

Multivariable Bidirectional Mendelian Randomization via Bayesian Directed Cyclic Graphical Models with Correlated Errors

Bitan Sarkar¹, Yuchao Jiang¹, Tian Ge², and Yang Ni³

¹Department of Statistics, Texas A&M University, College Station, TX, USA

²Psychiatric and Neurodevelopmental Genetics Unit, Center for Genomic Medicine, Massachusetts General Hospital, Boston, MA, USA

³Department of Statistics and Data Sciences, The University of Texas at Austin, Austin, TX, USA

Abstract

Mendelian randomization (MR) is a pivotal tool in genetics, genomics, and epidemiology, leveraging genetic variants as instrumental variables to infer causal relationships between exposures and outcomes. Traditional MR methods, while powerful, often rely on stringent assumptions such as the absence of feedback loops, which are frequently violated in complex biological networks. In addition, many popular MR approaches focus on only two variables (i.e., one exposure and one outcome), whereas our motivating applications of gene regulatory networks have many variables. In this article, we introduce a novel Bayesian framework for *multivariable* MR that concurrently addresses *unmeasured confounding* and *feedback loops*. Central to our approach is a sparse conditional cyclic graphical model with a sparse error variance-covariance matrix. Two structural priors are employed to enable the modeling and inference of causal relationships as well as latent confounding structures. Our method is designed to operate effectively with summary-level data, facilitating its application in contexts where individual-level data are inaccessible, e.g., due to privacy concerns. It can also account for horizontal pleiotropy, under which we establish the sufficient identifiability conditions. Through extensive simulations and applications to the GTEx and OneK1K data, we demonstrate the superior performance of our approach in recovering biologically plausible causal relationships in the presence of possible feedback loops and unmeasured confounding. Using posterior samples, we further quantify uncertainty in inferred network motifs by computing their posterior probabilities. The R package `MR.RGM` that implements the proposed method is available on CRAN (<https://cran.r-project.org/package=MR.RGM>).

Keywords: Causal Inference, Identifiability, Feedback Loops, Instrumental Variables, Unmeasured Confounding, Summary-Level Data, Gene Regulatory Networks, Horizontal Pleiotropy, Uncertainty Quantification.

1 Introduction

Mendelian randomization (MR) is a causal inference framework using genetic variants as instrumental variables and has revolutionized the fields of genetics and epidemiology. The main principle of MR is rooted in Mendel’s laws of inheritance, which ensure the random allocation of alleles, thereby mitigating confounding and reverse causation that often plague observational studies [14]. This natural randomization resembles the design of randomized controlled trials, offering a powerful alternative when such trials are infeasible.

Classical MR focuses on a single exposure and a single outcome, graphically represented in Figure 1a. To date, a wide range of MR methods have been developed including classic methods such as inverse-variance weighting (IVW [8]) for summary-level data and two-stage least squares [4, 49] for individual-level data, as well as more modern approaches such as MR-Egger regression [5], the weighted median estimator [6], MR-PRESSO [55], the weighted mode-based estimator [17], and the generalized summary-data-based Mendelian randomization [60].

There is also a range of software packages for MR. The `MendelianRandomization` package [9] provides R implementations of the IVW, MR-Egger, simple and weighted median, and intercept-based estimators. The `TwoSampleMR` package [20, 21] enables systematic two-sample MR analyses using summary-level data, offering a suite of MR methods along with data harmonization tools. The `OneSampleMR` package [38] is designed for analyses using individual-level data, supporting two-stage predictor substitution and two-stage residual inclusion approaches, which are appropriate when genetic instruments and exposures are measured within the same dataset.

Despite the large literature and software packages for MR methods, the focus has been predominantly on the “one exposure and one outcome” setting, where only the total causal effect can be inferred. Falling short in addressing the complexities of multiple exposures and outcomes, these MR methods cannot differentiate between direct and indirect/mediation effects. Bidirectional MR, for example, uses two separate analyses to test each direction (Figure 1b). Recognizing the complex nature of biological networks, multivariable MR (MVMR) was developed to estimate the direct effects of multiple exposures on an outcome simultaneously

(Figure 1c) [43]. MVMR accounts for the correlation between exposures, providing a more nuanced understanding of causal pathways. The `mrbayes` package [52] provides Bayesian implementations of IVW and MR-Egger for two-sample MR, including multivariable extensions. GRIVET is a recent approach that infers causal relationships among a set of variables in the presence of unmeasured confounding by leveraging directed acyclic graph (DAG) models [12]. MrDAG [61] is a Bayesian DAG model utilizing genetic variants as instruments.

While these MVMR approaches have enabled richer causal inference by discerning direct and indirect causal effects, their acyclic assumption excludes the possibility of directed cycles or feedback loops, which are prevalent in many biological systems such as gene regulatory networks, metabolic networks, and phenotypic disease networks. To capture potential feedback loops, Spirtes (1995) [47] extends DAG models to directed cyclic graph (DCG) models, which have been applied to genomics [10, 33, 34], brain imaging [41], and electronic health records [24]. However, they all assume there is no unmeasured confounding and hence would draw biased inference when the assumption is violated.

In this paper, we propose a new Bayesian MVMR approach based on non-recursive structural equation models (SEMs) with sparse correlated errors, termed Mendelian randomization with reciprocal graphical model (**MR.RGM**), which simultaneously addresses unmeasured confounding and feedback loops using genetic variants as instrumental variables, while modeling all traits jointly without pre-specifying exposure-outcome roles (Figure 1d). Besides addressing the challenges of unmeasured confounding and feedback loops, our approach has four additional features. First, like many MR methods, it does not require individual-level data; only summary-level data would suffice. Often, genetic variants are not publicly available, and only summary statistics are published. Our approach is versatile for these common settings. Second, our approach also infers the exact positions of confounding via a graphical spike-and-slab prior, enabling the identification of which sets of variables may be confounded. Third, the Bayesian nature of our approach allows for natural uncertainty quantification and enhanced interpretability by providing credible intervals for causal effects and posterior edge inclusion probabilities; in addition, we provide a `NetworkMotif` function that computes posterior probabilities for user-specified network motifs (e.g., a feedforward

loop) based on posterior samples. Finally, we also extend `MR.RGM` to account for horizontal pleiotropy and weak instruments; this extension, which we refer to as `MR.RGM+`, enables more flexible modeling and requires formal identifiability conditions, which we establish as a theoretical contribution. A conceptual comparison of the aforementioned MR frameworks and ours is summarized in Figure 1.

To assess the performance of our approach, we conduct extensive simulation studies with realistic network structures such as scale-free networks and small-world networks, comparing its performance against existing MR methods that are implemented in the popular MR software packages, `MendelianRandomization`, `mr bayes`, and `OneSampleMR`. Furthermore, we apply the proposed method to two real-world datasets, the GTEx V7 skeletal muscle data [13] and the OneK1K data [58], where we not only recover biologically plausible causal relationships but also report high posterior probabilities for key network motifs supported by existing biological literature.

2 Method

2.1 Overview of MR, Bidirectional MR, and MVMR

MR. MR is an instrumental variable approach to infer causal relationships between exposures and outcomes using genetic variants as instruments. The validity of MR rests on three key assumptions: (i) the genetic variants must be associated with the exposure of interest (relevance); (ii) they must be independent of any confounders of the exposures and outcomes (independence); and (iii) they should influence the outcome only through their effect on the exposure, without any alternative pathways (exclusion restriction). Traditionally, MR only considers one exposure Y_1 and one outcome Y_2 with the direction of causality fixed to be $Y_1 \rightarrow Y_2$. Using X_1 as an instrument for the exposure Y_1 , MR considers the following generative model,

$$Y_1 = b_1 X_1 + c_1 W + E_1 \tag{1}$$

$$Y_2 = a_{21} Y_1 + c_2 W + E_2, \tag{2}$$

where W is an unmeasured confounder of Y_1 and Y_2 , and E_1, E_2 are independent exogenous errors. The confounder induces non-causal association between Y_1 and Y_2 , which in turn leads to a biased estimate of a_{21} , the main quantity of interest, if we simply regress Y_2 on Y_1 . Equations (1)-(2) as a generative model imply the exclusion restriction as well as the relevance assumption (as long as $b_1 \neq 0$). We additionally assume $X_1 \perp W$ (i.e., the independence assumption).

Two-stage least squares (2SLS) and inverse-variance weighting (IVW) are the two most commonly used methods to estimate the causal effect a_{21} of exposure Y_1 on outcome Y_2 . In 2SLS, we first regress Y_1 on X_1 and get a fitted \hat{Y}_1 and then regress Y_2 on \hat{Y}_1 . The coefficient of \hat{Y}_1 in the latter regression is the desired causal effect a_{21} . Such an approach can be justified by plugging (1) into (2),

$$Y_2 = a_{21}b_1X_1 + a_{21}c_1W + a_{21}E_1 + c_2W + E_2 \quad (3)$$

$$= a_{21}\hat{Y}_1 + a_{21}c_1W + a_{21}E_1 + c_2W + E_2, \quad (4)$$

where the second equality uses the fact that $\hat{Y}_1 = b_1X_1$ at the population level because X_1 is independent of W and E_1 . This independence (plus the independence of X_1 and E_2) and (4) together imply that a_{21} can be recovered by regressing Y_2 on \hat{Y}_1 .

IVW relies on the fact that

$$a_{21} = \frac{a_{21}b_1}{b_1} := \frac{r_{21}}{r_{11}} \quad (5)$$

where the numerator r_{21} is the effect of X_1 on Y_2 in a simple linear regression model due to (3) and the mutual independence of X_1, W, E_1, E_2 , and the denominator r_{11} is the effect of X_1 on Y_1 in a simple linear regression model due to (1) and the same mutual independence assertion. IVW then takes a weighted average of those ratio estimators when there are multiple instruments with weights equal to the inverse variances of the estimators.

Bidirectional MR. When the direction of causality between Y_1 and Y_2 is unknown, separately applying MR in both directions is often adopted, provided that an instrument X_2 is also available for Y_2 , which is known as the bidirectional MR. When the causal effects

in both directions are significant, both may be reported simultaneously, indicating bidirectional/reciprocal causal effects. The validity of using 2SLS and IVW in such a scenario can be justified by considering a non-recursive SEM as a generative model,

$$\begin{cases} Y_1 = a_{12}Y_2 + b_1X_1 + c_1W + E_1 \\ Y_2 = a_{21}Y_1 + b_2X_2 + c_2W + E_2. \end{cases} \quad (6)$$

Crucially, unlike Equations (1) and (2), the two equations in (6) are coupled. The right-hand sides of these equations are *not* the conditional expectations of the left-hand sides unless a_{12} or a_{21} is zero. Under generative model (6), the marginal distributions of Y_1 and Y_2 are:

$$\begin{aligned} Y_1 &= \frac{1}{1 - a_{12}a_{21}} \{b_1X_1 + a_{12}b_2X_2 + (c_1 + a_{12}c_2)W + E_1 + a_{12}E_2\}, \\ Y_2 &= \frac{1}{1 - a_{12}a_{21}} \{b_2X_2 + b_1a_{21}X_1 + (c_2 + a_{21}c_1)W + E_2 + a_{21}E_1\}. \end{aligned} \quad (7)$$

Because X_1, X_2, W, E_1, E_2 are mutually independent, we have

$$\begin{cases} \frac{b_1}{1 - a_{12}a_{21}} = r_{11} \\ \frac{b_1a_{21}}{1 - a_{12}a_{21}} = r_{21} \\ \frac{a_{12}b_2}{1 - a_{12}a_{21}} = r_{12} \\ \frac{b_2}{1 - a_{12}a_{21}} = r_{22} \end{cases}$$

where r_{jk} is the effect of X_k on Y_j in a simple linear regression for $j, k \in \{1, 2\}$. Hence, the causal effect of Y_1 on Y_2 is

$$a_{21} = \frac{r_{21}}{r_{11}},$$

which coincides with (5) because the extra factor $\frac{1}{1 - a_{12}a_{21}}$ due to the coupling in SEM is common to both r_{21} and r_{11} and thus cancels out in the ratio. Similarly, $a_{12} = \frac{r_{12}}{r_{22}}$. Consequently, both 2SLS and IVW are still valid estimation procedures for bidirectional MR even though regression and SEM are generally very different statistical models.

MVMR. However, most real-world systems have more than two variables. Consider, for example, a trivariate generative SEM,

$$\begin{cases} Y_1 = a_{12}Y_2 + a_{13}Y_3 + b_1X_1 + c_1W + E_1 \\ Y_2 = a_{21}Y_1 + a_{23}Y_3 + b_2X_2 + c_2W + E_2 \\ Y_3 = a_{31}Y_1 + a_{32}Y_2 + b_3X_3 + c_3W + E_3. \end{cases} \quad (8)$$

where a_{jk} is the direct causal effect of Y_k on Y_j , often represented graphically by $Y_k \rightarrow Y_j$ or simply $k \rightarrow j$ in a causal graph. Unlike the bivariate case, applying MR or bidirectional MR to (Y_1, Y_2) does not estimate the direct causal effect a_{12} . Instead, it targets the total causal effect t_{12} of Y_2 on Y_1 , which consists of both direct and indirect/mediated effects via Y_3 and can be found by do-calculus [39]:

$$t_{12} = \frac{a_{12} + a_{13}a_{32}}{|1 - a_{13}a_{31}|}, \quad (9)$$

where $a_{13}a_{32}$ is the indirect causal effect and $|1 - a_{13}a_{31}|$ is the ‘‘amplification’’ of the causal effect due to the reciprocal causal relationship between Y_1 and Y_3 . Because t_{12} is generally not equal to a_{12} , naively applying MR to construct causal graphs could lead to many false discoveries. For example, consider a hypothetical genetic regulatory cascade $Y_1 \rightarrow Y_2 \rightarrow Y_3$. Pairwise applications of MR would impute a false edge $Y_1 \rightarrow Y_3$ since the total effect of Y_1 on Y_3 is non-zero. For MVMR, a principled approach is the use of graphical models, which aim to estimate the direct causal effects directly. However, as reviewed in Section 1, there is a lack of MVMR methods that can accommodate and estimate reciprocal causality under unmeasured confounding.

2.2 Proposed MR.RGM

Let $\mathbf{Y} = (Y_1, \dots, Y_p)^T$ denote p traits, and let $\mathbf{X} = (X_1, \dots, X_k)^T$ represent k instrumental variables. In our later applications, the traits are gene expressions, and the instruments are (cis-) single-nucleotide polymorphisms (SNPs) that are significantly correlated with the traits. Let $\mathbf{U} = (U_1, \dots, U_l)^T$ denote a set of l covariates, and $\mathbf{W} = (W_1, \dots, W_t)^T$ represents t latent confounders, which are assumed to be $\mathbf{W} \sim N_t(0, \mathbf{I}_t)$, i.e., t independent sources of

unmeasured confounding. We model the data-generative process by an SEM:

$$\mathbf{Y} = \mathbf{A}\mathbf{Y} + \mathbf{B}\mathbf{X} + \mathbf{C}\mathbf{U} + \mathbf{D}\mathbf{W} + \mathbf{E}, \quad (10)$$

where $\mathbf{A} = (a_{jh}) \in \mathbb{R}^{p \times p}$ with a_{jh} being the direct causal effect of trait h on trait j , $\mathbf{B} = (b_{jh}) \in \mathbb{R}^{p \times k}$ with b_{jh} capturing the effect of instrumental variable h on trait j , $\mathbf{C} = (c_{jh}) \in \mathbb{R}^{p \times l}$ with c_{jh} representing the effect of covariate h on trait j , $\mathbf{D} = (d_{jh}) \in \mathbb{R}^{p \times t}$ with d_{jh} being the impact of unobserved confounder h on trait j , and $\mathbf{E} \sim N_p(0, \mathbf{\Sigma})$ with diagonal $\mathbf{\Sigma}$ is the independent exogenous errors. We further assume that there are no self-loops, i.e., $\text{diag}(\mathbf{A}) = \mathbf{0}$ and that \mathbf{X} , \mathbf{U} , \mathbf{W} , and \mathbf{E} are all mutually independent. Structural zeros are imposed on \mathbf{B} such that $b_{jh} \neq 0$ if and only if X_h is the instrument for Y_j ; this will be later relaxed to account for horizontal pleiotropy and weak instruments.

The presence of the latent confounders \mathbf{W} induces correlation among traits. Define:

$$\mathbf{E}^* := \mathbf{D}\mathbf{W} + \mathbf{E} \sim N_p(0, \mathbf{D}\mathbf{D}^T + \mathbf{\Sigma}) = N_p(0, \mathbf{\Sigma}^*),$$

where the latent confounders \mathbf{W} have been integrated out. The covariance matrix $\mathbf{\Sigma}^*$ of this new error term is not diagonal and hence correlated. A non-zero entry $\Sigma_{jh}^* \neq 0$ for $j \neq h$ indicates the presence of a latent confounder affecting both Y_j and Y_h as it must exist some s such that neither d_{js} nor d_{hs} is zero. This allows us to infer potential latent confounding structures directly from the covariance matrix of the errors, without having to assume a known number of confounders.

Rewriting (10) with \mathbf{E}^* , we have,

$$\begin{aligned} (\mathbf{I}_p - \mathbf{A})\mathbf{Y} &= \mathbf{B}\mathbf{X} + \mathbf{C}\mathbf{U} + \mathbf{E}^* \\ \implies \mathbf{Y} &= (\mathbf{I}_p - \mathbf{A})^{-1}\mathbf{B}\mathbf{X} + (\mathbf{I}_p - \mathbf{A})^{-1}\mathbf{C}\mathbf{U} + (\mathbf{I}_p - \mathbf{A})^{-1}\mathbf{E}^*. \end{aligned} \quad (11)$$

This formulation accommodates feedback loops through \mathbf{A} (e.g., if $a_{jh} \neq 0$ and $a_{hj} \neq 0$, then $Y_j \rightleftharpoons Y_h$) and models latent confounding via the error covariance structure $\mathbf{\Sigma}^*$. The conditional distribution of \mathbf{Y} given \mathbf{X} and \mathbf{U} can be derived from (11):

$$\mathbf{Y} \mid \mathbf{X}, \mathbf{U} \sim N_p \left\{ (\mathbf{I}_p - \mathbf{A})^{-1}\mathbf{B}\mathbf{X} + (\mathbf{I}_p - \mathbf{A})^{-1}\mathbf{C}\mathbf{U}, (\mathbf{I}_p - \mathbf{A})^{-1}\mathbf{\Sigma}^*(\mathbf{I}_p - \mathbf{A})^{-T} \right\}. \quad (12)$$

To enable the use of summary-level data—common in MR where individual-level data may be unavailable due to privacy concerns—we represent the conditional distribution in (12) in terms of sufficient statistics, which are empirical second-moment matrices:

$$\begin{aligned} \mathbf{S}_{\mathbf{y}\mathbf{y}} &= \frac{1}{n} \sum_{i=1}^n \mathbf{y}_i \mathbf{y}_i^T, & \mathbf{S}_{\mathbf{y}\mathbf{x}} &= \frac{1}{n} \sum_{i=1}^n \mathbf{y}_i \mathbf{x}_i^T, & \mathbf{S}_{\mathbf{y}\mathbf{u}} &= \frac{1}{n} \sum_{i=1}^n \mathbf{y}_i \mathbf{u}_i^T, \\ \mathbf{S}_{\mathbf{x}\mathbf{x}} &= \frac{1}{n} \sum_{i=1}^n \mathbf{x}_i \mathbf{x}_i^T, & \mathbf{S}_{\mathbf{u}\mathbf{u}} &= \frac{1}{n} \sum_{i=1}^n \mathbf{u}_i \mathbf{u}_i^T, & \mathbf{S}_{\mathbf{x}\mathbf{u}} &= \frac{1}{n} \sum_{i=1}^n \mathbf{x}_i \mathbf{u}_i^T. \end{aligned}$$

These sufficient statistics allow us to make causal inference without requiring access to individual-level data. The distribution (12), based on the sufficient statistics, is given by (see Supplementary Section-S1 for the derivation):

$$\begin{aligned} & p(\{\mathbf{y}_i\}_{i=1}^n | \{\mathbf{x}_i\}_{i=1}^n, \{\mathbf{u}_i\}_{i=1}^n, \mathbf{A}, \mathbf{B}, \mathbf{C}, \Sigma^*) \\ &= (2\pi)^{-\frac{np}{2}} \cdot \det(\Sigma^*)^{-\frac{n}{2}} \cdot |\det(\mathbf{I}_p - \mathbf{A})|^n \cdot \exp\left(-\frac{1}{2}n \cdot [\text{tr}(\mathbf{S}_{\mathbf{y}\mathbf{y}}(\mathbf{I}_p - \mathbf{A})^T \Sigma^{*-1}(\mathbf{I}_p - \mathbf{A})) \right. \\ &\quad - 2n \cdot \text{tr}(\mathbf{S}_{\mathbf{y}\mathbf{x}} \mathbf{B}^T \Sigma^{*-1}(\mathbf{I}_p - \mathbf{A})) + \mathbf{n} \cdot \text{tr}(\mathbf{S}_{\mathbf{x}\mathbf{x}} \mathbf{B}^T \Sigma^{*-1} \mathbf{B}) \\ &\quad - 2n \cdot \text{tr}(\mathbf{S}_{\mathbf{y}\mathbf{u}} \mathbf{C}^T \Sigma^{*-1}(\mathbf{I}_p - \mathbf{A})) + 2\mathbf{n} \cdot \text{tr}(\mathbf{S}_{\mathbf{x}\mathbf{u}} \mathbf{C}^T \Sigma^{*-1} \mathbf{B}) \\ &\quad \left. + n \cdot \text{tr}(\mathbf{S}_{\mathbf{u}\mathbf{u}} \mathbf{C}^T \Sigma^{*-1} \mathbf{C})\right]). \end{aligned}$$

Our goal is to estimate the matrices \mathbf{A} , \mathbf{B} , \mathbf{C} , and Σ^* , which respectively capture the causal relationships among traits, instrumental effects, covariate effects, and the confounding effects. To achieve this, we adopt a fully Bayesian framework by placing prior distributions on these parameters and using Markov chain Monte Carlo (MCMC) to sample them from their joint posterior distribution. Using sufficient statistics also improves the scalability with respect to the sample size n . The cost of evaluating the likelihood based on raw data is $\mathcal{O}(n\{p^2 + p(k+l)\} + p^3)$ whereas that of sufficient statistics is $\mathcal{O}(p^3 + p^2(k+l) + p(k+l)^2)$, which is a big reduction if $n \gg \{p, k, l\}$.

2.3 Priors and Posteriors

The priors are chosen to support both parameter estimation and structural learning, with a particular emphasis on inducing sparsity in the causal graph (\mathbf{A}) and in the confounding structure (Σ^*) via two sets of spike-and-slab priors. A full specification of all prior

distributions and hyperparameters is provided in Supplementary Section-S2. As an extension to account for horizontal pleiotropy and weak instruments, we impose another set of spike-and-slab priors to select valid instruments, for which the details are also provided in Supplementary Section-S2.

We use MCMC to draw posterior samples of the model parameters. Step-by-step updating scheme is detailed in the Supplementary Section-S3. Our implementation leverages `Rcpp` and linear algebra for efficient matrix computations. Figure 2 provides a schematic overview of the full `MR.RGM` workflow.

2.4 Identifiability of `MR.RGM+` Under Instrument Diversity and Sparsity

When there is horizontal pleiotropy (i.e., the violation of the exclusion restriction condition), the proposed model is not identifiable without additional assumptions. Without loss of generality, we drop the observed covariates \mathbf{U} from the proposed SEM:

$$\mathbf{Y} = \mathbf{A}\mathbf{Y} + \mathbf{B}\mathbf{X} + \mathbf{E}^*, \quad \mathbf{E}^* \sim N_p(\mathbf{0}, \boldsymbol{\Sigma}^*), \quad (13)$$

where $\text{diag}(\mathbf{A}) = \mathbf{0}$ and $\mathbf{I}_p - \mathbf{A}$ is assumed to be invertible. Define the reduced-form coefficient

$$\boldsymbol{\Pi} := (\mathbf{I}_p - \mathbf{A})^{-1}\mathbf{B}. \quad (14)$$

By theory of multivariate linear regression, $\boldsymbol{\Pi}$ is identifiable from second moments, $\boldsymbol{\Pi} = \text{Cov}(\mathbf{Y}, \mathbf{X})\text{Var}(\mathbf{X})^{-1}$ provided that $\text{Var}(\mathbf{X})$ is invertible. To establish identifiability of (\mathbf{A}, \mathbf{B}) from $\boldsymbol{\Pi}$, we make the following three assumptions:

Assumption 1 (Instrument Diversity). *All $(p - 1) \times (p - 1)$ minors of $\boldsymbol{\Pi}$ are non-zero. That is, for every subset $R \subseteq \{1, \dots, p\}$ with $|R| = p - 1$ and every subset $H \subseteq \{1, \dots, k\}$ with $|H| = p - 1$:*

$$\det(\boldsymbol{\Pi}_{R,H}) \neq 0.$$

We provide a few examples in Supplementary Section-S4. Intuitively, this assumption requires that for each trait j , the instruments must provide “diverse” information about the

other traits; in other words, no $(p - 1)$ instruments can have collinear effects on the non- j traits. Note that the Instrument Diversity assumption is a condition on $\mathbf{\Pi} = (\mathbf{I} - \mathbf{A})^{-1}\mathbf{B}$, whereas the Relevance assumption of a classic MR is a condition on \mathbf{B} . Even if row j of \mathbf{B} is zero (no instruments directly affect trait j), row j of $\mathbf{\Pi}$ can be non-zero through mediation:

$$\mathbf{\Pi}_{j,:} = \sum_h [(\mathbf{I} - \mathbf{A})^{-1}]_{jh} \mathbf{B}_{:,h},$$

where $\mathbf{B}_{:,h}$ denotes the h th column of \mathbf{B} . Hence, a trait with no direct instruments can still have non-zero reduced-form effects. Let $\|\cdot\|_0$ denote the L_0 norm, i.e., the number of non-zero elements in a vector, and let $\mathbf{B}_{j,:}$ denote the j th row of \mathbf{B} .

Assumption 2 (Sparsity). *Every trait has at most $\frac{k-p+1}{2}$ instruments, i.e., $\max_{j \in \{1, \dots, p\}} \|\mathbf{B}_{j,:}\|_0 \leq \frac{k-p+1}{2}$.*

Intuitively, this assumption requires the violation of the Exclusion Restriction assumption to be sparse. In other words, a dense \mathbf{B} implies a lot of violations, which is ruled out by the Sparsity assumption. For example, for $p = 10$ traits and $k = 30$ instruments, we assume $\|\mathbf{B}_{j,:}\|_0 \leq \frac{30-10+1}{2} = 10.5$, i.e., each trait can have at most 10 instruments with direct effects.

Assumption 3 (Independence). *The instruments are not confounded.*

This assumption is also required in the classic MR.

Theorem 1 (Identifiability of MR.RGM+). *Under Assumptions 1-3, $(\mathbf{A}, \mathbf{B}, \mathbf{\Sigma}^*)$ is identifiable.*

The proof is provided in Supplementary Section-S4; here we provide a sketch. The reduced-form matrix $\mathbf{\Pi} = (\mathbf{I}_p - \mathbf{A})^{-1}\mathbf{B}$ is identified from data, but without constraints, infinitely many (\mathbf{A}, \mathbf{B}) pairs yield the same $\mathbf{\Pi}$. The key insight is that the sparsity constraint on \mathbf{B} provides enough equations to identify \mathbf{A} . Inverting the relationship gives $\mathbf{B} = (\mathbf{I}_p - \mathbf{A})\mathbf{\Pi}$, so each entry satisfies:

$$b_{jh} = \pi_{jh} - \sum_{i \neq j} a_{ji} \pi_{ih}.$$

When $b_{jh} = 0$ (instrument h has no direct effect on trait j), this becomes a linear constraint on the causal effects $\{a_{ji}\}_{i \neq j}$:

$$\pi_{jh} = \sum_{i \neq j} a_{ji} \pi_{ih}.$$

Crucially, the constraints for trait j involve only the $p - 1$ unknowns in row j of \mathbf{A} , so the problem decomposes into p independent linear systems. For trait j with $s_j := \|\mathbf{B}_{j,:}\|_0$ direct instrument effects, there are $k - s_j$ zero constraints in $p - 1$ unknowns. With $s_j \leq (k - p + 1)/2$, any two candidate solutions must share at least $k - 2s_j \geq p - 1$ zero constraints. This overdetermined system can have at most one solution. The Instrument Diversity condition ensures these shared constraints have full rank, guaranteeing that the unique solution exists.

3 Simulation Studies

We evaluate the performance of the proposed MR.RGM, using simulations designed to reflect complex causal structures commonly found in biological systems. We compare MR.RGM with several baseline methods such as MR packages `OneSampleMR`, `mrbayes`, and `MendelianRandomization`, which include MR approaches based on Simple Median, Weighted Median, and IVW. These baselines offer a diverse representation of current MR tools; however, none explicitly model feedback loops. For clarity, we denote the Simple Median, Weighted Median, and IVW methods from the `MendelianRandomization` package as `MR-SimpleMedian`, `MR-WeightedMedian`, and `MR-IVW`, respectively. For ablation, we also consider two variants of MR.RGM, namely, `MR.RGM_NoConf`, which assumes no latent confounding and was implemented by [44], and `MR.RGM+`, which accounts for horizontal pleiotropy. For the implementation of `MR.RGM+`, rather than prespecifying instrument-trait mapping, we treat every SNP as a potential instrument for every gene/trait.

We consider three distinct scenarios with topological features commonly observed in gene regulatory networks – scale-free and small-world graphs are well-established motifs in systems biology, and horizontal pleiotropy is ubiquitous challenges in MR.

1. **Scale-free graph with feedback loops and unmeasured confounding:** A scale-free causal network with directed cycles is constructed to model reciprocal regulation. Each trait is assigned three unique instruments, and no pleiotropy is introduced.
2. **Small-world graph with feedback loops and unmeasured confounding:** Similar to Case 1, but using a small-world network topology. Each trait again receives

three unique instruments, and no pleiotropy is introduced.

3. **Small-world graph with feedback loops, unmeasured confounding, and horizontal pleiotropy:** In addition to the structure in Case 2, horizontal pleiotropy is introduced by assigning one shared IV to each consecutive trait pair (traits are arbitrarily ordered).

Given the graph and IV structure, we simulate data from (10) without covariates, where the non-zero off-diagonal entries of \mathbf{A} are sampled from $\text{Uniform}[-0.1, 0.1]$, reflecting small effect sizes to capture low-signal conditions common in real data. To ensure that both the instrument effects and the confounding effects remain detectable relative to these weak causal signals, the non-zero entries of \mathbf{B} are set to be 1, the entries of \mathbf{D} are sampled from $\{-1, +1\}$, giving them a larger scale than the entries of \mathbf{A} . The instruments and the unmeasured confounders are drawn from independent standard normal distributions. The errors are drawn from independent centered normal distributions with variance 9, resulting in a weak signal-to-noise setting.

For Case 3, since the competing methods do not account for horizontal pleiotropy, we randomly assign each instrument to one of the two traits if an instrument affects two traits.

We vary sample size $n \in \{500, 1000, 10000, 30000\}$ and number of traits $p \in \{5, 10\}$, yielding 8 settings per scenario. Each simulation is repeated 20 times. Performance is evaluated based on the following criteria:

- **Graph Recovery:** To evaluate each method’s ability to recover the true causal graph, we compute area under the ROC curve (AUC), true positive rate (TPR), false discovery rate (FDR), and Matthews correlation coefficient (MCC).
- **Causal Effect Estimation:** We compute maximum absolute deviation (MaxAbsDev), mean absolute deviation (MAD), and mean squared deviation (MSD) between the estimated and true causal effects among all pairs of traits.
- **Confounding Structure Recovery:** We normalize the true variance-covariance matrix $\Sigma^* = \mathbf{D}\mathbf{D}^T + \Sigma$ to the range of $[0, 1]$ and threshold it at its empirical mean to

create a “true” significant confounding structure. We then compute AUC, TPR, FDR, and MCC of our estimated confounding structure.

- **Instrument-Trait Selection Accuracy.** When MR.RGM+ is applied (i.e., in Case 3), we also report the AUC of the instrument-trait selection.

In the main text, we focus on visualizing the AUC for graph recovery, confounding structure recovery, and instrument–trait selection, and the MAD for causal effect estimation, for network size $p=10$. In addition, for the scale-free network with feedback loops and unmeasured confounding and network size $p=10$, we report the full performance tables for graph recovery (AUC, TPR, FDR, and MCC; Table 1) and for causal effect estimation (MaxAbsDev, MeanAbsDev, and MeanSqDev; Table 2). The corresponding plots for network size $p=5$, as well as the remaining performance tables for both $p=5$ and $p=10$ across all scenarios, are provided in Supplementary Section-S5.

Results for Cases 1-2. The results for Cases 1 and 2 are similar and hence are reported together. Figures 3a and 4a show that MR.RGM consistently achieves the highest AUC in graph recovery across all sample sizes in both cases. MR.RGM_NoConf underperforms MR.RGM for large n , reflecting the influence of unmeasured confounding. MR-SimpleMedian, MR-WeightedMedian, MR-IVW, OneSampleMR and mrbayes, improve steadily with increasing n and nearly catch up MR.RGM by $n=10,000-30,000$.

Figures 3b and 4b show that MR.RGM attains the lowest MAD for the causal effect estimation for all sample sizes. MR.RGM_NoConf is competitive at $n \in \{500, 1000\}$ but become less so as n grows. MR-SimpleMedian, MR-WeightedMedian, MR-IVW, OneSampleMR, and mrbayes improve with sample size and eventually surpass MR.RGM_NoConf at larger n , while remaining short of MR.RGM.

Tables 1 and 2 summarize the numerical results for Case 1 with $p=10$, and they closely mirror the patterns seen in the AUC and MAD boxplots. Table 1 shows that MR.RGM achieves comparable or higher TPR together with consistently lower FDR and higher MCC than competing methods as the sample size increases. Table 2 likewise shows that MR.RGM attains smaller MaxAbsDev and MeanSqDev than all alternatives. By contrast, MR.RGM_NoConf lags

behind in both graph recovery and causal effect estimation, especially at larger n , reflecting its inability to account for unmeasured confounding.

Figures 5a and 5b show that `MR.RGM` recovers the confounding structure increasingly well with sample size: the median AUC approaches 1.0 for $n \geq 10,000$. Competing methods do not infer the confounding structure.

Results for Case 3. Figure 6a shows that `MR.RGM+` attains the highest AUC for graph recovery across all sample sizes under horizontal pleiotropy. `MR.RGM` remains competitive but is modestly attenuated by horizontal pleiotropy, while `MR.RGM.NoConf` lags further because it omits latent confounding. `MR.SimpleMedian`, `MR.WeightedMedian`, `MR-IVW`, `OneSampleMR`, and `mrBayes` improve with n but stay below `MR.RGM+`.

Figure 6b shows that `MR.RGM+` achieves the lowest MAD across all n and is the clear winner. By contrast, `MR.RGM` and `MR.RGM.NoConf` exhibit higher MAD. `MR.SimpleMedian`, `MR.WeightedMedian`, `MR-IVW`, `OneSampleMR`, and `mrBayes` improve with sample size and surpass `MR.RGM` and `MR.RGM.NoConf` at large n , yet they remain well above `MR.RGM+`.

Figure 7 shows confounding structure recovery improving with sample size. Under horizontal pleiotropy, `MR.RGM+` reaches nearly perfect AUC by $n \geq 10,000$, whereas `MR.RGM` improves with n but does not quite attain perfect AUC.

Moreover, `MR.RGM+` attains consistently high AUC for recovering the true instrument-trait map (Figure 8) with AUC values tightly concentrated above 0.95 across all n , indicating strong selection performance even at moderate sample size.

Scalability Test. We benchmark the runtime of `MR.RGM` against the competing methods. We fix the number of observations at the largest value used in our simulations, $n = 30,000$, and vary the number of traits $p \in \{2, 5, 10, 20\}$. All Bayesian methods (`MR.RGM`, `MR.RGM.NoConf`, `MR.RGM+`, `mrBayes`) use 50,000 MCMC iterations with 10,000 burn-in; for `MendelianRandomization` we also run 50,000 iterations. Benchmarks were executed in RStudio on an Apple M2 Pro machine (10-core CPU, 3.5 GHz) with 16 GB unified memory. Each method is run 20 times, and we report the median wall-clock runtime in seconds in Figure 9. As p increases, the runtime rises for all methods, but the `MR.RGM` family remains practi-

cal. For example, at $p = 20$, the median runtime is approximately 90s for `MR.RGM`, 55s for `MR.RGM_NoConf`, 233s for `MR.RGM+`.

4 Real Data Analysis

In this section, we demonstrate the effectiveness of the proposed method by applying it to two real-world genomic datasets: the skeletal muscle samples from the GTEx v7 dataset and the B-cell samples from the OneK1K dataset. For each dataset, we discard individuals who do not have complete information of gene expressions, SNPs, or relevant covariates (e.g., sex and age).

We apply our algorithm to infer the causal gene regulatory networks, with the associated uncertainty quantified by the posterior probabilities of edge inclusion, and assess the presence and the structure of latent confounders. Because horizontal pleiotropy may link any SNP to multiple genes in real tissues, we use the `MR.RGM+` variant, allowing the model to select the relevant SNP–gene pairs. We run the proposed MCMC with 50,000 iterations, a burn-in of 10,000, and thinning every 10 iterations, yielding 4,000 posterior samples.

Beyond edge-level posterior inclusion probabilities, we further summarize higher-order regulatory structure using the `NetworkMotif` function of our R package. This function computes posterior probabilities for user-specified network motifs—such as feedback loops, feedforward loops, and cascades—by quantifying the proportion of posterior samples in which all constituent edges are simultaneously present. This network motif-level summary provides a principled way to quantify the uncertainty of biologically meaningful regulatory patterns that extend beyond pairwise interactions.

4.1 Application to GTEx v7 Skeletal Muscle Tissue Data

Dataset description. The GTEx project is a comprehensive resource designed to study the relationship between genetic variation and gene expression across multiple human tissues. We focus on the skeletal muscle samples from GTEx v7, which consists of 332 individuals with both genotype and gene expression data available. Our analysis centers around the

mechanistic target of rapamycin (mTOR) signaling pathway, a key regulator of cell growth and metabolism, which has been widely studied in both physiological and pathological contexts. We select 18 genes that are well-established components or regulators of the mTOR signaling cascade:

MTOR, ERK, AMPK, PI3K, PDK1, SHIP1, VHL, GSK3B, Tel2, TSC2, MLST8, Folliculin/BHD, PKCA, PHLPP1/2, INSULIN RECEPTOR, PRAS40, FKBP12, S6K.

We extract normalized expression levels of these 18 genes for the 332 individuals, resulting in a 332×18 gene expression matrix. We utilize the `signif_variant_gene_pairs` file provided by GTEx and identify 62 SNPs that show significant association with at least one of the 18 genes. The resulting genotype (instrument) matrix has dimensions 332×62 . In addition to gene expression and SNPs, we control for two individual-level covariates: sex and age. The sex variable is coded as binary (male/female), while age is discretized into ordinal bins: 20–29 \rightarrow 1, 30–39 \rightarrow 2, ..., 70–79 \rightarrow 6.

Results. Figure 10 shows the estimated causal network. For simplicity, we only display causal relationships for which the posterior inclusion probabilities (PIPs) are over 0.85 and confounding relationships for which the PIPs are over 0.5. Blue arrows denote directed causal edges (double-headed where bidirectional), and orange curved links indicate latent confounding of gene pairs. Within each edge type, lighter lines indicate lower PIP.

In Tables 3 and 4, we highlight a subset of biologically plausible causal relationships (gene regulations) and confounding structure, respectively. Generally, they align well with known molecular interactions within the mTOR signaling pathway and related regulatory cascades in muscle tissue. These results are obtained without imposing any prior knowledge about the underlying network topology, demonstrating the power of the proposed method in discovering interpretable gene regulatory relationships from genomic data.

In addition to individual regulatory edges, we examined higher-order regulatory motifs within the inferred mTOR signaling network. We identify a feedback loop involving *PDK1*, *VHL*, and *PKCA* (Figure 12a). *PDK1* acts as a central kinase upstream of multiple metabolic pathways, while *VHL* regulates hypoxia-inducible signaling that intersects with insulin and

mTOR pathways [16]. *PKCA* participates in insulin-responsive signaling and modulates downstream mTOR activity [32]. The simultaneous presence of these interactions suggests a regulatory feedback architecture integrating nutrient sensing, hypoxia response, and kinase signaling. The posterior probability of this motif is 0.854.

We further identify a feedforward loop in which *PDK1* regulates *S6K* both directly and indirectly through *VHL* (Figure 12b), consistent with coordinated control of protein synthesis downstream of insulin and growth factor signaling [2, 30]. This feedforward structure exhibits a posterior probability of 0.724.

Finally, a cascade motif *VHL*→*PKCA*→*MTOR* highlights a biologically plausible signaling flow linking oxygen sensing to mTORC1 activation (Figure 12c) [16, 45], with a high posterior probability of 0.931.

4.2 Application to OneK1K B Cell Data

Dataset description. The OneK1K cohort is a deeply phenotyped dataset combining genotype and transcriptomic data from a large number of individuals to study immune regulatory mechanisms. In this study, we focus on the B cells from 891 individuals. B cells are essential to adaptive immunity, and the B cell receptor (BCR) signaling pathway governs key processes such as antigen recognition, proliferation, and survival.

We analyze expression data for 66 genes central to the BCR signaling cascade, including membrane receptors, kinases, adaptor proteins, transcription factors, and regulators of apoptosis. The curated genes were selected based on their involvement in distinct signaling modules:

- **Membrane receptors and proximal signaling:** *CD19*, *BCR*, *FGR2B*, *SHIP*, *LYN*, *SYK*, *CD22*, *CD45*, *CBP/PAG*, *CSK*, *PIR-B*
- **Adaptor proteins and scaffolds:** *BCAP*, *BLNK*, *GRB2*, *LAB*, *BAM32*, *DOK1*, *CBL*
- **PI3K-AKT-mTOR axis:** *P85*, *PI3K*, *PIP3*, *AKT*, *P70S6K*, *GSK3*

- **PLC γ and calcium signaling:** *PLCY2, CAM, CAMK, PKC, NFAT*
- **RAS/MAPK signaling:** *SOS, RASGRP, RASGAP, RAS, RAP, RIAM, MEK, MEK1/2, ERK1/2, C-RAF, MEKK, JNK, P38*
- **Cytoskeletal rearrangement and trafficking:** *EZRIN, CLATHRIN, VAV, RAC, HS1, PYK2*
- **NF- κ B signaling module:** *CARMA1, TAK1, BCL10, MALT1, IKK, NFKB, IKB*
- **Transcriptional regulators and apoptosis mediators:** *CD40, ETS1, BFL1, BCL-XL, BCL6, EGR1, JUN, ATF2, CREB, MEF2C, RAPL*

For these genes, we extract normalized cell-type-level gene expressions across all 891 individuals, resulting in a 891×66 gene expression matrix. SNP-gene marginal association scores are obtained from the OneK1K study. We retain 847 SNPs significantly associated with at least one of the 66 genes, producing an instrument matrix of dimension 891×847 . We also include as covariates sex (male/female) and age (discretized: <30 as 1, 30–39 as 2, 40–49 as 3, ..., 70–79 as 6, and 80+ as 7).

Results. To visualize the estimated causal network without clutter, we focus on the following 29 genes, whose causal relationships will be discussed in detail:

PYK2, SYK, CBL, DOK1, PIP3, AKT, CD19, PI3K, ERK1/2, JUN, NFKB, IKB, PKC, CAMK, PLCY2, VAV, RIAM, RAP, JNK, CREB, CD40, MEK1/2, MEKK, EZRIN, HS1, SHIP, FGR2B, MEF2C, RAC.

For readability, we display their regulatory relationships as nine overlapping modules (a gene may appear in more than one panel when it bridges modules) in Figure 11. Blue arrows denote causal edges; orange curved lines denote confounding links. Within each edge type, lighter lines indicate lower posterior probabilities.

In Tables 5 and 6, we highlight a subset of biologically plausible causal relationships (gene regulations) and confounding structure, respectively. Many of them align with well-established regulatory mechanisms in B cell development, signal transduction, and immune

response modulation. They capture not only unidirectional regulatory relationships but also feedback loops that reflect the dynamic nature of BCR signaling.

Next, we characterize higher-order regulatory motifs in the B cell receptor (BCR) signaling network inferred from the OneK1K dataset. A prominent feedback loop involves *PLCY2*, *RAC*, and *ERK1/2* (Figure 12d), reflecting the well-established coupling between calcium signaling, cytoskeletal reorganization, and MAPK activation during B cell activation [35, 40]. Such feedback interactions are known to stabilize signaling dynamics and support sustained transcriptional responses. This motif is strongly supported by the posterior, with a probability of 0.926.

We also detect a feedforward loop in which *BCR* activation drives *IKK* both directly and indirectly via *P70S6K* (Figure 12e), linking proximal antigen receptor signaling to NF- κ B pathway activation [19, 22]. This feedforward architecture enables coordinated and robust control of inflammatory signaling and has a posterior probability of 0.918.

Moreover, a cascade motif $LYN \rightarrow RAC \rightarrow ERK1/2$ (Figure 12f) captures a canonical signaling axis connecting Src-family kinase activation to MAPK-driven transcriptional programs in B cells [27, 50], with a high posterior probability of 0.949.

5 Conclusion

We have introduced MR.RGM, a Bayesian multivariable, bidirectional Mendelian randomization framework that performs network-wide causal inference and structure learning. The method explicitly accommodates unmeasured confounding and feedback (cyclic) structure, and it jointly selects and estimates (i) the directed causal network among traits, (ii) instrument-trait effects, and (iii) a residual covariance whose off-diagonal elements indicate latent confounding. Sparsity-inducing priors yield interpretable graphs and effect maps, while the fully Bayesian formulation provides uncertainty quantification for edges, effects, confounding links, and higher-order network motifs. The inference can be carried out from sufficient statistics, so the method works seamlessly with summary-level data when individual-level records are unavailable.

Extensive simulations with realistic network structure show that **MR.RGM** consistently outperforms competing approaches, delivering higher graph-recovery AUC and lower effect-estimation error as sample size grows. In horizontal pleiotropic regimes, **MR.RGM+** achieves the best performance for both graph and effect recovery and attains near-perfect accuracy in SNP-gene selection at moderate to large sample size. The confounding structure recovered from the estimated residual covariance attains AUCs close to one in large samples, demonstrating that the same posterior output simultaneously supports causal network estimation and latent-confounder mapping. Despite using MCMC, the framework is computationally competitive, scaling to sizes of typical signaling pathways within a practical runtime.

Applications to GTEx v7 skeletal muscle tissue and the OneK1K B-cell group further validate the approach: we recover high-probability causal edges including feedback loops concordant with known biology and reveal plausible latent confounding modules, all with principled uncertainty measures. Beyond individual edges, the proposed **NetworkMotif** function enables posterior inference on higher-order regulatory structures, such as feedback loops, feedforward loops, and cascades, yielding interpretable motif-level probabilities that summarize coordinated signaling mechanisms supported by existing biological literature and quantify uncertainty.

There are some remaining practical considerations. When individual-level measurements of $(\mathbf{X}, \mathbf{Y}, \mathbf{U})$ are available, **MR.RGM** can be applied directly; if covariates \mathbf{U} are unavailable, the algorithm can be used without them, as implemented in our software. For summary-level analyses, the method requires the matrices $(\mathbf{S}_{\mathbf{y}\mathbf{y}}, \mathbf{S}_{\mathbf{y}\mathbf{x}}, \mathbf{S}_{\mathbf{x}\mathbf{x}}, \mathbf{S}_{\mathbf{y}\mathbf{u}}, \mathbf{S}_{\mathbf{x}\mathbf{u}}, \mathbf{S}_{\mathbf{u}\mathbf{u}})$. In practice, covariate-related quantities such as $\mathbf{S}_{\mathbf{y}\mathbf{u}}$, $\mathbf{S}_{\mathbf{x}\mathbf{u}}$, and $\mathbf{S}_{\mathbf{u}\mathbf{u}}$ are sometimes unavailable; in such cases, the method can be run without covariates, as in the individual-level setting. The trait–trait covariance $\mathbf{S}_{\mathbf{y}\mathbf{y}}$ can be reliably estimated as long as each pair of traits is measured in at least one study, even if different pairs come from different cohorts. A common limitation is that $\mathbf{S}_{\mathbf{y}\mathbf{x}}$ may exclude trans-SNP associations because many GWAS only report genome-wide significant hits; this is inherent to summary-level MR and implies that the method performs best when a reasonably dense set of SNP–trait associations is available. When in-sample LD ($\mathbf{S}_{\mathbf{x}\mathbf{x}}$) is unavailable and external reference LD must be used, population

mismatch may introduce LD misspecification. This can be mitigated by selecting a reference panel matched on ancestry, or by modeling $\mathbf{S}_{\mathbf{xx}}$ as a latent positive-definite matrix—e.g., with a Wishart or inverse-Wishart prior centered at the observed reference LD, so that LD uncertainty is propagated into the posterior. Finally, although the present work focuses on continuous traits (e.g., gene expression), the framework can be extended to binary or categorical complex traits using standard data-augmentation strategies such as Pólya–Gamma augmentation for logistic models or probit-based latent-variable formulations.

Taken together, these strengths and considerations position `MR.RGM` as a flexible and powerful computational tool for network-wide Mendelian randomization in modern genomic and transcriptomic studies, supporting inference at both the edge and motif levels, with clear avenues for extension to complex traits and large-scale biobank analyses.

Data and Code Availability

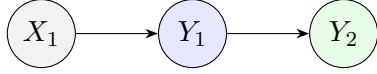
R package availability. The full implementation of the proposed Bayesian Mendelian randomization framework is publicly available as the `MR.RGM` R package. The package includes functionality for posterior inference, causal graph estimation, uncertainty quantification, and network motif analysis, and can be accessed via:

- CRAN: <https://cran.r-project.org/package=MR.RGM>
- GitHub: <https://github.com/bitansa/MR.RGM>

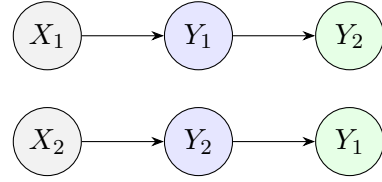
Reproducibility of simulations and real data analyses. All simulation code and analysis scripts used to generate the results in this paper are available at:

- <https://github.com/bitansa/MR.RGM>

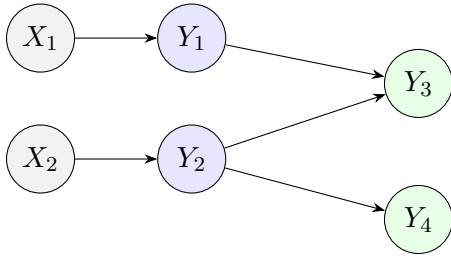
The repository contains scripts to reproduce all simulation studies and real data analyses, along with detailed documentation and software version information.



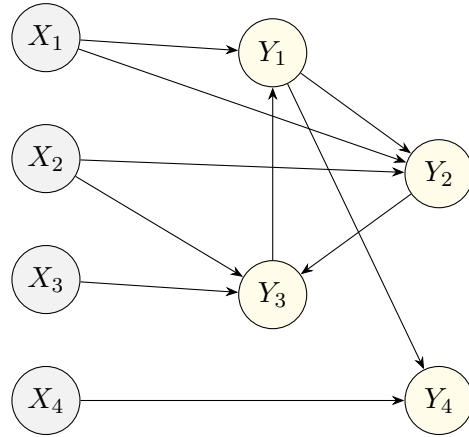
(a) Classical MR: one exposure (Y_1) and one outcome (Y_2) with instrument X_1 . The direction between exposure and outcome is fixed a priori.



(b) Bidirectional MR: two *separate* MR analyses ($Y_1 \rightarrow Y_2$ and $Y_2 \rightarrow Y_1$), each requiring its own instrument.



(c) MVMR: exposures (Y_1, Y_2) each with its own instrument; both influence Y_3 , and Y_2 additionally influences Y_4 . Typically, the direction between exposure and outcomes are fixed a priori.



(d) Propsoed MR.RGM: supports directed cycles, horizontal pleiotropy, and flexible trait–trait interactions with arbitrary directions (no pre-specification of exposure vs outcome is required).

Figure 1: Conceptual comparison of Mendelian randomization frameworks. (a)–(c) require pre-specified exposure and outcome roles. (a) and (c) do not allow feedback loops. (d) the proposed MR.RGM supports feedback loops, while allowing all traits to be modeled simultaneously without pre-specifying causal direction. Horizontal pleiotropy and unmeasured confounding are handled with principled approach as well.

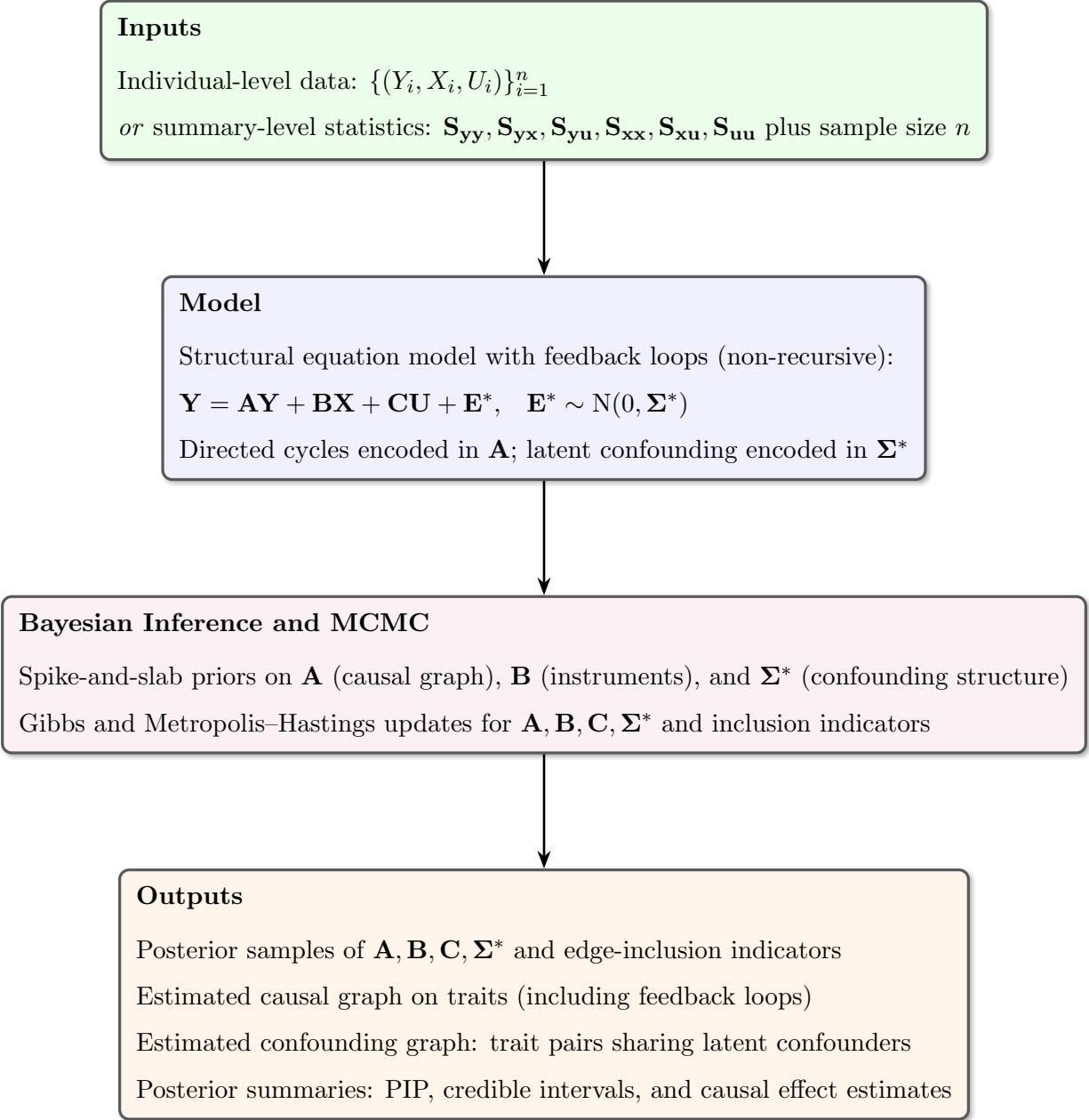
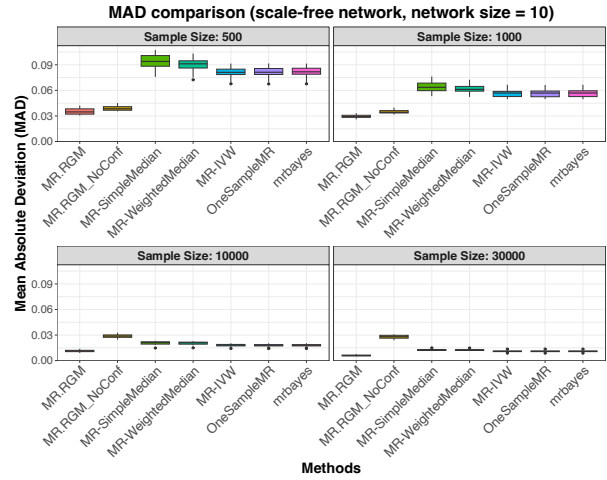
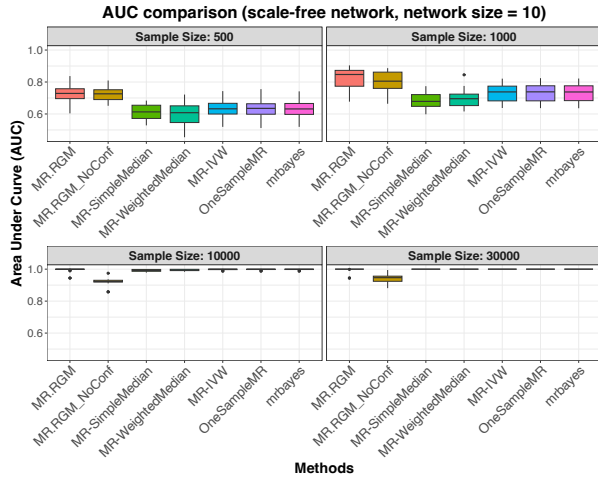


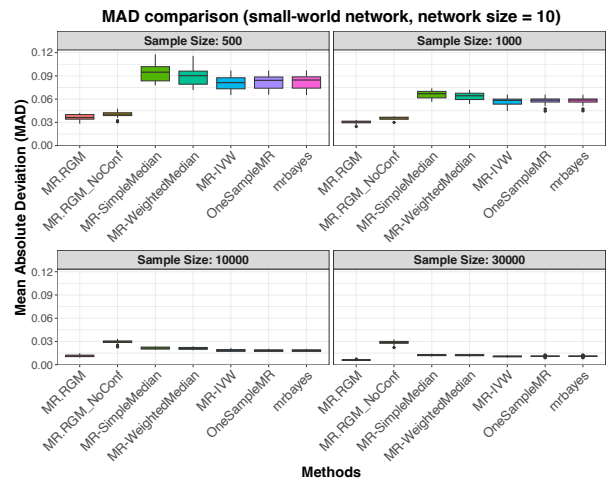
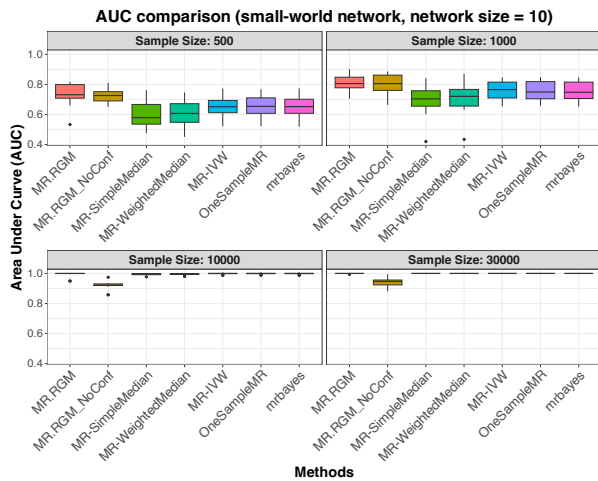
Figure 2: Overview of the proposed MR.RGM workflow. The method can take either individual-level data ($\mathbf{Y}, \mathbf{X}, \mathbf{U}$) or summary-level second-moment statistics plus sample size n as input. These are plugged into a structural equation model with directed cycles and correlated errors. Spike-and-slab priors and MCMC are then used to infer the causal graph, the latent confounding structure, and the causal effects, along with their corresponding uncertainties.



(a) Graph recovery: boxplots of AUC by method (x-axis) and sample size (facets; $n \in \{500, 1000, 10000, 30000\}$).

(b) Causal effect estimation: boxplots of MAD by method (x-axis) and sample size (facets; $n \in \{500, 1000, 10000, 30000\}$).

Figure 3: Scale-free network with feedback loops and unmeasured confounding, with network size $p=10$. (a) AUC for graph recovery; (b) MAD for causal effect estimation.



(a) Graph recovery: AUC by method (x-axis) and sample size (facets; $n \in \{500, 1000, 10000, 30000\}$).

(b) Causal effect estimation: MAD by method (x-axis) and sample size (facets; $n \in \{500, 1000, 10000, 30000\}$).

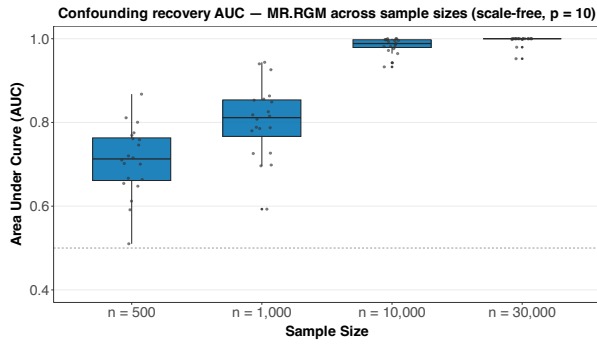
Figure 4: Small-world network with feedback loops and unmeasured confounding, with network size $p=10$. (a) AUC for graph recovery; (b) MAD for causal effect estimation.

Setting	Method	AUC	TPR	FDR	MCC
n = 500	MR.RGM	0.732 (0.055)	0.472 (0.108)	0.536 (0.096)	0.331 (0.114)
	MR.RGM_NoConf	0.718 (0.045)	0.494 (0.085)	0.605 (0.058)	0.281 (0.077)
	MR-SimpleMedian	0.612 (0.047)	0.093 (0.067)	0.397 (0.264)	0.161 (0.109)
	MR-WeightedMedian	0.601 (0.073)	0.111 (0.072)	0.500 (0.278)	0.154 (0.136)
	MR-IVW	0.631 (0.057)	0.182 (0.092)	0.508 (0.219)	0.199 (0.135)
	OneSampleMR	0.633 (0.060)	0.188 (0.093)	0.506 (0.223)	0.205 (0.141)
	mrbayes	0.630 (0.058)	0.185 (0.093)	0.504 (0.218)	0.203 (0.134)
n = 1000	MR.RGM	0.824 (0.067)	0.537 (0.096)	0.428 (0.100)	0.445 (0.111)
	MR.RGM_NoConf	0.789 (0.073)	0.585 (0.110)	0.547 (0.090)	0.371 (0.121)
	MR-SimpleMedian	0.681 (0.050)	0.164 (0.075)	0.358 (0.206)	0.246 (0.107)
	MR-WeightedMedian	0.695 (0.057)	0.188 (0.079)	0.402 (0.184)	0.251 (0.107)
	MR-IVW	0.731 (0.055)	0.265 (0.097)	0.454 (0.203)	0.281 (0.152)
	OneSampleMR	0.732 (0.055)	0.259 (0.087)	0.439 (0.212)	0.284 (0.146)
	mrbayes	0.731 (0.055)	0.265 (0.097)	0.463 (0.201)	0.277 (0.151)
n = 10000	MR.RGM	0.993 (0.017)	0.972 (0.042)	0.033 (0.041)	0.962 (0.046)
	MR.RGM_NoConf	0.918 (0.030)	0.906 (0.080)	0.485 (0.060)	0.579 (0.072)
	MR-SimpleMedian	0.992 (0.007)	0.957 (0.047)	0.139 (0.082)	0.882 (0.071)
	MR-WeightedMedian	0.994 (0.005)	0.969 (0.042)	0.128 (0.083)	0.897 (0.066)
	MR-IVW	0.998 (0.003)	0.994 (0.017)	0.175 (0.078)	0.878 (0.054)
	OneSampleMR	0.998 (0.003)	0.994 (0.017)	0.172 (0.072)	0.881 (0.050)
	mrbayes	0.998 (0.003)	0.994 (0.017)	0.174 (0.076)	0.880 (0.053)
n = 30000	MR.RGM	0.994 (0.017)	0.988 (0.030)	0.000 (0.000)	0.992 (0.019)
	MR.RGM_NoConf	0.939 (0.030)	0.920 (0.052)	0.452 (0.056)	0.617 (0.058)
	MR-SimpleMedian	1.000 (0.000)	1.000 (0.000)	0.140 (0.068)	0.907 (0.047)
	MR-WeightedMedian	1.000 (0.000)	1.000 (0.000)	0.154 (0.077)	0.897 (0.054)
	MR-IVW	1.000 (0.000)	1.000 (0.000)	0.201 (0.061)	0.864 (0.044)
	OneSampleMR	1.000 (0.000)	1.000 (0.000)	0.201 (0.061)	0.864 (0.044)
	mrbayes	1.000 (0.000)	1.000 (0.000)	0.200 (0.060)	0.865 (0.043)

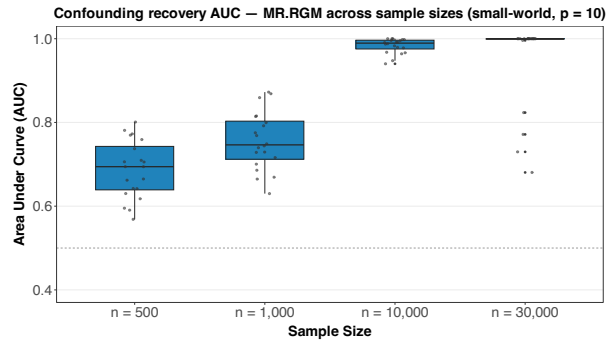
Table 1: Graph recovery performance in a scale-free network with feedback loops and un-measured confounding, with network size $p = 10$.

Setting	Method	MaxAbsDev	MeanAbsDev	MeanSqDev
n = 500	MR.RGM	0.173 (0.043)	0.035 (0.004)	0.002 (0.001)
	MR.RGM_NoConf	0.179 (0.045)	0.039 (0.003)	0.003 (0.001)
	MR-SimpleMedian	0.315 (0.053)	0.094 (0.009)	0.014 (0.002)
	MR-WeightedMedian	0.309 (0.059)	0.090 (0.009)	0.013 (0.002)
	MR-IVW	0.287 (0.051)	0.081 (0.006)	0.010 (0.002)
	OneSampleMR	0.285 (0.049)	0.081 (0.006)	0.010 (0.002)
	mrbayes	0.286 (0.049)	0.081 (0.006)	0.010 (0.002)
n = 1000	MR.RGM	0.130 (0.018)	0.030 (0.002)	0.002 (0.0003)
	MR.RGM_NoConf	0.154 (0.023)	0.035 (0.002)	0.002 (0.0002)
	MR-SimpleMedian	0.225 (0.037)	0.064 (0.006)	0.007 (0.001)
	MR-WeightedMedian	0.215 (0.037)	0.061 (0.005)	0.006 (0.001)
	MR-IVW	0.191 (0.033)	0.056 (0.004)	0.005 (0.001)
	OneSampleMR	0.192 (0.031)	0.056 (0.004)	0.005 (0.001)
	mrbayes	0.192 (0.032)	0.056 (0.004)	0.005 (0.001)
n = 10000	MR.RGM	0.059 (0.015)	0.011 (0.001)	0.0003 (0.0001)
	MR.RGM_NoConf	0.102 (0.013)	0.029 (0.002)	0.001 (0.0001)
	MR-SimpleMedian	0.071 (0.011)	0.021 (0.002)	0.001 (0.0001)
	MR-WeightedMedian	0.069 (0.011)	0.020 (0.002)	0.001 (0.0001)
	MR-IVW	0.063 (0.009)	0.018 (0.002)	0.001 (0.0001)
	OneSampleMR	0.063 (0.010)	0.018 (0.002)	0.0005 (0.0001)
	mrbayes	0.063 (0.010)	0.018 (0.002)	0.0005 (0.0001)
n = 30000	MR.RGM	0.030 (0.018)	0.006 (0.001)	0.00007 (0.00003)
	MR.RGM_NoConf	0.094 (0.011)	0.028 (0.002)	0.001 (0.0001)
	MR-SimpleMedian	0.041 (0.005)	0.013 (0.001)	0.0002 (0.0001)
	MR-WeightedMedian	0.040 (0.005)	0.013 (0.001)	0.0002 (0.0001)
	MR-IVW	0.038 (0.006)	0.011 (0.001)	0.0002 (0.0001)
	OneSampleMR	0.037 (0.005)	0.011 (0.001)	0.0002 (0.00003)
	mrbayes	0.037 (0.005)	0.011 (0.001)	0.0002 (0.00003)

Table 2: Causal effect estimation performance in a scale-free network with feedback loops and unmeasured confounding, with network size $p = 10$.

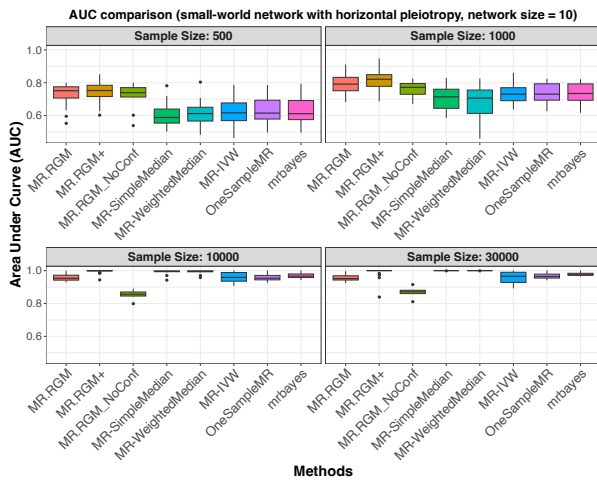


(a) Scale-free network: AUC across sample sizes ($n \in \{500, 1000, 10000, 30000\}$).

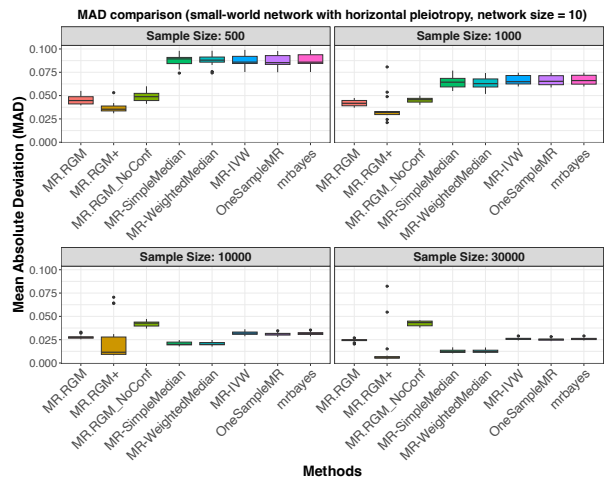


(b) Small-world network: AUC across sample sizes ($n \in \{500, 1000, 10000, 30000\}$).

Figure 5: Confounding structure recovery performance using MR.RGM under feedback loops and unmeasured confounding, with network size $p = 10$. (a) Scale-free; (b) Small-world.



(a) Graph recovery: AUC by method (x-axis) and sample size (facets; $n \in \{500, 1000, 10000, 30000\}$).



(b) Causal effect estimation: MAD by method (x-axis) and sample size (facets; $n \in \{500, 1000, 10000, 30000\}$).

Figure 6: Small-world network with feedback loops, unmeasured confounding, and horizontal pleiotropy, with network size $p=10$. (a) AUC for graph recovery; (b) MAD for causal effect estimation.

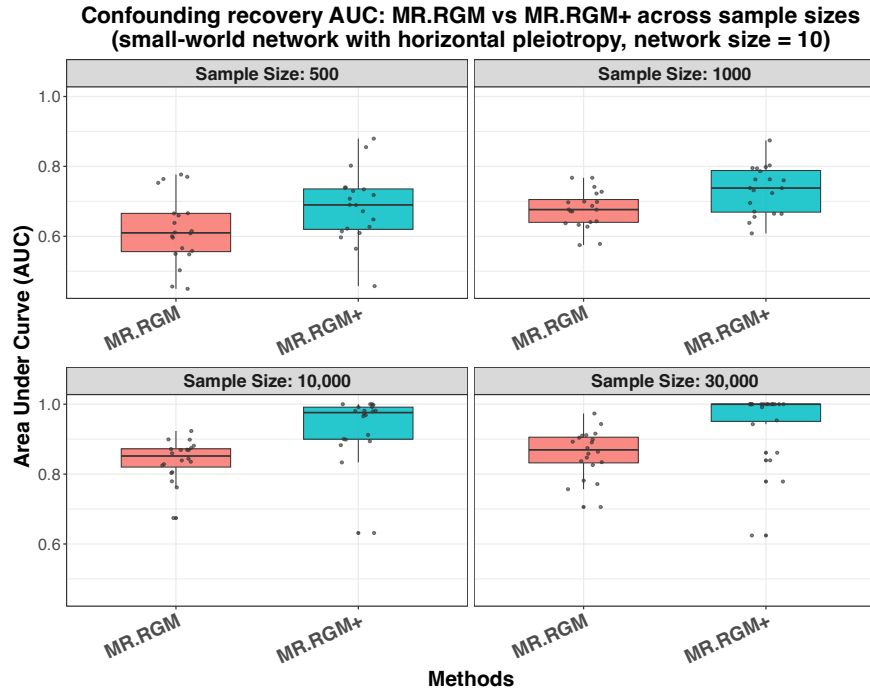


Figure 7: Confounding structure recovery performance using MR.RGM and MR.RGM+ in a small-world network with feedback loops, unmeasured confounding, and horizontal pleiotropy, with network size $p=10$. Boxplots of AUC by method (x-axis) and sample size (facets; $n \in \{500, 1000, 10000, 30000\}$).

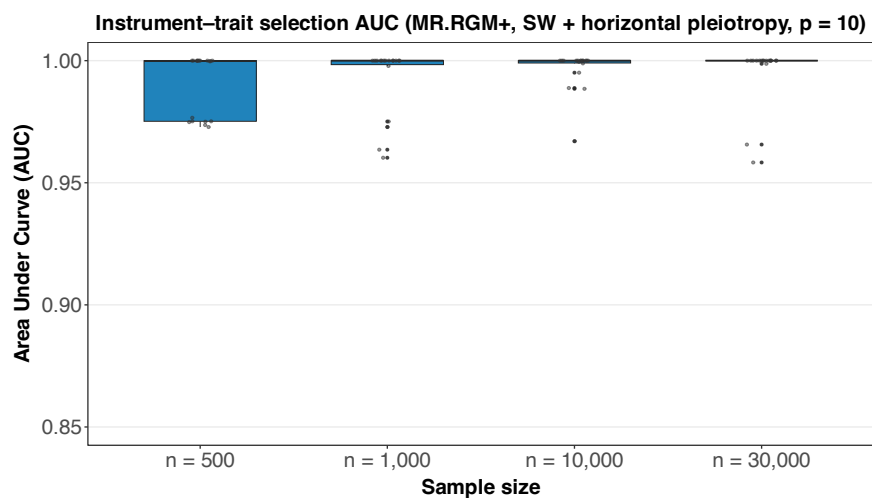


Figure 8: Instrument-trait selection performance using MR.RGM+ in a small-world network with feedback loops, unmeasured confounding, and horizontal pleiotropy, with network size $p=10$. Boxplots of AUC across sample sizes ($n \in \{500, 1000, 10000, 30000\}$).

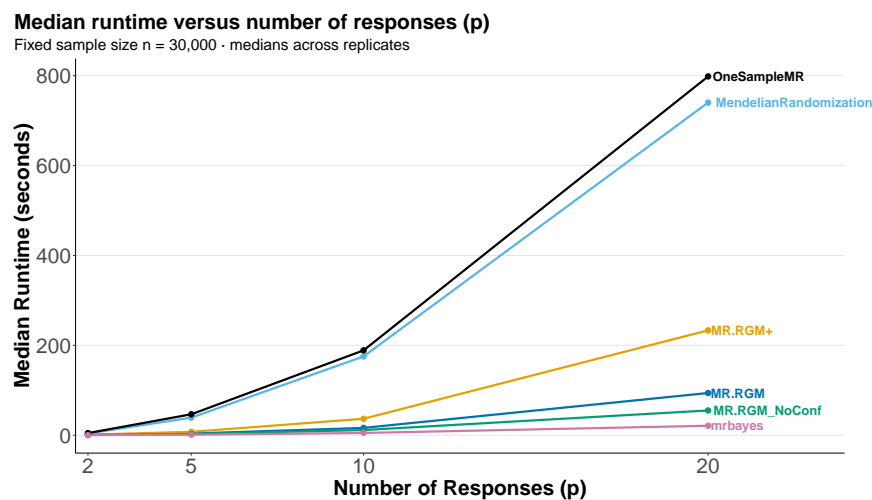


Figure 9: **Median runtime versus number of traits.** Lines show median wall-clock runtime (seconds) over 20 runs for each method as p increases ($p \in \{2, 5, 10, 20\}$) with fixed $n = 30,000$. Experiments were conducted in RStudio on an Apple M2 Pro machine (10-core CPU, 3.5 GHz) with 16 GB unified memory.

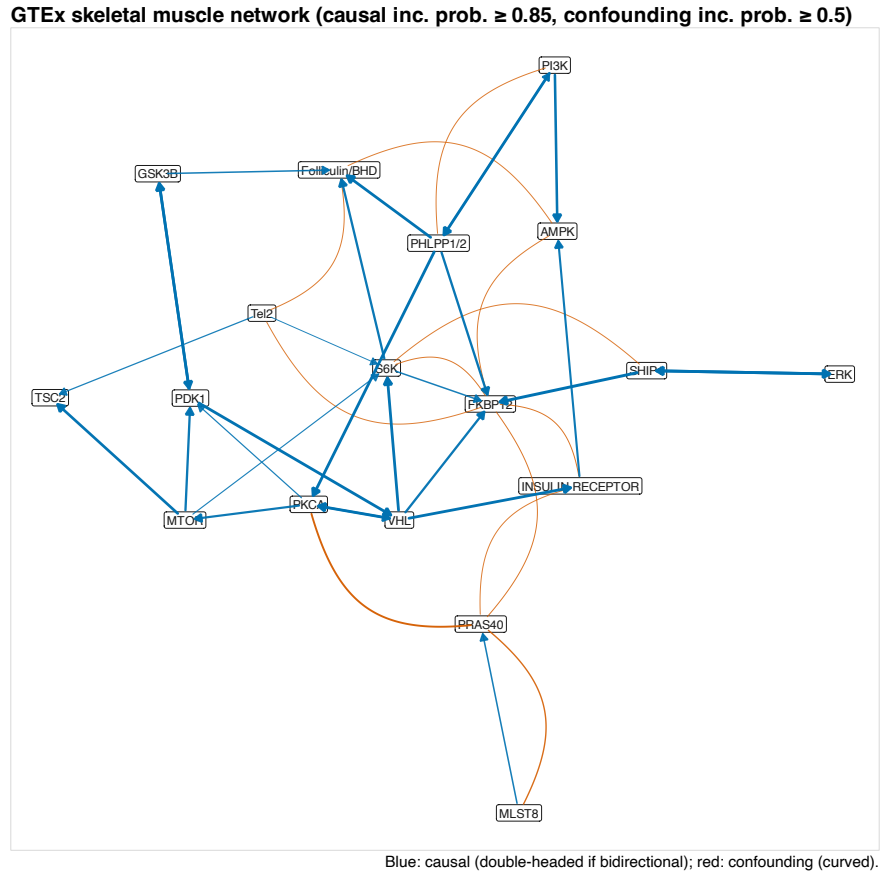


Figure 10: GTEEx skeletal muscle mTOR signaling network. For clarity, we only display causal edges with inclusion probability ≥ 0.85 and confounding edges with inclusion probability ≥ 0.50 . Blue arrows: causal edges (double-headed if bidirectional). Orange curved edges: latent confounding links. Edge color shading reflects posterior support.

Gene Regulation	PIP	Biological Interpretation
<i>MTOR</i> → <i>S6K</i>	0.871	One of the most prominent and canonical interactions in the <i>mTORC1</i> pathway is the phosphorylation of ribosomal protein <i>S6K</i> by <i>mTOR</i> . This activation is essential for promoting protein synthesis and cell growth [30].
<i>MTOR</i> → <i>PDK1</i>	0.950	<i>MTOR</i> has been shown to regulate <i>PDK1</i> activity, particularly under nutrient and growth factor stimulation. This regulatory axis is crucial for coordinating upstream <i>Akt</i> signaling and <i>mTORC1</i> activation [31].
<i>INSULIN RECEPTOR</i> → <i>AMPK</i>	0.937	While insulin signaling is primarily known for activating the <i>PI3K–Akt–mTOR</i> pathway, it also directly suppresses <i>AMPK</i> activity via <i>PI3K–Akt</i> -mediated inhibitory phosphorylation of <i>AMPKα</i> at Ser485/491 in insulin-responsive tissues [53].
<i>PI3K</i> → <i>AMPK</i>	0.968	<i>PI3K</i> activates <i>Akt</i> , which in turn inhibits/modulates <i>AMPK</i> [53]. In human skeletal muscle, <i>PI3K–Akt</i> signaling reduces <i>AMPK</i> activity via inhibitory phosphorylation on <i>AMPKα</i> Ser485/491, coordinating glucose transport and broader metabolic programs.
<i>VHL</i> → <i>INSULIN RECEPTOR</i>	0.984	The tumor suppressor <i>VHL</i> regulates hypoxia-inducible factors (HIFs), which in turn affect insulin sensitivity and receptor expression, linking <i>VHL</i> to metabolic regulation [16].
<i>PHLPP1/2</i> → <i>PKCA</i>	0.987	<i>PHLPP</i> phosphatases dephosphorylate <i>PKC</i> isoforms, including <i>PKCA</i> , playing a role in signal termination downstream of <i>PI3K/Akt</i> [32].
<i>Tel2</i> → <i>TSC2</i>	0.878	<i>Tel2</i> , part of the TTT complex, stabilizes PIKK proteins such as <i>mTOR</i> . By influencing <i>mTOR</i> stability, <i>Tel2</i> indirectly affects <i>TSC2</i> through <i>mTOR</i> -mediated regulation [48].
<i>MLST8</i> → <i>PRAS40</i>	0.899	<i>MLST8</i> is a core component of <i>mTORC1</i> and <i>mTORC2</i> . Through its scaffolding function, it modulates assembly of complexes that regulate <i>PRAS40</i> , a known <i>mTORC1</i> inhibitor [54].
<i>GSK3B</i> ⇌ <i>PDK1</i>	0.974 / 0.989	<i>GSK3B</i> and <i>PDK1</i> operate in a reciprocal regulatory relationship. <i>PDK1</i> phosphorylates <i>GSK3B</i> (Ser9), facilitating insulin signaling. Conversely, elevated <i>GSK3B</i> activity can negatively regulate upstream insulin signaling, including <i>PDK1</i> , through feedback mechanisms affecting IRS stability and <i>Akt</i> activation [28, 31].
<i>ERK</i> ⇌ <i>SHIP1</i>	0.987 / 0.987	<i>SHIP1</i> inhibits <i>ERK</i> activation by reducing <i>PI3K/PIP3</i> signaling. Conversely, <i>ERK</i> regulates <i>SHIP1</i> expression and phosphorylation, forming a negative feedback loop. Though most direct evidence comes from immune cells, the loop is likely conserved in skeletal muscle given shared pathways [11, 37].

Table 3: A few key gene regulatory relationships identified from the GTEx v7 skeletal muscle dataset, along with their posterior inclusion probabilities (PIPs) and biological validation.

Confounding	PIP	Biological Interpretation
<i>MTOR</i> – <i>TSC2</i>	0.525	<i>MTOR</i> and <i>TSC2</i> are part of the same regulatory axis wherein <i>TSC2</i> negatively regulates <i>mTORC1</i> activity. Their interaction is modulated by <i>AMPK</i> and insulin signaling, making their co-expression sensitive to metabolic state and upstream energy-sensing signals, a plausible source of shared confounding [45].
<i>PDK1</i> – <i>S6K</i>	0.501	In human skeletal muscle, both <i>PDK1</i> and <i>S6K</i> are activated downstream of <i>insulin/PI3K–Akt–mTOR</i> signaling. While <i>PDK1</i> can directly phosphorylate <i>S6K1</i> , their correlation at the systems level is more likely driven by confounding through shared upstream inputs, particularly insulin- and growth factor-mediated <i>PI3K</i> activity. Thus, rather than reflecting a direct causal dependency, their association in muscle tissue may arise from coordinated regulation of the anabolic signaling network [1].
<i>Folliculin/BHD</i> – <i>PRAS40</i>	0.503	Both <i>Folliculin (BHD)</i> and <i>PRAS40</i> negatively regulate <i>mTORC1</i> in response to metabolic cues and are phosphorylated in response to <i>AMPK/Akt</i> signaling. Their activities intersect through nutrient-sensing regulatory feedbacks, suggesting coordinated regulation and shared latent influences [51].
<i>MTOR</i> – <i>FKBP12</i>	0.501	<i>FKBP12</i> is a well-characterized binding partner of <i>MTOR</i> , crucial for rapamycin-mediated inhibition of <i>mTORC1</i> . Their expression is often correlated under rapamycin treatment and nutrient signaling, indicative of potential shared upstream regulatory programs [42].

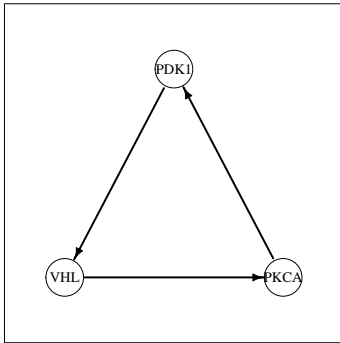
Table 4: A few biologically plausible confounding structures inferred from the GTEx v7 skeletal muscle dataset, presented with their posterior inclusion probabilities (PIPs) and supporting biological validation.

Regulation	PIP	Biological Interpretation
$PYK2 \rightarrow SYK$	0.981	<i>PYK2</i> (also known as <i>PTK2B</i>) is a calcium-sensitive non-receptor tyrosine kinase that plays a regulatory role in immune cell signaling. In B cells, <i>PYK2</i> is activated downstream of integrin and BCR engagement and has been shown to facilitate the recruitment and activation of <i>SYK</i> by phosphorylating ITAMs and forming signaling complexes with <i>SYK</i> and other adaptors. This upstream role positions <i>PYK2</i> as a modulator of <i>SYK</i> -mediated signaling cascades, particularly in integrin-enhanced or adhesion-dependent B cell responses [50].
$CBL \rightarrow DOK1$	0.994	<i>CBL</i> , an E3 ubiquitin ligase, is recruited to signaling complexes downstream of the BCR where it associates with tyrosine-phosphorylated <i>DOK1</i> . This interaction promotes ubiquitination and degradation of <i>DOK1</i> , modulating its role as a negative regulator of <i>Ras</i> and <i>PI3K</i> signaling. Through this regulation, <i>CBL</i> fine-tunes BCR signaling by limiting <i>DOK1</i> 's inhibitory effects on <i>MAPK</i> and survival pathways, ensuring balance between activation and attenuation of B cell responses [29].
$PIP3 \rightarrow AKT$	0.883	In B cells, <i>PIP3</i> generated by <i>PI3K</i> recruits <i>AKT</i> to the membrane via its PH domain, where it becomes activated by phosphorylation. This is central to cell survival and metabolic regulation [46].
$CD19 \rightarrow PI3K$	0.949	<i>CD19</i> serves as a coreceptor for BCR signaling and amplifies signal transduction by recruiting <i>PI3K</i> . It directly binds the p85 regulatory subunit of <i>PI3K</i> upon phosphorylation, enhancing <i>PIP3</i> production and facilitating activation of downstream effectors such as <i>AKT</i> and <i>BTK</i> in B cells [23].
$ERK1/2 \rightarrow JUN$	0.927	<i>ERK1/2</i> , part of the <i>MAPK</i> cascade, phosphorylates <i>c-JUN</i> , a component of the <i>AP-1</i> transcription factor complex. In activated B cells, this phosphorylation increases <i>JUN</i> transcriptional activity, promoting expression of genes involved in proliferation, differentiation, and survival [40].
$PI3K \rightarrow AKT$	0.857	The <i>PI3K</i> - <i>AKT</i> signaling axis is central in B cell biology. Upon activation by coreceptors or cytokines, <i>PI3K</i> catalyzes production of <i>PIP3</i> , which recruits and activates <i>AKT</i> . This supports survival, proliferation, and metabolic adaptation [36].
$NFKB \rightleftharpoons IKB$	0.714 / 0.928	In resting B cells, <i>IKB</i> binds and retains <i>NFKB</i> in the cytoplasm. Upon BCR or <i>CD40</i> stimulation, <i>IKB</i> is phosphorylated and degraded, allowing <i>NFKB</i> to translocate to the nucleus and drive expression of inflammatory and survival genes. <i>NFKB</i> also induces <i>IKB</i> , forming a well-characterized negative feedback loop [19].
$PKC \rightleftharpoons CAMK$	0.705 / 0.889	<i>PKC</i> and <i>CAMK</i> pathways intersect in calcium signaling. <i>PKC</i> modulates intracellular calcium flux and influences <i>CAMK</i> activation, while <i>CAMK</i> regulates calcium-sensitive <i>PKC</i> isoforms. In B cells, this bidirectional interaction integrates signals from membrane engagement and intracellular messengers [35].
$PLCY2 \rightleftharpoons PI3K$	0.693 / 0.772	<i>PLCY2</i> and <i>PI3K</i> form a feedback module in BCR signaling. <i>PI3K</i> -generated <i>PIP3</i> recruits and activates <i>PLCY2</i> , which hydrolyzes <i>PIP2</i> to produce <i>DAG</i> and <i>IP3</i> . These propagate further signaling, and <i>DAG</i> -mediated pathways (e.g., <i>RasGRP</i>) can modulate <i>PI3K</i> activity, closing the loop [57].
$RIAM \rightleftharpoons RAP$	0.897 / 0.606	<i>RIAM</i> is a <i>Rap1</i> effector mediating inside-out integrin activation. <i>RAP</i> -GTP binds and activates <i>RIAM</i> , which recruits talin to promote integrin conformational changes. Feedback arises as <i>RIAM</i> can influence <i>RAP</i> activity via cytoskeletal and membrane localization effects in lymphocytes [7].
$JNK \rightleftharpoons CREB$	0.687 / 0.695	<i>JNK</i> phosphorylates <i>CREB</i> under stress or immune activation. Activated <i>CREB</i> drives expression of survival and inflammation-related genes, some of which (e.g., <i>c-Jun</i>) feed back into <i>MAPK/JNK</i> signaling. This bidirectional loop supports adaptive responses to antigenic stimulation in B cells [26, 59].
$CD40 \rightleftharpoons NFKB$	0.569 / 0.901	<i>CD40</i> engagement activates canonical and non-canonical <i>NFKB</i> pathways, promoting survival, class switching, and cytokine production. In turn, <i>NFKB</i> upregulates <i>CD40</i> intermediates, reinforcing activation [22].

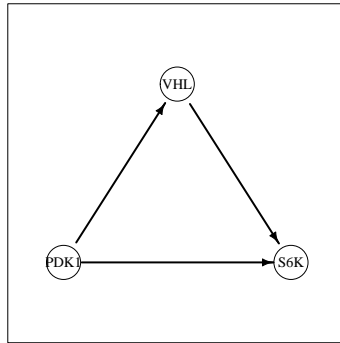
Table 5: A few key gene regulatory relationships identified from the OneK1K B-cell dataset, along with their posterior inclusion probabilities (PIPs) and biological validation.

Confounding	PIP	Biological Interpretation
<i>MEK1/2</i> – <i>ERK1/2</i>	0.498	In B cells, both <i>MEK1/2</i> (<i>MAP2K1/2</i>) and <i>ERK1/2</i> are co-activated by <i>Ras-Raf</i> signaling following BCR stimulation. Their correlation likely reflects confounding via shared <i>Ras-Raf</i> inputs that simultaneously activate <i>MEK1/2</i> and <i>ERK1/2</i> [27].
<i>MEKK</i> – <i>JNK</i>	0.494	<i>MEKK</i> (<i>MAP3K1</i>) and <i>JNK</i> (<i>MAPK8/9</i>) are key kinases in the <i>MAPK</i> signaling cascade in B cells. Their activation is strongly coordinated through shared upstream regulators, notably the CBM (CARMA1–BCL10–MALT1) complex and <i>PKCB</i> -mediated BCR signaling. The correlation between <i>MEKK</i> and <i>JNK</i> likely reflects confounding by common upstream effectors, as both respond to antigen receptor stimulation and stress signals [15].
<i>EZRIN</i> – <i>HS1</i>	0.508	<i>EZRIN</i> links membrane proteins to the actin cytoskeleton, while <i>HS1</i> regulates actin remodeling in hematopoietic cells. Both proteins are co-regulated during immune synapse formation in B cells through calcium and <i>PI3K</i> signaling. Their correlation likely arises from confounding by cytoskeletal remodeling pathways [18].
<i>PLCY2</i> – <i>VAV</i>	0.491	<i>PLCY2</i> hydrolyzes <i>PIP₂</i> to trigger calcium release, while <i>VAV</i> is a GEF that activates <i>Rac</i> and cytoskeletal rearrangements. Both are simultaneously recruited to the BCR signalosome via <i>SYK</i> and <i>BLNK</i> , suggesting that their association reflects confounding through this shared scaffold [56].
<i>SHIP</i> – <i>FGR2B</i>	0.492	<i>SHIP</i> is an inositol phosphatase recruited by the inhibitory receptor <i>FGR2B</i> . Their correlation is expected since <i>FGR2B</i> engagement recruits <i>SHIP</i> via ITIM phosphorylation by <i>LYN</i> . Thus, their co-regulation is driven by shared <i>LYN</i> kinase activity, creating a confounding structure [3].
<i>CREB</i> – <i>MEF2C</i>	0.487	<i>CREB</i> is activated downstream of <i>PKA/ERK</i> , while <i>MEF2C</i> responds to <i>CAMK</i> and <i>MAPK</i> signals. Both transcription factors are co-activated by BCR-induced calcium influx and <i>MAPK</i> cascades, producing correlated activity through shared upstream inputs rather than direct interaction [25].
<i>RAC</i> – <i>PYK2</i>	0.486	<i>RAC</i> is a small GTPase that controls actin dynamics, while <i>PYK2</i> is a focal adhesion kinase activated by calcium and integrin signaling. In B cells, both are regulated downstream of <i>VAV</i> and calcium signals during immune synapse formation. Their association likely reflects confounding by BCR-driven adhesion and cytoskeletal pathways [50].

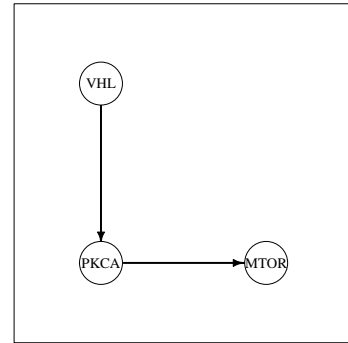
Table 6: A few biologically plausible confounding structures inferred from the OneK1K B-cell dataset, presented with their posterior inclusion probabilities (PIPs) and supporting biological validation.



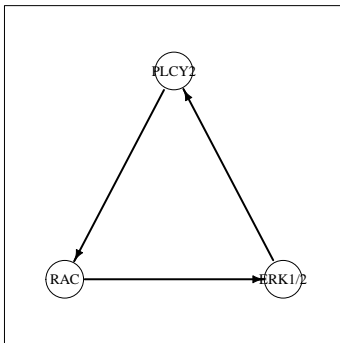
(a) GTEx feedback motif ($PDK1-VHL-PKCA$; $p = 0.854$).



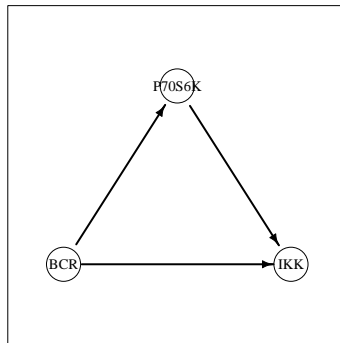
(b) GTEx feedforward motif ($PDK1-VHL-S6K$; $p = 0.724$).



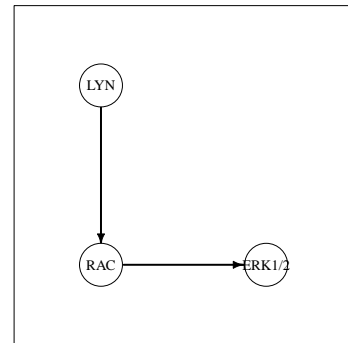
(c) GTEx cascade motif ($VHL-PKCA-MTOR$; $p = 0.931$).



(d) OneK1K feedback motif ($PLCY2-RAC-ERK1/2$; $p = 0.926$).



(e) OneK1K feedforward motif ($BCR-P70S6K-IKK$; $p = 0.918$).



(f) OneK1K cascade motif ($LYN-RAC-ERK1/2$; $p = 0.949$).

Figure 12: Motif-level summaries inferred using the `NetworkMotif` function. Each subfigure shows a feedback loop, feedforward loop, or cascade, whose uncertainty is quantified by its posterior probability calculated from posterior samples (the proportion of posterior draws in which all edges comprising the motif are simultaneously present).

References

- [1] Dario R Alessi, Michael T Kozlowski, Qi Ping Weng, Nick Morrice, and Joseph Avruch. 3-Phosphoinositide-dependent protein kinase 1 (PDK1) phosphorylates and activates the p70 S6 kinase in vivo and in vitro. *Current Biology*, 8(2):69–81, 1998.
- [2] Aruna Balendran, Roderick Currie, C Gordon Armstrong, Joseph Avruch, and Dario R Alessi. Evidence that 3-phosphoinositide-dependent protein kinase-1 mediates phosphorylation of p70 s6 kinase in vivo at thr-412 as well as thr-252. *Journal of Biological Chemistry*, 274(52):37400–37406, 1999.
- [3] Ashley N. Barlev, Susan Malkiel, Izumi Kurata-Sato, Annemarie L. Dorjée, Jolien Surmond, and Betty Diamond. Fc γ RIIB regulates autoantibody responses by limiting marginal zone B cell activation. *Journal of Clinical Investigation*, 132(17):e157250, 2022.
- [4] Robert L Basman. A GENERALIZED CLASSICAL METHOD OF LINEAR ESTIMATION OF COEFFICIENTS IN A STRUCTURAL EQUATION. *Econometrica: Journal of the Econometric Society*, pages 77–83, 1957.
- [5] Jack Bowden, George Davey Smith, and Stephen Burgess. Mendelian randomization with invalid instruments: effect estimation and bias detection through Egger regression. *International Journal of Epidemiology*, 44(2):512–525, 2015.
- [6] Jack Bowden, George Davey Smith, Philip C Haycock, and Stephen Burgess. Consistent Estimation in Mendelian Randomization with Some Invalid Instruments Using a Weighted Median Estimator. *Genetic Epidemiology*, 40(4):304–314, May 2016.
- [7] Thomas Bromberger, Sarah Klapproth, Ina Rohwedder, Jasmin Weber, Robert Pick, Laura Mittmann, Soo Jin Min-Weißenhorn, Christoph A Reichel, Christoph Scheiermann, Markus Sperandio, and Markus Moser. Binding of Rap1 and Riam to Talin1 Fine-Tune β 2 Integrin Activity During Leukocyte Trafficking. *Frontiers in Immunology*, 12:702345, 2021. eCollection 2021.

- [8] Stephen Burgess, Adam Butterworth, and Simon G Thompson. Mendelian randomization analysis with multiple genetic variants using summarized data. *Genetic Epidemiology*, 37(7):658–665, 2013.
- [9] Stephen Burgess and Olena Yavorska. *MendelianRandomization: Mendelian Randomization Package*, 2024. R package version 0.10.0.
- [10] Xiaodong Cai, Juan Andrés Bazerque, and Georgios B. Giannakis. Inference of Gene Regulatory Networks with Sparse Structural Equation Models Exploiting Genetic Perturbations. *PLOS Computational Biology*, 9(5):e1003068, 2013.
- [11] Kevin K. Caldwell, Marcos Sosa, and Colin T. Buckley. Identification of mitogen-activated protein kinase docking sites in enzymes that metabolize phosphatidylinositols and inositol phosphates. *Cell Communication and Signaling*, 4:2, January 2006.
- [12] Li Chen, Chunlin Li, Xiaotong Shen, and Wei Pan. Discovery and inference of a causal network with hidden confounding. *Journal of the American Statistical Association*, 119(548):2572–2584, November 2023.
- [13] GTEx Consortium. Genetic effects on gene expression across human tissues. *Nature*, 550:204–213, 2017.
- [14] George Davey Smith and Shah Ebrahim. ‘Mendelian randomization’: can genetic epidemiology contribute to understanding environmental determinants of disease? *International Journal of Epidemiology*, 32(1):1–22, Feb 2003.
- [15] Roger J Davis. Signal transduction by the JNK group of MAP kinases. *Cell*, 103(2):239–252, 2000.
- [16] Jenny E Gunton. Hypoxia-inducible factors and diabetes. *Journal of Clinical Investigation*, 130(10):5063–5073, 2020.
- [17] Fernando Pires Hartwig, George Davey Smith, and Jack Bowden. Robust inference in summary data Mendelian randomization via the zero modal pleiotropy assumption. *International Journal of Epidemiology*, 46(6):1985–1998, Dec 2017.

- [18] Naomi E. Harwood and Facundo D. Batista. The Cytoskeleton Coordinates the Early Events of B-cell Activation. *Cold Spring Harbor Perspectives in Biology*, 3(2):a002360, February 2011.
- [19] Matthew S. Hayden and Sankar Ghosh. Signaling to NF-kappaB. *Genes & Development*, 18(18):2195–2224, 2004.
- [20] Gibran Hemani, Jie Zheng, Benjamin Elsworth, et al. *TwoSampleMR: Perform Mendelian Randomization using Two-Sample Summary Data*, 2025. R package version 0.6.8.
- [21] Gibran Hemani, Jie Zheng, Benjamin Elsworth, Katherine H. Wade, David Baird, Verena Haberland, Caroline Laurin, Stephen Burgess, Jack Bowden, Rebecca Langdon, Vanessa Y. Tan, Joshua Yarmolinsky, Hanan A. Shibab, Nicholas J. Timpson, David M. Evans, Caroline Relton, Richard M. Martin, George Davey Smith, Tom R. Gaunt, Paul C. Haycock, and The MR-Base Collaboration. The mr-base platform supports systematic causal inference across the human phenome. *eLife*, 7:e34408, 2018.
- [22] Bruce S. Hostager and Gail A. Bishop. CD40-Mediated Activation of the NF- κ B2 Pathway. *Frontiers in Immunology*, 4:376, 2013.
- [23] Kazunori Inabe and Tomohiro Kurosaki. Tyrosine phosphorylation of B-cell adaptor for phosphoinositide 3-kinase is required for Akt activation in response to CD19 engagement. *Blood*, 99(2):584–589, 2002.
- [24] Wei Jin, Yang Ni, Amanda B. Spence, Leah H. Rubin, and Yanxun Xu. Directed Cyclic Graphs for Simultaneous Discovery of Time-Lagged and Instantaneous Causality from Longitudinal Data Using Instrumental Variables. *Journal of Machine Learning Research*, 26(22):1–62, 2025.
- [25] Dustin Khiem, Jason G. Cyster, John J. Schwarz, and Brian L. Black. A p38 MAPK-MEF2C pathway regulates B-cell proliferation. *Proceedings of the National Academy of Sciences of the United States of America*, 105(44):17067–17072, Nov 2008.

- [26] Ji-Hye Kim, A-reum Hong, Yo-Han Kim, Hanju Yoo, Sang-Wook Kang, Sung Eun Chang, and Youngsup Song. Jnk suppresses melanogenesis by interfering with CREB-regulated transcription coactivator 3-dependent MITF expression. *Theranostics*, 10(9):4017–4029, 2020.
- [27] Walter Kolch. Meaningful relationships: the regulation of the Ras/Raf/MEK/ERK pathway by protein interactions. *Biochemical Journal*, 351(Pt 2):289–305, Oct 2000.
- [28] Ziva Liberman and Hagit Eldar-Finkelman. Serine 332 phosphorylation of insulin receptor substrate-1 by glycogen synthase kinase-3 attenuates insulin signaling. *Journal of Biological Chemistry*, 280(6):4422–4428, 2005. Epub 2004 Nov 30.
- [29] Mark L. Jr. Lupher, Navin Rao, Michael J. Eck, and Hamid Band. The Cbl protooncoprotein: a negative regulator of immune receptor signal transduction. *Immunology Today*, 20(8):375–382, 1999.
- [30] Xiaojun Ma and John Blenis. Molecular mechanisms of mTOR-mediated translational control. *Nature Reviews Molecular Cell Biology*, 10(4):307–318, 2009.
- [31] Brendan D Manning and Lewis C Cantley. AKT/PKB signaling: navigating downstream. *Cell*, 129(7):1261–1274, 2007.
- [32] Alexandra C. Newton. Protein kinase c: poised to signal. *American Journal of Physiology - Endocrinology and Metabolism*, 298(3):E395–E402, March 2010.
- [33] Yang Ni, Yuan Ji, and Peter Müller. Reciprocal Graphical Models for Integrative Gene Regulatory Network Analysis. *Bayesian Analysis*, 13(4):1095–1110, 2018.
- [34] Yang Ni, Peter Müller, Yitan Zhu, and Yuan Ji. Heterogeneous reciprocal graphical models. *Biometrics*, 74(2):606–615, 2018.
- [35] Masatsugu Oh-Hora and Anjana Rao. Calcium signaling in lymphocytes. *Current Opinion in Immunology*, 20(3):250–258, Jun 2008.

- [36] Klaus Okkenhaug and Bart Vanhaesebroeck. PI3K in lymphocyte development, differentiation and activation. *Nature Reviews Immunology*, 3(4):317–330, 2003.
- [37] Christopher J. Ong, Andrew Ming-Lum, Matt Nodwell, Ali Ghanipour, Lu Yang, David E. Williams, Joseph Kim, Loutfig Demirjian, Pooran Qasimi, Jens Ruschmann, Li-Ping Cao, Kewei Ma, Stephen W. Chung, Vincent Duronio, Raymond J. Andersen, Gerald Krystal, and Alice L.-F. Mui. Small-molecule agonists of SHIP1 inhibit the phosphoinositide 3-kinase pathway in hematopoietic cells. *Blood*, 110(6):1942–1949, September 2007. Epub 2007 May 14.
- [38] Tom Palmer, Wes Spiller, and Eleanor Sanderson. *OneSampleMR: One Sample Mendelian Randomization and Instrumental Variable Analyses*. MRC Integrative Epidemiology Unit, University of Bristol, Bristol, UK, 2023.
- [39] Judea Pearl. Causal diagrams for empirical research. *Biometrika*, 82(4):669–688, 1995.
- [40] Robert Jr. Roskoski. ERK1/2 MAP kinases: Structure, function, and regulation. *Pharmacological Research*, 66(2):105–143, 2012.
- [41] Saptarshi Roy, Raymond KW Wong, and Yang Ni. Directed Cyclic Graph for Causal Discovery from Multivariate Functional Data. *Advances in Neural Information Processing Systems*, 36:42762–42774, 2023.
- [42] David M. Sabatini, Helena Erdjument-Bromage, Maria Lui, Paul Tempst, and Solomon H. Snyder. RAFT1: a mammalian protein that binds to FKBP12 in a rapamycin-dependent fashion and is homologous to yeast tors. *Cell*, 78(1):35–43, 1994.
- [43] Eleanor Sanderson, George Davey Smith, Frank Windmeijer, and Jack Bowden. An examination of multivariable Mendelian randomization in the single-sample and two-sample summary data settings. *International Journal of Epidemiology*, 48(3):713–727, 2019.
- [44] Bitan Sarkar and Yang Ni. MR.RGM: an R package for fitting Bayesian multivariate bidirectional Mendelian randomization networks. *Bioinformatics*, 41(4):btaf130, 2025.

- [45] Robert A Saxton and David M Sabatini. mTOR Signaling in Growth, Metabolism, and Disease. *Cell*, 168(6):960–976, Mar 2017.
- [46] Lomon So and David A. Fruman. PI3K Signaling in B and T Lymphocytes: New Developments and Therapeutic Advances. *Biochemical Journal*, 442(3):465–481, Mar 2012.
- [47] Peter Spirtes. Directed cyclic graphical representations of feedback models. In *Proceedings of the Eleventh Conference on Uncertainty in Artificial Intelligence (UAI)*, pages 491–498, San Francisco, CA, USA, 1995. Morgan Kaufmann Publishers Inc.
- [48] Hiroyuki Takai, Richard C Wang, Kaori K Takai, Haijuan Yang, and Titia de Lange. Tel2 regulates the stability of PI3K-related protein kinases. *Cell*, 131(7):1248–1259, Dec 2007.
- [49] Henri Theil. Repeated Least Squares Applied to Complete Equation Systems. Technical report, Central Planning Bureau, The Hague, 1953. Mimeographed report.
- [50] Kathy W K Tse, May Dang-Lawson, Rosaline L Lee, Doris Vong, Anica Bulic, Leonard Buckbinder, and Michael R Gold. B cell receptor-induced phosphorylation of Pyk2 and focal adhesion kinase involves integrins and the Rap GTPases and is required for B cell spreading. *Journal of Biological Chemistry*, 284(34):22865–22877, 2009.
- [51] Zhi-Yang Tsun, Liron Bar-Peled, Lynne Chantranupong, Roberto Zoncu, Tim Wang, Choah Kim, Eric Spooner, and David M Sabatini. The Folliculin Tumor Suppressor Is a GAP for the RagC/D GTPases That Signal Amino Acid Levels to mTORC1. *Molecular Cell*, 52(4):495–505, 2013.
- [52] Okezie Uche-Ikonne, Frank Dondelinger, and Tom Palmer. Software Application Profile: Bayesian estimation of inverse variance weighted and MR-Egger models for two-sample Mendelian randomization studies – mrbayes. *International Journal of Epidemiology*, 50(1):43–49, 2021.

- [53] Rudy J Valentine, Kimberly A Coughlan, Neil B Ruderman, and Asish K Saha. Insulin inhibits AMPK activity and phosphorylates AMPK Ser^{485/491} through Akt in hepatocytes, myotubes and incubated rat skeletal muscle. *Archives of Biochemistry and Biophysics*, 562:62–69, 2014.
- [54] Emilie Vander Haar, Seong-Il Lee, Sricharan Bandhakavi, Timothy J. Griffin, and Do-Hyung Kim. Insulin signalling to mTOR mediated by the Akt/PKB substrate PRAS40. *Nature Cell Biology*, 9(3):316–323, 2007.
- [55] Marie Verbanck, Chia-Yen Chen, Benjamin Neale, and Ron Do. Detection of widespread horizontal pleiotropy in causal relationships inferred from Mendelian randomization between complex traits and diseases. *Nature Genetics*, 50(5):693–698, 2018.
- [56] Michele Weber, Bebhinn Treanor, David Depoil, Hisaaki Shinohara, Naomi E. Harwood, Masaki Hikida, Tomohiro Kurosaki, and Facundo D. Batista. Phospholipase C- γ 2 and Vav cooperate within signaling microclusters to propagate B cell spreading in response to membrane-bound antigen. *Journal of Experimental Medicine*, 205(4):853–868, Apr 2008.
- [57] Yue Wen, Yukai Jing, Lu Yang, Danqing Kang, Panpan Jiang, Na Li, Jiali Cheng, Jingwen Li, Xingbo Li, Zican Peng, Xizi Sun, Heather Miller, Zhiwei Sui, Quan Gong, Boxu Ren, Wei Yin, and Chaohong Liu. The regulators of BCR signaling during B cell activation. *Blood Science*, 1(2):119–129, 2019.
- [58] Seyhan Yazar, Jorge Alquicira-Hernández, Kelvin Wing, Anna Senabouth, Genevieve Gordon, Søren Andersen, Qian Lu, Alex Rowson, Trevor Taylor, Luke Clarke, Laura Maccora, Chia Chen, Angus Cook, Jia Ye, Kate Fairfax, Alex Hewitt, and Joseph Powell. Single-cell eQTL mapping identifies cell type-specific control of autoimmune disease. *Science*, 376(6589):eabf3041, 2022.
- [59] J Zhang, Q Wang, N Zhu, M Yu, B Shen, J Xiang, and A Lin. Cyclic AMP inhibits JNK activation by CREB-mediated induction of c-FLIP(L) and MKP-1, thereby antagonizing UV-induced apoptosis. *Cell Death & Differentiation*, 15:1654–1662, 2008.

- [60] Zhihong Zhu, Zhili Zheng, Futao Zhang, Yang Wu, Maciej Trzaskowski, Robert Maier, Matthew R. Robinson, John J. McGrath, Peter M. Visscher, Naomi R. Wray, and Jian Yang. Causal associations between risk factors and common diseases inferred from GWAS summary data. *Nature Communications*, 9:224, 2018.
- [61] Verena Zuber, Toinét Cronjé, Na Cai, Dipender Gill, and Leonardo Bottolo. Bayesian causal graphical model for joint Mendelian randomization analysis of multiple exposures and outcomes. *The American Journal of Human Genetics*, 112(5):1173–1198, 2025.

Supplementary Material: Multivariable Bidirectional Mendelian Randomization via Bayesian Directed Cyclic Graphical Model with Correlated Errors

Bitan Sarkar¹, Yuchao Jiang¹, Tian Ge², and Yang Ni³

¹Department of Statistics, Texas A&M University, College Station, TX, USA

²Psychiatric and Neurodevelopmental Genetics Unit, Center for Genomic Medicine, Massachusetts General Hospital, Boston, MA, USA

³Department of Statistics and Data Sciences, University of Texas at Austin, Austin, TX, USA

1 Conditional Likelihood in terms of Summary-Level Data

We rewrite the conditional Gaussian likelihood entirely in terms of the empirical second-moment matrices \mathbf{S}_{yy} , \mathbf{S}_{yx} , \mathbf{S}_{yu} , \mathbf{S}_{xx} , \mathbf{S}_{xu} , \mathbf{S}_{uu} so that inference can be performed from summary-level data (and per-iteration work no longer scales with sample size). Thus, expanding the quadratic form, and converting sums to traces yields:

$$\begin{aligned}
 & p(\{\mathbf{Y}_i\}_{i=1}^n | \{\mathbf{X}_i\}_{i=1}^n, \{\mathbf{U}_i\}_{i=1}^n, \mathbf{A}, \mathbf{B}, \mathbf{C}, \Sigma^*) \\
 &= \prod_{i=1}^n \mathcal{N}(\mathbf{Y}_i | (\mathbf{I}_p - \mathbf{A})^{-1} \mathbf{B} \mathbf{X}_i + (\mathbf{I}_p - \mathbf{A})^{-1} \mathbf{C} \mathbf{U}_i, (\mathbf{I}_p - \mathbf{A})^{-1} \Sigma^* (\mathbf{I}_p - \mathbf{A})^{-\mathbf{T}}) \\
 &= \prod_{i=1}^n \mathcal{N}((\mathbf{I}_p - \mathbf{A}) \mathbf{Y}_i - \mathbf{B} \mathbf{X}_i - \mathbf{C} \mathbf{U}_i | \mathbf{0}, \Sigma^*) \cdot |\det(\mathbf{I}_p - \mathbf{A})| \\
 &= \prod_{i=1}^n (2\pi)^{-p/2} \det(\Sigma^*)^{-1/2} |\det(\mathbf{I}_p - \mathbf{A})| \exp\left(-\frac{1}{2} [(\mathbf{I}_p - \mathbf{A}) \mathbf{Y}_i - \mathbf{B} \mathbf{X}_i - \mathbf{C} \mathbf{U}_i]^{\mathbf{T}} \right. \\
 &\quad \left. \Sigma^{*-1} [(\mathbf{I}_p - \mathbf{A}) \mathbf{Y}_i - \mathbf{B} \mathbf{X}_i - \mathbf{C} \mathbf{U}_i] \right) \\
 &= (2\pi)^{-\frac{np}{2}} \cdot \det(\Sigma^*)^{-\frac{n}{2}} \cdot |\det(\mathbf{I}_p - \mathbf{A})|^n \cdot \exp\left(-\frac{1}{2} \sum_{i=1}^n [(\mathbf{I}_p - \mathbf{A}) \mathbf{Y}_i - \mathbf{B} \mathbf{X}_i - \mathbf{C} \mathbf{U}_i]^{\mathbf{T}} \right. \\
 &\quad \left. \Sigma^{*-1} [(\mathbf{I}_p - \mathbf{A}) \mathbf{Y}_i - \mathbf{B} \mathbf{X}_i - \mathbf{C} \mathbf{U}_i] \right) \\
 &= (2\pi)^{-\frac{np}{2}} \cdot \det(\Sigma^*)^{-\frac{n}{2}} \cdot |\det(\mathbf{I}_p - \mathbf{A})|^n \cdot \exp\left(-\frac{1}{2} \sum_{i=1}^n [\mathbf{Y}_i^{\mathbf{T}} (\mathbf{I}_p - \mathbf{A})^{\mathbf{T}} \Sigma^{*-1} (\mathbf{I}_p - \mathbf{A}) \mathbf{Y}_i \right. \\
 &\quad - 2 \mathbf{X}_i^{\mathbf{T}} \mathbf{B}^{\mathbf{T}} \Sigma^{*-1} (\mathbf{I}_p - \mathbf{A}) \mathbf{Y}_i + \mathbf{X}_i^{\mathbf{T}} \mathbf{B}^{\mathbf{T}} \Sigma^{*-1} \mathbf{B} \mathbf{X}_i - 2 \mathbf{U}_i^{\mathbf{T}} \mathbf{C}^{\mathbf{T}} \Sigma^{*-1} (\mathbf{I}_p - \mathbf{A}) \mathbf{Y}_i \\
 &\quad \left. + 2 \mathbf{U}_i^{\mathbf{T}} \mathbf{C}^{\mathbf{T}} \Sigma^{*-1} \mathbf{B} \mathbf{X}_i + \mathbf{U}_i^{\mathbf{T}} \mathbf{C}^{\mathbf{T}} \Sigma^{*-1} \mathbf{C} \mathbf{U}_i] \right)
 \end{aligned}$$

$$\begin{aligned}
& = (2\pi)^{-\frac{np}{2}} \cdot \det(\boldsymbol{\Sigma}^*)^{-\frac{n}{2}} \cdot |\det(\mathbf{I}_p - \mathbf{A})|^n \cdot \exp\left(-\frac{1}{2} \sum_{i=1}^n [\text{tr}(\mathbf{Y}_i^T (\mathbf{I}_p - \mathbf{A})^T \boldsymbol{\Sigma}^{*-1} (\mathbf{I}_p - \mathbf{A}) \mathbf{Y}_i) \right. \\
& \quad \left. - 2\text{tr}(\mathbf{X}_i^T \mathbf{B}^T \boldsymbol{\Sigma}^{-1} (\mathbf{I}_p - \mathbf{A}) \mathbf{Y}_i) + \text{tr}(\mathbf{X}_i^T \mathbf{B}^T \boldsymbol{\Sigma}^{-1} \mathbf{B} \mathbf{X}_i) - 2\text{tr}(\mathbf{U}_i^T \mathbf{C}^T \boldsymbol{\Sigma}^{*-1} (\mathbf{I}_p - \mathbf{A}) \mathbf{Y}_i) \right. \\
& \quad \left. + 2\text{tr}(\mathbf{U}_i^T \mathbf{C}^T \boldsymbol{\Sigma}^{*-1} \mathbf{B} \mathbf{X}_i) + \text{tr}(\mathbf{U}_i^T \mathbf{C}^T \boldsymbol{\Sigma}^{*-1} \mathbf{C} \mathbf{U}_i)]\right) \\
& = (2\pi)^{-\frac{np}{2}} \cdot \det(\boldsymbol{\Sigma}^*)^{-\frac{n}{2}} \cdot |\det(\mathbf{I}_p - \mathbf{A})|^n \cdot \exp\left(-\frac{1}{2} \sum_{i=1}^n [\text{tr}(\mathbf{Y}_i \mathbf{Y}_i^T (\mathbf{I}_p - \mathbf{A})^T \boldsymbol{\Sigma}^{*-1} (\mathbf{I}_p - \mathbf{A})) \right. \\
& \quad \left. - 2\text{tr}(\mathbf{Y}_i \mathbf{X}_i^T \mathbf{B}^T \boldsymbol{\Sigma}^{-1} (\mathbf{I}_p - \mathbf{A})) + \text{tr}(\mathbf{X}_i \mathbf{X}_i^T \mathbf{B}^T \boldsymbol{\Sigma}^{-1} \mathbf{B}) - 2\text{tr}(\mathbf{Y}_i \mathbf{U}_i^T \mathbf{C}^T \boldsymbol{\Sigma}^{*-1} (\mathbf{I}_p - \mathbf{A})) \right. \\
& \quad \left. + 2\text{tr}(\mathbf{X}_i \mathbf{U}_i^T \mathbf{C}^T \boldsymbol{\Sigma}^{*-1} \mathbf{B}) + \text{tr}(\mathbf{U}_i \mathbf{U}_i^T \mathbf{C}^T \boldsymbol{\Sigma}^{*-1} \mathbf{C})\right) \\
& = (2\pi)^{-\frac{np}{2}} \cdot \det(\boldsymbol{\Sigma}^*)^{-\frac{n}{2}} \cdot |\det(\mathbf{I}_p - \mathbf{A})|^n \cdot \exp\left(-\frac{1}{2} \left[\text{tr}\left(\sum_{i=1}^n \mathbf{Y}_i \mathbf{Y}_i^T (\mathbf{I}_p - \mathbf{A})^T \boldsymbol{\Sigma}^{*-1} (\mathbf{I}_p - \mathbf{A})\right) \right. \right. \\
& \quad \left. - 2\text{tr}\left(\sum_{i=1}^n \mathbf{Y}_i \mathbf{X}_i^T \mathbf{B}^T \boldsymbol{\Sigma}^{-1} (\mathbf{I}_p - \mathbf{A})\right) + \text{tr}\left(\sum_{i=1}^n \mathbf{X}_i \mathbf{X}_i^T \mathbf{B}^T \boldsymbol{\Sigma}^{-1} \mathbf{B}\right) \right. \\
& \quad \left. - 2\text{tr}\left(\sum_{i=1}^n \mathbf{Y}_i \mathbf{U}_i^T \mathbf{C}^T \boldsymbol{\Sigma}^{*-1} (\mathbf{I}_p - \mathbf{A})\right) + 2\text{tr}\left(\sum_{i=1}^n \mathbf{X}_i \mathbf{U}_i^T \mathbf{C}^T \boldsymbol{\Sigma}^{*-1} \mathbf{B}\right) \right. \\
& \quad \left. + \text{tr}\left(\sum_{i=1}^n \mathbf{U}_i \mathbf{U}_i^T \mathbf{C}^T \boldsymbol{\Sigma}^{*-1} \mathbf{C}\right) \right] \Bigg) \\
& = (2\pi)^{-\frac{np}{2}} \cdot \det(\boldsymbol{\Sigma}^*)^{-\frac{n}{2}} \cdot |\det(\mathbf{I}_p - \mathbf{A})|^n \cdot \exp\left(-\frac{1}{2} \left[\text{tr}(\mathbf{nS}_{yy} (\mathbf{I}_p - \mathbf{A})^T \boldsymbol{\Sigma}^{*-1} (\mathbf{I}_p - \mathbf{A})) \right. \right. \\
& \quad \left. - 2\text{tr}(\mathbf{nS}_{yx} \mathbf{B}^T \boldsymbol{\Sigma}^{*-1} (\mathbf{I}_p - \mathbf{A})) + \text{tr}(\mathbf{nS}_{xx} \mathbf{B}^T \boldsymbol{\Sigma}^{*-1} \mathbf{B}) \right. \\
& \quad \left. - 2\text{tr}(\mathbf{nS}_{yu} \mathbf{C}^T \boldsymbol{\Sigma}^{*-1} (\mathbf{I}_p - \mathbf{A})) + 2\text{tr}(\mathbf{nS}_{xu} \mathbf{C}^T \boldsymbol{\Sigma}^{*-1} \mathbf{B}) \right. \\
& \quad \left. + \text{tr}(\mathbf{nS}_{uu} \mathbf{C}^T \boldsymbol{\Sigma}^{*-1} \mathbf{C}) \right] \Bigg) \\
& = (2\pi)^{-\frac{np}{2}} \cdot \det(\boldsymbol{\Sigma}^*)^{-\frac{n}{2}} \cdot |\det(\mathbf{I}_p - \mathbf{A})|^n \cdot \exp\left(-\frac{1}{2} \left[n \cdot \left[\text{tr}(\mathbf{S}_{yy} (\mathbf{I}_p - \mathbf{A})^T \boldsymbol{\Sigma}^{*-1} (\mathbf{I}_p - \mathbf{A})) \right. \right. \right. \\
& \quad \left. - 2n \cdot \text{tr}(\mathbf{S}_{yx} \mathbf{B}^T \boldsymbol{\Sigma}^{*-1} (\mathbf{I}_p - \mathbf{A})) + n \cdot \text{tr}(\mathbf{S}_{xx} \mathbf{B}^T \boldsymbol{\Sigma}^{*-1} \mathbf{B}) \right. \\
& \quad \left. - 2n \cdot \text{tr}(\mathbf{S}_{yu} \mathbf{C}^T \boldsymbol{\Sigma}^{*-1} (\mathbf{I}_p - \mathbf{A})) + 2n \cdot \text{tr}(\mathbf{S}_{xu} \mathbf{C}^T \boldsymbol{\Sigma}^{*-1} \mathbf{B}) \right. \\
& \quad \left. + n \cdot \text{tr}(\mathbf{S}_{uu} \mathbf{C}^T \boldsymbol{\Sigma}^{*-1} \mathbf{C}) \right] \Bigg)
\end{aligned}$$

2 Detailed Prior Specifications

This section provides the full prior specifications for all model components in MR.RGM, including the causal effect matrix \mathbf{A} , the instrument–trait matrix \mathbf{B} , the covariate effect matrix \mathbf{C} , and the residual covariance matrix $\boldsymbol{\Sigma}^*$.

Priors on the causal effect matrix \mathbf{A} . We place a spike-and-slab prior on each off-diagonal entry a_{jh} of the matrix \mathbf{A} . The presence of a directed edge from Y_h to Y_j is governed by a binary

inclusion variable γ_{jh} , and the effect size a_{jh} is conditionally modeled as:

$$\begin{aligned} a_{jh} &\sim \gamma_{jh} \cdot \text{N}(0, \tau_{jh}) + (1 - \gamma_{jh}) \cdot \text{N}(0, \nu_1 \cdot \tau_{jh}), \\ \gamma_{jh} &\sim \text{Bernoulli}(\rho_{jh}) \\ \rho_{jh} &\sim \text{Beta}(a_\rho, b_\rho) \\ \sqrt{\tau_{jh}} &\sim \mathcal{C}^+(0, 1), \end{aligned}$$

where $\mathcal{C}^+(0, 1)$ is the standard half-Cauchy distribution. Here, we fix $\nu_1 \ll 1$ to ensure good separation between signals and noises. Following [2], half-Cauchy distribution can be reparameterized as:

$$x \sim \mathcal{C}^+(0, 1) \implies x^2 \mid a \sim \text{IG}(1/2, 1/a), \quad a \sim \text{IG}(1/2, 1),$$

where $\text{IG}(\cdot, \cdot)$ denotes the inverse-gamma distribution. This allows a closed-form Gibbs update.

Priors on the instrument effect matrix \mathbf{B} . When there may be horizontal pleiotropy (the violation of the exclusion restriction assumption) or weak instruments (the violation of the relevance assumption), we do not impose fixed structural zeros in \mathbf{B} but instead adopt a spike-and-slab prior for each entry of \mathbf{B} :

$$\begin{aligned} b_{jh} &\sim \phi_{jh} \cdot \text{N}(0, \eta_{jh}) + (1 - \phi_{jh}) \cdot \text{N}(0, \nu_2 \cdot \eta_{jh}), \\ \phi_{jh} &\sim \text{Bernoulli}(\psi_{jh}), \\ \psi_{jh} &\sim \text{Beta}(a_\psi, b_\psi), \\ \sqrt{\eta_{jh}} &\sim \mathcal{C}^+(0, 1), \end{aligned}$$

where $\nu_2 \ll 1$ and ϕ_{jh} indicates whether X_h is a (significant) instrument for Y_j . This prior formulation encourages sparsity in \mathbf{B} , facilitating automatic selection of valid and relevant instruments. Under the InSIDE assumption [1, 4] that the instrument effects are independent of each other, we obtain unbiased causal effect estimation. We call MR.RGM with selection on instruments MR.RGM+. Otherwise, simple normal priors are placed on the non-zero entries of \mathbf{B} .

Prior on the covariate effect matrix \mathbf{C} . We assume a conjugate matrix-normal prior on $\mathbf{C} \in \mathbb{R}^{p \times l}$:

$$\mathbf{C} \sim \text{MN}_{p \times l}(\mathbf{0}, \mathbf{\Sigma}^*, \tau \mathbf{I}_l).$$

Prior on the error covariance matrix $\mathbf{\Sigma}^*$. The error covariance matrix $\mathbf{\Sigma}^* = \mathbf{D}\mathbf{D}^T + \mathbf{\Sigma}$ combines unmeasured confounding (via \mathbf{D}) and measurement noise (via $\mathbf{\Sigma}$). Since we do not know *a priori* the number t of unmeasured confounders, we directly model $\mathbf{\Sigma}^*$ instead of modeling \mathbf{D} and $\mathbf{\Sigma}$. We introduce a binary indicator matrix $\mathbf{Z} = (z_{jh}) \in \{0, 1\}^{p \times p}$ that encodes whether the off-diagonal entry σ_{jh}^* is nonzero. The priors are specified as follows:

$$\begin{aligned} \sigma_{jh}^* &\sim z_{jh} \cdot \text{N}(0, \omega_1^2) + (1 - z_{jh}) \cdot \text{N}(0, \omega_2^2), \quad j < h, \\ z_{jh} &\sim \text{Bernoulli}(\pi), \\ \sigma_{jj}^* &\sim \text{Exp}\left(\frac{\lambda}{2}\right), \end{aligned}$$

subject to the positive-definiteness of the resulting $\mathbf{\Sigma}^*$. The hyperparameters ω_1, ω_2, π and λ control the sparsity and scale of the inferred error covariance. Following [3], we recommend setting $\omega_2 \geq 0.01$ and $\omega_1/\omega_2 \leq 1000$ to ensure numerical stability and encourage separation between signals and noises. The parameter π lies between 0 and 1, with smaller values favoring sparser structures. For the exponential prior, λ may be set to moderately large values such as 5 or 10.

3 Detailed Posterior Inference Procedure

Our MCMC consists of the following 11 updates at each iteration.

1. Update ψ_{jh} by a Gibbs transition probability. Draw $\psi_{jh} \sim \text{Beta}(\phi_{jh} + a_\psi, 1 - \phi_{jh} + b_\psi)$.
2. Update η_{jh} by a Gibbs transition probability. Draw $\epsilon \sim \text{IG}(1, 1 + 1/\eta_{jh})$ and then draw $\eta_{jh} \sim \text{IG}(1, b_{jh}^2/2 + 1/\epsilon)$ (if $\phi_{jh} = 1$) or draw $\eta_{jh} \sim \text{IG}(1, b_{jh}^2/(2 \times \nu_2) + 1/\epsilon)$ (if $\phi_{jh} = 0$).
3. Update ϕ_{jh} by a Gibbs transition probability. Draw $\phi_{jh} \sim \text{Ber}(p_\phi)$ where,

$$p_\phi = \frac{\exp(-b_{jh}^2/(2 \times \eta_{jh})) \times \psi_{jh}}{\exp(-b_{jh}^2/(2 \times \eta_{jh})) \times \psi_{jh} + \exp(-b_{jh}^2/(2 \times \nu_2 \times \eta_{jh})) \times (1 - \psi_{jh})/\sqrt{\nu_2}}.$$

4. Update b_{jh} by a random-walk Metropolis-Hastings (M-H) transition probability. Propose $\tilde{b}_{jh} \sim N(b_{jh}, \xi_b)$ where ξ_b is the proposal variance and create $\tilde{\mathbf{B}}$ from \mathbf{B} by substituting b_{jh} by \tilde{b}_{jh} . Accept \tilde{b}_{jh} with probability $\min(\alpha, 1)$ where,

$$\alpha = \frac{p\left(\{\mathbf{y}_i\}_{i=1}^n | \{\mathbf{x}_i\}_{i=1}^n, \{\mathbf{u}_i\}_{i=1}^n, \mathbf{A}, \tilde{\mathbf{B}}, \mathbf{C}, \Sigma^*\right) p(\tilde{b}_{jh} | \phi_{jh}, \eta_{jh})}{p\left(\{\mathbf{y}_i\}_{i=1}^n | \{\mathbf{x}_i\}_{i=1}^n, \{\mathbf{u}_i\}_{i=1}^n, \mathbf{A}, \mathbf{B}, \mathbf{C}, \Sigma^*\right) p(b_{jh} | \phi_{jh}, \eta_{jh})}.$$

5. Update ρ_{jh} by a Gibbs transition probability. Draw $\rho_{jh} \sim \text{Beta}(\gamma_{jh} + a_\rho, 1 - \gamma_{jh} + b_\rho)$.
6. Update τ_{jh} by a Gibbs transition probability. Draw $\epsilon \sim \text{IG}(1, 1 + 1/\tau_{jh})$ and then draw $\tau_{jh} \sim \text{IG}(1, a_{jh}^2/2 + 1/\epsilon)$ (if $\gamma_{jh} = 1$) or draw $\tau_{jh} \sim \text{IG}(1, a_{jh}^2/(2 \times \nu_1) + 1/\epsilon)$ (if $\gamma_{jh} = 0$).
7. Update γ_{jh} by a Gibbs transition probability. Draw $\gamma_{jh} \sim \text{Ber}(p_\gamma)$ where

$$p_\gamma = \frac{\exp(-a_{jh}^2/(2 \times \tau_{jh})) \times \rho_{jh}}{\exp(-a_{jh}^2/(2 \times \tau_{jh})) \times \rho_{jh} + \exp(-a_{jh}^2/(2 \times \nu_1 \times \tau_{jh})) \times (1 - \rho_{jh})/\sqrt{\nu_1}}.$$

8. Update a_{jh} by a random walk Metropolis-Hastings (M-H) transition probability. Propose $\tilde{a}_{jh} \sim N(a_{jh}, \xi_a)$ where ξ_a is the proposal variance and create $\tilde{\mathbf{A}}$ from \mathbf{A} by substituting a_{jh} by \tilde{a}_{jh} . Accept \tilde{a}_{jh} with probability $\min(\alpha, 1)$ where,

$$\alpha = \frac{p\left(\{\mathbf{y}_i\}_{i=1}^n | \{\mathbf{x}_i\}_{i=1}^n, \{\mathbf{u}_i\}_{i=1}^n, \tilde{\mathbf{A}}, \mathbf{B}, \mathbf{C}, \Sigma^*\right) p(\tilde{a}_{jh} | \gamma_{jh}, \tau_{jh}, \nu_1)}{p\left(\{\mathbf{y}_i\}_{i=1}^n | \{\mathbf{x}_i\}_{i=1}^n, \{\mathbf{u}_i\}_{i=1}^n, \mathbf{A}, \mathbf{B}, \mathbf{C}, \Sigma^*\right) p(a_{jh} | \gamma_{jh}, \tau_{jh}, \nu_1)}.$$

9. Update \mathbf{C} by a Gibbs transition probability:

$$\mathbf{C} \sim \text{MN}_{p \times l} \left([n(\mathbf{I}_p - \mathbf{A})\mathbf{S}_{yu} - n\mathbf{B}\mathbf{S}_{xu}] (n\mathbf{S}_{uu} + \tau^{-1}\mathbf{I}_l)^{-1}, \Sigma^*, (n\mathbf{S}_{uu} + \tau^{-1}\mathbf{I}_l)^{-1} \right)$$

10. Update z_{jh} for $j < h$ by a Gibbs transition probability:

$$z_{jh} \sim \text{Bernoulli}(p_z), \quad \text{where } p_z = \frac{\frac{1}{\omega_1} \exp\left(-\frac{(\sigma_{jh}^*)^2}{2\omega_1^2}\right) \cdot \pi}{\frac{1}{\omega_1} \exp\left(-\frac{(\sigma_{jh}^*)^2}{2\omega_1^2}\right) \cdot \pi + \frac{1}{\omega_2} \exp\left(-\frac{(\sigma_{jh}^*)^2}{2\omega_2^2}\right) \cdot (1 - \pi)}.$$

11. Update Σ^* by a blocked Gibbs step following [3]. We define \mathbf{S} as:

$$\begin{aligned} \mathbf{S} = & n\{(\mathbf{I}_p - \mathbf{A})\mathbf{S}_{yy}(\mathbf{I}_p - \mathbf{A})^\top - (\mathbf{I}_p - \mathbf{A})\mathbf{S}_{yx}\mathbf{B}^\top - \mathbf{B}\mathbf{S}_{yx}^\top(\mathbf{I}_p - \mathbf{A})^\top + \mathbf{B}\mathbf{S}_{xx}\mathbf{B}^\top + \mathbf{C}\mathbf{S}_{uu}\mathbf{C}^\top \\ & - (\mathbf{I}_p - \mathbf{A})\mathbf{S}_{yu}\mathbf{C}^\top - \mathbf{C}\mathbf{S}_{yu}^\top(\mathbf{I}_p - \mathbf{A})^\top + \mathbf{B}\mathbf{S}_{xu}\mathbf{C}^\top + \mathbf{C}\mathbf{S}_{xu}^\top\mathbf{B}^\top\} + \mathbf{C}\mathbf{C}^\top/\tau. \end{aligned}$$

For each column $j = 1, \dots, p$, partition Σ^* , \mathbf{S} , and \mathbf{Z} as:

$$\Sigma^* = \begin{bmatrix} \Sigma_{11} & \sigma_{12} \\ \sigma_{12}^\top & \sigma_{22} \end{bmatrix}, \quad \mathbf{S} = \begin{bmatrix} \mathbf{S}_{11} & s_{12} \\ s_{12}^\top & s_{22} \end{bmatrix}, \quad \mathbf{Z} = \begin{bmatrix} \mathbf{Z}_{11} & z_{12} \\ z_{12}^\top & z_{22} \end{bmatrix}.$$

Let $u = \sigma_{12}$, and define $v = \sigma_{22} - \sigma_{12}^\top \Sigma_{11}^{-1} \sigma_{12}$. Then the full conditionals are:

$$\begin{aligned} u \mid \cdot & \sim N((\mathbf{\Omega} + \text{diag}(v_{12}^{-1}))^{-1}w, (\mathbf{\Omega} + \text{diag}(v_{12}^{-1}))^{-1}), \\ v \mid \cdot & \sim \text{GIG}\left(1 - \frac{n}{2}, \lambda, u^\top \Sigma_{11}^{-1} \mathbf{S}_{11} \Sigma_{11}^{-1} u - 2s_{12}^\top \Sigma_{11}^{-1} u + s_{22}\right), \end{aligned}$$

where $w = \Sigma_{11}^{-1} s_{12} v^{-1}$ and $\mathbf{\Omega} = \Sigma_{11}^{-1} \mathbf{S}_{11} \Sigma_{11}^{-1} v^{-1} + \lambda \Sigma_{11}^{-1}$.

After MCMC, we summarize model parameters as follows:

Selection and Estimation of \mathbf{A} (Causal Effects): We compute the posterior mean of each γ_{jh} for $j \neq h$, which is an estimate of the marginal inclusion probability for a causal edge from trait h to trait j . To obtain a sparse causal graph, we can apply a threshold (e.g., 0.5) to marginal inclusion probabilities, which yields a binary adjacency matrix. The causal effect matrix \mathbf{A} is computed as the element-wise (Hadamard) product of the posterior mean of \mathbf{A} and the binary adjacency matrix, preserving effect sizes only for edges with sufficient posterior support.

Selection and Estimation of \mathbf{B} (Instrumental Effects): Similarly, we compute the posterior mean of each ϕ_{il} , which is the inclusion probability for each instrument-trait pair. We threshold it and multiply it element-wise with the posterior mean of \mathbf{B} to retain only those instrumental effects that are well-supported by the data.

Selection and Estimation of Σ^* (Residual Covariance and Confounding Structure): We compute the posterior mean of each $z_{jh} = 1$ for $j \neq h$, which is the inclusion probability for confounding between traits j and h . We threshold it and multiply it element-wise with the posterior mean of Σ^* . This results in a sparse estimate of the residual covariance matrix, identifying significant confounding effects that are supported by the data.

4 Identifiability of MR.RGM+ Under Instrument Diversity and Sparsity

Consider the SEM:

$$\mathbf{Y} = \mathbf{A}\mathbf{Y} + \mathbf{B}\mathbf{X} + \mathbf{E}^*,$$

where $\mathbf{Y} \in \mathbb{R}^p$, $\mathbf{X} \in \mathbb{R}^k$, $\mathbf{A} \in \mathbb{R}^{p \times p}$ with $\text{diag}(\mathbf{A}) = \mathbf{0}$, $\mathbf{B} \in \mathbb{R}^{p \times k}$, and $\mathbf{E}^* \sim N_p(\mathbf{0}, \Sigma^*)$. We assume $\mathbf{X} \sim (\mathbf{0}, \Sigma_{XX})$ with $\Sigma_{XX} \succ 0$, $\mathbf{X} \perp \mathbf{E}^*$, and $(\mathbf{I}_p - \mathbf{A})$ is invertible. The reduced form is:

$$\mathbf{Y} = \mathbf{\Pi}\mathbf{X} + \boldsymbol{\eta}, \quad \boldsymbol{\eta} \sim N_p(\mathbf{0}, \mathbf{\Omega}),$$

where:

$$\begin{aligned}\mathbf{\Pi} &= (\mathbf{I}_p - \mathbf{A})^{-1}\mathbf{B} \\ \mathbf{\Omega} &= (\mathbf{I}_p - \mathbf{A})^{-1}\mathbf{\Sigma}^*(\mathbf{I}_p - \mathbf{A})^{-\top}\end{aligned}\tag{1}$$

From observations, we can identify:

$$\begin{aligned}\mathbf{\Pi} &= \text{Cov}(\mathbf{Y}, \mathbf{X})\mathbf{\Sigma}_{XX}^{-1} \\ \mathbf{\Omega} &= \text{Var}(\mathbf{Y}) - \mathbf{\Pi}\mathbf{\Sigma}_{XX}\mathbf{\Pi}^\top\end{aligned}$$

Vectorize $\mathbf{B} = (\mathbf{I}_p - \mathbf{A})\mathbf{\Pi}$ by stacking its rows:

$$\text{vec}(\mathbf{B}) = \text{vec}(\mathbf{\Pi}) - \mathbf{M}\mathbf{a}$$

where $\mathbf{a} = (a_{12}, a_{13}, \dots, a_{1p}, a_{21}, a_{23}, \dots, a_{p,p-1})^\top \in \mathbb{R}^{p(p-1)}$ is the vector of off-diagonal elements of \mathbf{A} , and $\mathbf{M} \in \mathbb{R}^{pk \times p(p-1)}$ is a block diagonal matrix:

$$\mathbf{M} = \text{diag}(\mathbf{\Phi}_1, \mathbf{\Phi}_2, \dots, \mathbf{\Phi}_p),$$

where each block $\mathbf{\Phi}_j \in \mathbb{R}^{k \times (p-1)}$ corresponds to trait j and is given by:

$$\mathbf{\Phi}_j = \mathbf{\Pi}_{-j}^\top.$$

Here $\mathbf{\Pi}_{-j} \in \mathbb{R}^{(p-1) \times k}$ denotes $\mathbf{\Pi}$ with row j removed.

The block diagonal structure of \mathbf{M} implies that the identification problem can be decomposed into p independent subproblems, one for each trait j . The causal effects $\{a_{ji}\}_{i \neq j}$ can be determined independently from the zero constraints on row j of \mathbf{B} .

Lemma 1 (Rank of constraint submatrix). *Suppose Instrument Diversity holds. For any support $S := \text{supp}(\mathbf{B}) \subseteq \{1, \dots, p\} \times \{1, \dots, k\}$ with per-trait supports $S_j = \text{supp}(\mathbf{B}_{j,:}) = \{h : (j, h) \in S\}$ satisfying:*

$$|S_j^c| \geq p - 1 \quad \text{for all } j \in \{1, \dots, p\},$$

we have:

$$\text{rank}([\mathbf{M}]_{S^c,:}) = p(p - 1)$$

where $[\mathbf{M}]_{S^c,:}$ is defined as

$$[\mathbf{M}]_{S^c,:} = \text{diag}\left([\mathbf{\Phi}_1]_{S_1^c,:}, [\mathbf{\Phi}_2]_{S_2^c,:}, \dots, [\mathbf{\Phi}_p]_{S_p^c,:}\right)$$

Proof. For a block diagonal matrix, the rank is the sum of the ranks of the diagonal blocks:

$$\text{rank}([\mathbf{M}]_{S^c,:}) = \sum_{j=1}^p \text{rank}([\mathbf{\Phi}_j]_{S_j^c,:})$$

We now show that $\text{rank}([\mathbf{\Phi}_j]_{S_j^c,:}) = p - 1$ for each j .

Recall that $\mathbf{\Phi}_j = \mathbf{\Pi}_{-j}^\top \in \mathbb{R}^{k \times (p-1)}$. Thus:

$$[\mathbf{\Phi}_j]_{S_j^c,:} = [\mathbf{\Pi}_{-j}^\top]_{S_j^c,:} = (\mathbf{\Pi}_{-j, S_j^c})^\top$$

where $\mathbf{\Pi}_{-j, S_j^c} \in \mathbb{R}^{(p-1) \times |S_j^c|}$ is $\mathbf{\Pi}_{-j}$ restricted to columns in S_j^c .

Since $|S_j^c| \geq p - 1$ by assumption, the matrix $\mathbf{\Pi}_{-j, S_j^c}$ has at least $p - 1$ columns. By Instrument Diversity, any $(p - 1)$ columns of $\mathbf{\Pi}_{-j}$ are linearly independent, so:

$$\text{rank}(\mathbf{\Pi}_{-j, S_j^c}) = p - 1$$

Therefore $\text{rank}([\mathbf{\Phi}_j]_{S_j^c, \cdot}) = \text{rank}((\mathbf{\Pi}_{-j, S_j^c})^\top) = p - 1$.

Summing over all traits:

$$\text{rank}([\mathbf{M}]_{S^c, \cdot}) = \sum_{j=1}^p (p - 1) = p(p - 1)$$

□

Proof of the Identifiability Theorem

For each trait j , define:

- $\mathbf{a}_{j, -j} \in \mathbb{R}^{p-1}$: the off-diagonal entries $(a_{j1}, \dots, a_{j, j-1}, a_{j, j+1}, \dots, a_{jp})^\top$
- $\mathbf{b}_j \in \mathbb{R}^k$: row j of \mathbf{B}
- $\boldsymbol{\pi}_j \in \mathbb{R}^k$: row j of $\mathbf{\Pi}$
- $S_j \subseteq \{1, \dots, k\}$: the support of row j of \mathbf{B} , i.e., $S_j := \text{supp}(\mathbf{b}_j)$
- $S_j^c = \{1, \dots, k\} \setminus S_j$: instruments where $b_{jh} = 0$
- $s_j := \|\mathbf{b}_j\|_0 = |S_j|$: the number of nonzero entries in \mathbf{b}_j

The constraint for trait j is:

$$\mathbf{b}_j = \boldsymbol{\pi}_j - \mathbf{\Phi}_j \mathbf{a}_{j, -j}$$

The zero constraints (for $h \in S_j^c$) give:

$$[\boldsymbol{\pi}_j]_{S_j^c} = [\mathbf{\Phi}_j]_{S_j^c, \cdot} \mathbf{a}_{j, -j}$$

This is a system of $|S_j^c| = k - s_j$ linear equations in $p - 1$ unknowns. For a fixed support S_j with $|S_j| = s_j$, this system has $k - s_j$ equations in $p - 1$ unknowns. For it to have at most one solution, we need it to be overdetermined or just-determined, i.e., $k - s_j \geq p - 1$ and hence $s_j \leq k - p + 1$. Under Instrument Diversity and $|S_j^c| = k - s_j \geq p - 1$, Lemma 1 guarantees full column rank $\text{rank}([\mathbf{\Phi}_j]_{S_j^c, \cdot}) = p - 1$. Thus, for each trait j with $s_j \leq k - p + 1$, there exists at most one $\mathbf{a}_{j, -j}$ satisfying the constraints for support S_j .

Since a priori we do not know the support S_j , we need to prove the uniqueness of the solution across all possible supports. Suppose for contradiction that two solutions exist, (\mathbf{A}, \mathbf{B}) and $(\mathbf{A}', \mathbf{B}')$ with $\mathbf{A} \neq \mathbf{A}'$, $|S_j| \leq s_j$, and $|S'_j| \leq s_j$ for all j . Since $\mathbf{A} \neq \mathbf{A}'$, there exists at least one trait j^* such that $\mathbf{a}_{j^*, -j^*} \neq \mathbf{a}'_{j^*, -j^*}$. For this trait, both $\mathbf{a}_{j^*, -j^*}$ and $\mathbf{a}'_{j^*, -j^*}$ must satisfy zero constraints on their respective supports.

Zero constraints for (\mathbf{A}, \mathbf{B}) : For every $h \in (S_{j^*})^c$, we have $b_{j^*h} = 0$, which means:

$$\pi_{j^*h} = \sum_{i \neq j^*} a_{j^*i} \pi_{ih} \quad \text{for all } h \in (S_{j^*})^c$$

Zero constraints for $(\mathbf{A}', \mathbf{B}')$: For every $h \in (S'_{j^*})^c$, we have $b'_{j^*h} = 0$, which means:

$$\pi_{j^*h} = \sum_{i \neq j^*} a'_{j^*i} \pi_{ih} \quad \text{for all } h \in (S'_{j^*})^c$$

Constraints on the intersection: Define:

$$(S_{j^*})^c \cap (S'_{j^*})^c = (S_{j^*} \cup S'_{j^*})^c$$

This is the set of instruments where *both* \mathbf{B} and \mathbf{B}' have zeros in row j^* . On this intersection, *both* $\mathbf{a}_{j^*, -j^*}$ and $\mathbf{a}'_{j^*, -j^*}$ must satisfy the *same* linear constraints:

$$[\boldsymbol{\pi}_{j^*}]_{(S_{j^*} \cup S'_{j^*})^c} = [\boldsymbol{\Phi}_{j^*}]_{(S_{j^*} \cup S'_{j^*})^c, :} \mathbf{a}_{j^*, -j^*} \quad (2)$$

By inclusion-exclusion:

$$|S_{j^*} \cup S'_{j^*}| \leq |S_{j^*}| + |S'_{j^*}| \leq s_{j^*} + s_{j^*} = 2s_{j^*}$$

Therefore:

$$|(S_{j^*} \cup S'_{j^*})^c| = k - |S_{j^*} \cup S'_{j^*}| \geq k - 2s_{j^*}$$

For the system (2) to have at most one solution, we need it to be overdetermined or just-determined:

$$\begin{aligned} |(S_{j^*} \cup S'_{j^*})^c| &\geq p - 1 \\ k - 2s_{j^*} &\geq p - 1 \\ s_{j^*} &\leq \frac{k - p + 1}{2} \end{aligned}$$

Under Instrument Diversity, if $|(S_{j^*} \cup S'_{j^*})^c| \geq p - 1$, then Lemma 1 guarantees:

$$\text{rank}([\boldsymbol{\Phi}_{j^*}]_{(S_{j^*} \cup S'_{j^*})^c, :}) = p - 1$$

Therefore, the system has at most one solution. Since both $\mathbf{a}_{j^*, -j^*}$ and $\mathbf{a}'_{j^*, -j^*}$ satisfy the system, $\mathbf{a}_{j^*, -j^*} = \mathbf{a}'_{j^*, -j^*}$, which contradicts our assumption that $\mathbf{a}_{j^*, -j^*} \neq \mathbf{a}'_{j^*, -j^*}$. Since the argument must hold for any trait j^* where \mathbf{A} and \mathbf{A}' differ, we require:

$$s_j \leq \frac{k - p + 1}{2} \quad \text{for all } j \in \{1, \dots, p\}$$

or equivalently,

$$\max_j s_j \leq \frac{k - p + 1}{2},$$

which is our sparsity assumption.

Once \mathbf{A} is identified, $\boldsymbol{\Sigma}^*$ is uniquely determined:

$$\boldsymbol{\Sigma}^* = (\mathbf{I}_p - \mathbf{A})\boldsymbol{\Omega}(\mathbf{I}_p - \mathbf{A})^\top$$

where $\boldsymbol{\Omega}$ is identified from the data via (1).

This completes the proof.

Remark 1 (Tightness of the bound). The per-trait bound is tight in the following sense: if $s_j > (k - p + 1)/2$ for some trait j , one can construct examples where two distinct supports yield feasible solutions with different \mathbf{A} matrices.

For example, consider $p = 2$ traits and $k = 3$ instruments with:

$$\mathbf{\Pi} = \begin{pmatrix} 1 & 2 & 3 \\ 1 & 1 & 1 \end{pmatrix}$$

This satisfies Instrument Diversity (all entries non-zero). The per-trait bound requires $s_j \leq (k - p + 1)/2 = 1$.

We construct two distinct solutions, both with $s_1 = 2 > 1$. Recall that $b_{1h} = \pi_{1h} - a_{12}\pi_{2h}$.

Solution 1: Support $S_1 = \{1, 2\}$ with zero constraint $b_{13} = 0$:

$$\pi_{13} = a_{12} \cdot \pi_{23} \implies a_{12} = 3$$

Verification: $b_{11} = 1 - 3 \times 1 = -2$, $b_{12} = 2 - 3 \times 1 = -1$, $b_{13} = 0$. Thus $s_1 = 2$.

Solution 2: Support $S'_1 = \{2, 3\}$ with zero constraint $b'_{11} = 0$:

$$\pi_{11} = a'_{12} \cdot \pi_{21} \implies a'_{12} = 1$$

Verification: $b'_{11} = 0$, $b'_{12} = 2 - 1 \times 1 = 1$, $b'_{13} = 3 - 1 \times 1 = 2$. Thus $s'_1 = 2$.

Both solutions satisfy the same reduced form and sparsity level, but yield different causal effects ($a_{12} = 3 \neq 1 = a'_{12}$). The key observation is that $(S_1 \cup S'_1)^c = \emptyset$ —there are no shared zero constraints to enforce uniqueness. This demonstrates that the bound $s_j \leq (k - p + 1)/2$ is tight.

Examples of Instrument Diversity

Example 1 (Failure of Instrument Diversity: Block diagonal $\mathbf{\Pi}$). Consider $p = 2$ traits, $k = 4$ instruments, with block diagonal structure:

$$\mathbf{\Pi} = \begin{pmatrix} \pi_{11} & \pi_{12} & 0 & 0 \\ 0 & 0 & \pi_{23} & \pi_{24} \end{pmatrix}$$

Instrument Diversity fails because:

- For $j = 1$: $\mathbf{\Pi}_{-1} = (0, 0, \pi_{23}, \pi_{24})$. Any 1×1 submatrix from columns 1 or 2 is zero.
- For $j = 2$: $\mathbf{\Pi}_{-2} = (\pi_{11}, \pi_{12}, 0, 0)$. Any 1×1 submatrix from columns 3 or 4 is zero.

Instruments 1–2 affect only trait 1; instruments 3–4 affect only trait 2. There is no “cross-trait” variation to identify the causal effects a_{12} and a_{21} .

Example 2 (Failure of Instrument Diversity: Insufficient instruments for one trait). Consider $p = 2$ traits, $k = 4$ instruments:

$$\mathbf{\Pi} = \begin{pmatrix} \pi_{11} & 0 & 0 & 0 \\ 0 & \pi_{22} & \pi_{23} & \pi_{24} \end{pmatrix}$$

Instrument Diversity fails because:

- For $j = 1$: $\mathbf{\Pi}_{-1} = (0, \pi_{22}, \pi_{23}, \pi_{24})$. Column 1 is zero, so any 1×1 submatrix using column 1 fails.

- For $j = 2$: $\mathbf{\Pi}_{-2} = (\pi_{11}, 0, 0, 0)$. Columns 2, 3, 4 are zero.

Trait 1 has only one instrument (column 1), and this instrument does not affect trait 2 in the reduced form. There is no information to identify a_{12} (the causal effect of trait 2 on trait 1).

Example 3 (Instrument Diversity satisfied). Consider $p = 2$ traits, $k = 4$ instruments with dense $\mathbf{\Pi}$:

$$\mathbf{\Pi} = \begin{pmatrix} 1 & 2 & 3 & 4 \\ 5 & 6 & 7 & 8 \end{pmatrix}$$

Instrument Diversity holds because:

- For $j = 1$: $\mathbf{\Pi}_{-1} = (5, 6, 7, 8)$. All 1×1 submatrices are non-zero.
- For $j = 2$: $\mathbf{\Pi}_{-2} = (1, 2, 3, 4)$. All 1×1 submatrices are non-zero.

With the per-trait bound $s_j \leq (4 - 2 + 1)/2 = 1.5$, each trait can have at most 1 direct instrument effect.

5 Additional Simulation Results

We provide all figures for network size $p=5$ and all tables for $p \in \{5, 10\}$ under three settings: (1) scale-free network with feedback loops and unmeasured confounding; (2) small-world network with feedback loops and unmeasured confounding; and (3) small-world network with feedback loops, unmeasured confounding, and horizontal pleiotropy. The only exceptions are the graph recovery performance table and the causal effect estimation table for the scale-free setting with $p=10$, which are included in the main manuscript. Unless noted otherwise, all figures report results across $n \in \{500, 1000, 10,000, 30,000\}$. For each combination of scenario, sample size, and network size, every method is evaluated over 20 independent replicates; figures and tables summarize these replicates.

5.1 Case 1: Scale-free network with feedback loops and unmeasured confounding

Overview. Figure (1) reports graph-recovery AUC (boxplots) by method across sample sizes for network size $p = 5$. Tables (1) summarize graph-recovery metrics (AUC, TPR, FDR, MCC; mean \pm sd) for $p = 5$. Figure (2) shows causal-effect estimation error (MeanAbsDev; boxplots) by method across sample sizes for $p = 5$, while Tables (2) report effect-estimation error metrics (MaxAbsDev, MeanAbsDev, MeanSqDev; mean \pm sd) for $p = 5$. Finally, Figure (3) presents confounding-structure recovery AUC (boxplots) for $p = 5$ using MR.RGM, and Table (3) compiles confounding-structure recovery metrics (AUC, TPR, FDR, MCC; mean \pm sd) for $p \in \{5, 10\}$ using MR.RGM across all sample sizes.

5.2 Case 2: Small-world network with feedback loops and unmeasured confounding

Overview. Figure (4) reports graph-recovery AUC (boxplots) by method across sample sizes for network size $p = 5$. Tables (4) and (5) summarize graph-recovery metrics (AUC, TPR, FDR, MCC; mean \pm sd) for $p \in \{5, 10\}$. Figure (5) shows causal-effect estimation error (MeanAbsDev; boxplots) by method across sample sizes for $p = 5$, while Tables (6) and (7) report effect-estimation error metrics (MaxAbsDev, MeanAbsDev, MeanSqDev; mean \pm sd) for $p \in \{5, 10\}$. Finally, Figure

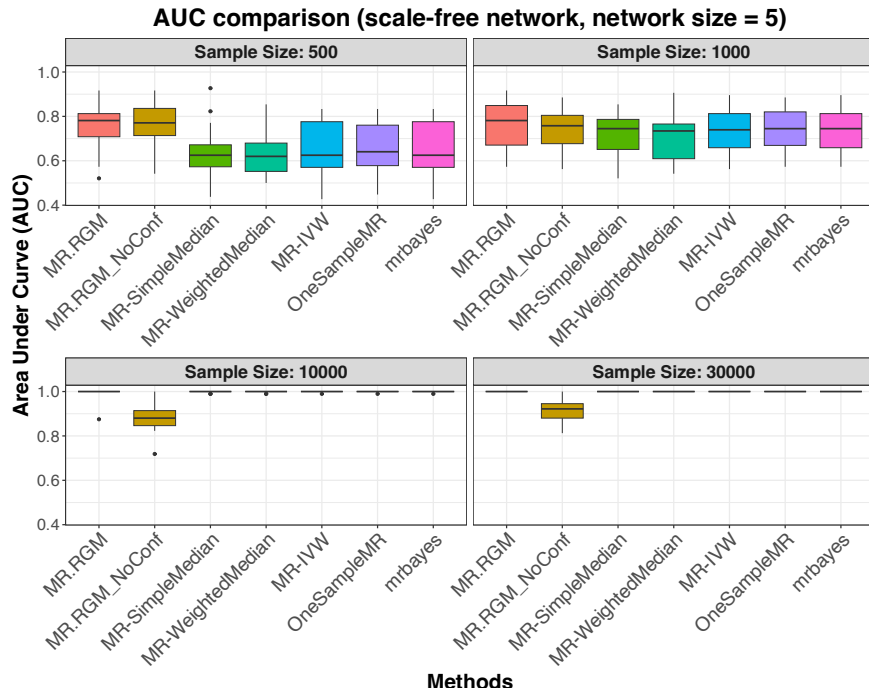


Figure 1: Graph recovery performance in a scale-free network with feedback loops and unmeasured confounding, with network size $p=5$. Boxplots of AUC by method (x-axis) and sample size (facets; $n \in \{500, 1000, 10000, 30000\}$).

(6) presents confounding-structure recovery AUC (boxplots) for $p = 5$ using MR.RGM, and Table (8) compiles confounding-structure recovery metrics (AUC, TPR, FDR, MCC; mean \pm sd) for $p \in \{5, 10\}$ using MR.RGM across all sample sizes.

5.3 Case 3: Small-world network with feedback loops, unmeasured confounding, and horizontal pleiotropy

Overview. Figure (7) reports graph-recovery AUC (boxplots) by method across sample sizes for network size $p = 5$. Tables (9) and (10) summarize graph-recovery metrics (AUC, TPR, FDR, MCC; mean \pm sd) for $p \in \{5, 10\}$. Figure (8) shows causal-effect estimation error (MeanAbsDev; boxplots) by method across sample sizes for $p = 5$, while Tables (11) and (12) report effect-estimation error metrics (MaxAbsDev, MeanAbsDev, MeanSqDev; mean \pm sd) for $p \in \{5, 10\}$. Figure (9) presents confounding-structure recovery AUC (boxplots) across sample sizes for both MR.RGM and MR.RGM+ at $p = 5$, and Tables (13) and (14) compile confounding-structure recovery metrics (AUC, TPR, FDR, MCC; mean \pm sd) for MR.RGM and MR.RGM+ respectively at $p \in \{5, 10\}$. Finally, Figure (10) displays instrument-trait selection AUC (boxplots) for MR.RGM+ across sample sizes at $p = 5$.

Table 1: Graph recovery performance in a scale-free network with feedback loops and unmeasured confounding, with network size $p=5$.

Setting	Method	AUC	TPR	FDR	MCC
n = 500	MR.RGM	0.754 (0.097)	0.500 (0.125)	0.298 (0.179)	0.381 (0.208)
	MR.RGM_NoConf	0.756 (0.097)	0.556 (0.092)	0.338 (0.157)	0.361 (0.164)
	MR-SimpleMedian	0.641 (0.117)	0.056 (0.075)	0.231 (0.389)	0.055 (0.174)
	MR-WeightedMedian	0.630 (0.098)	0.069 (0.095)	0.287 (0.388)	0.045 (0.180)
	MR-IVW	0.653 (0.122)	0.174 (0.119)	0.213 (0.247)	0.203 (0.193)
	OneSampleMR	0.661 (0.108)	0.174 (0.119)	0.199 (0.238)	0.207 (0.180)
	mrbytes	0.654 (0.121)	0.174 (0.119)	0.222 (0.261)	0.197 (0.200)
n = 1000	MR.RGM	0.771 (0.111)	0.549 (0.187)	0.235 (0.141)	0.468 (0.182)
	MR.RGM_NoConf	0.749 (0.101)	0.605 (0.173)	0.308 (0.158)	0.426 (0.213)
	MR-SimpleMedian	0.721 (0.099)	0.132 (0.088)	0.194 (0.231)	0.160 (0.135)
	MR-WeightedMedian	0.703 (0.099)	0.174 (0.133)	0.349 (0.359)	0.160 (0.208)
	MR-IVW	0.742 (0.093)	0.278 (0.142)	0.299 (0.274)	0.260 (0.206)
	OneSampleMR	0.744 (0.090)	0.264 (0.155)	0.298 (0.281)	0.243 (0.224)
	mrbytes	0.742 (0.093)	0.264 (0.155)	0.307 (0.285)	0.236 (0.226)
n = 10000	MR.RGM	0.993 (0.029)	0.965 (0.056)	0.000 (0.000)	0.972 (0.045)
	MR.RGM_NoConf	0.884 (0.066)	0.831 (0.154)	0.336 (0.078)	0.538 (0.105)
	MR-SimpleMedian	0.999 (0.003)	0.972 (0.052)	0.044 (0.055)	0.939 (0.060)
	MR-WeightedMedian	0.999 (0.003)	0.972 (0.052)	0.044 (0.055)	0.939 (0.060)
	MR-IVW	0.999 (0.002)	0.993 (0.029)	0.037 (0.052)	0.962 (0.048)
	OneSampleMR	0.999 (0.002)	0.993 (0.029)	0.043 (0.054)	0.957 (0.049)
	mrbytes	1.000 (0.001)	0.993 (0.029)	0.037 (0.052)	0.962 (0.048)
n = 30000	MR.RGM	1.000 (0.000)	1.000 (0.000)	0.000 (0.000)	1.000 (0.000)
	MR.RGM_NoConf	0.910 (0.051)	0.888 (0.142)	0.273 (0.124)	0.640 (0.095)
	MR-SimpleMedian	1.000 (0.000)	1.000 (0.000)	0.087 (0.081)	0.922 (0.075)
	MR-WeightedMedian	1.000 (0.000)	1.000 (0.000)	0.087 (0.081)	0.922 (0.075)
	MR-IVW	1.000 (0.000)	1.000 (0.000)	0.111 (0.097)	0.898 (0.092)
	OneSampleMR	1.000 (0.000)	1.000 (0.000)	0.111 (0.097)	0.898 (0.092)
	mrbytes	1.000 (0.000)	1.000 (0.000)	0.111 (0.097)	0.898 (0.092)

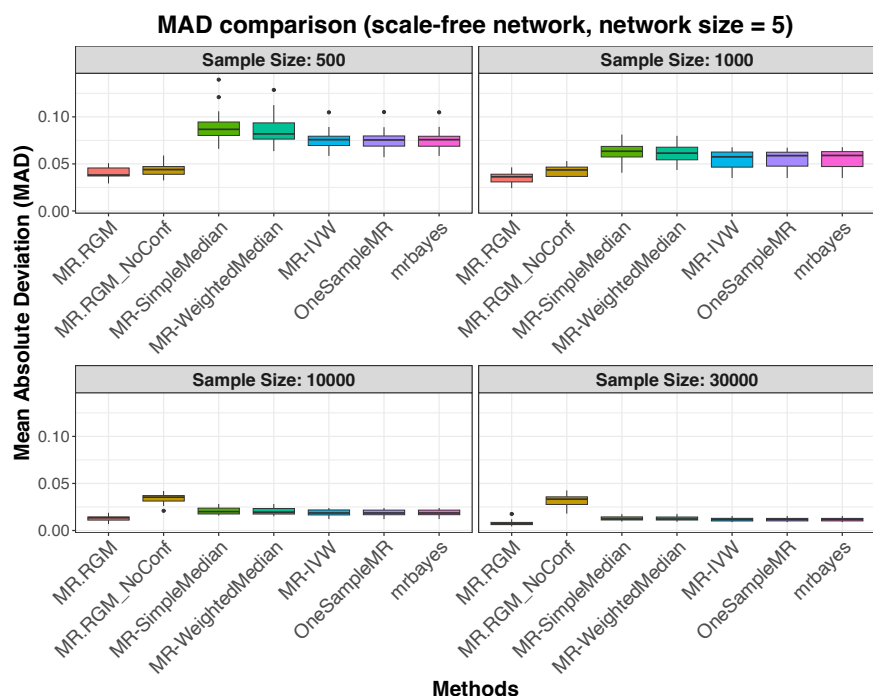


Figure 2: Causal effect estimation performance in a scale-free network with feedback loops and unmeasured confounding, with network size $p = 5$. Boxplots of mean absolute deviation (MAD) by method (x-axis) and sample size (facets; $n \in \{500, 1000, 10000, 30000\}$).

Table 2: Causal effect estimation performance in a scale-free network with feedback loops and unmeasured confounding, with network size $p = 5$.

Setting	Method	MaxAbsDev	MeanAbsDev	MeanSqDev
n = 500	MR.RGM	0.119 (0.018)	0.040 (0.006)	0.003 (0.001)
	MR.RGM.NoConf	0.130 (0.021)	0.045 (0.007)	0.003 (0.001)
	MR-SimpleMedian	0.253 (0.052)	0.090 (0.017)	0.013 (0.004)
	MR-WeightedMedian	0.242 (0.051)	0.086 (0.016)	0.012 (0.004)
	MR-IVW	0.210 (0.053)	0.076 (0.010)	0.009 (0.002)
	OneSampleMR	0.209 (0.054)	0.075 (0.010)	0.009 (0.002)
n = 1000	MR.RGM	0.101 (0.015)	0.036 (0.006)	0.002 (0.001)
	MR.RGM.NoConf	0.118 (0.020)	0.042 (0.006)	0.003 (0.001)
	MR-SimpleMedian	0.175 (0.037)	0.062 (0.010)	0.006 (0.002)
	MR-WeightedMedian	0.174 (0.036)	0.061 (0.010)	0.006 (0.002)
	MR-IVW	0.164 (0.035)	0.055 (0.010)	0.005 (0.001)
	OneSampleMR	0.165 (0.035)	0.055 (0.009)	0.005 (0.001)
n = 10000	MR.RGM	0.046 (0.019)	0.013 (0.003)	0.0003 (0.0002)
	MR.RGM.NoConf	0.087 (0.013)	0.034 (0.005)	0.002 (0.0004)
	MR-SimpleMedian	0.059 (0.014)	0.021 (0.004)	0.001 (0.000)
	MR-WeightedMedian	0.058 (0.014)	0.021 (0.004)	0.001 (0.000)
	MR-IVW	0.049 (0.010)	0.019 (0.003)	0.001 (0.000)
	OneSampleMR	0.049 (0.010)	0.019 (0.003)	0.001 (0.000)
n = 30000	MR.RGM	0.030 (0.025)	0.008 (0.003)	0.0002 (0.0003)
	MR.RGM.NoConf	0.081 (0.012)	0.032 (0.006)	0.002 (0.0004)
	MR-SimpleMedian	0.035 (0.009)	0.013 (0.002)	0.0003 (0.0001)
	MR-WeightedMedian	0.035 (0.009)	0.013 (0.002)	0.0003 (0.0001)
	MR-IVW	0.031 (0.005)	0.012 (0.002)	0.0002 (0.0001)
	OneSampleMR	0.031 (0.005)	0.012 (0.002)	0.0002 (0.0001)
n = 30000	MR.RGM	0.031 (0.005)	0.012 (0.002)	0.0002 (0.0001)
	MR.RGM.NoConf	0.031 (0.005)	0.012 (0.002)	0.0002 (0.0001)
	MR-SimpleMedian	0.031 (0.005)	0.012 (0.002)	0.0002 (0.0001)
	MR-WeightedMedian	0.031 (0.005)	0.012 (0.002)	0.0002 (0.0001)
	MR-IVW	0.031 (0.005)	0.012 (0.002)	0.0002 (0.0001)
	OneSampleMR	0.031 (0.005)	0.012 (0.002)	0.0002 (0.0001)

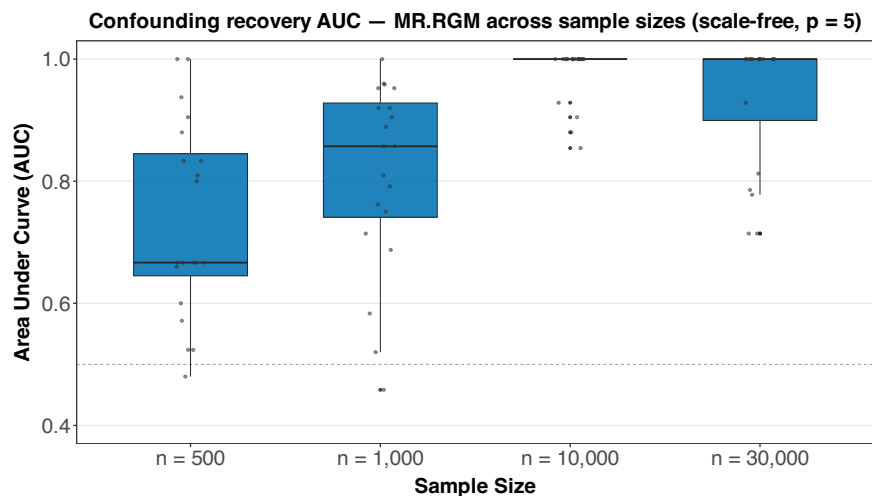


Figure 3: Confounding structure recovery performance using MR.RGM in a scale-free network with feedback loops and unmeasured confounding, with network size $p = 5$. Boxplots of AUC across sample sizes ($n \in \{500, 1000, 10000, 30000\}$).

Table 3: Confounding structure recovery performance using MR.RGM in a scale-free network with feedback loops and unmeasured confounding, across network sizes $p \in \{5, 10\}$.

Setting	Sample Size	AUC	TPR	FDR	MCC
p = 5	500	0.735 (0.156)	0.307 (0.193)	0.242 (0.296)	0.219 (0.264)
	1000	0.812 (0.151)	0.464 (0.214)	0.255 (0.340)	0.332 (0.342)
	10000	0.978 (0.045)	0.952 (0.076)	0.185 (0.283)	0.728 (0.308)
	30000	0.937 (0.105)	1.000 (0.000)	0.203 (0.280)	0.709 (0.378)
p = 10	500	0.709 (0.081)	0.242 (0.070)	0.150 (0.115)	0.210 (0.114)
	1000	0.804 (0.085)	0.335 (0.076)	0.110 (0.086)	0.290 (0.148)
	10000	0.984 (0.018)	0.886 (0.064)	0.016 (0.027)	0.839 (0.091)
	30000	0.996 (0.011)	0.995 (0.013)	0.007 (0.013)	0.982 (0.029)

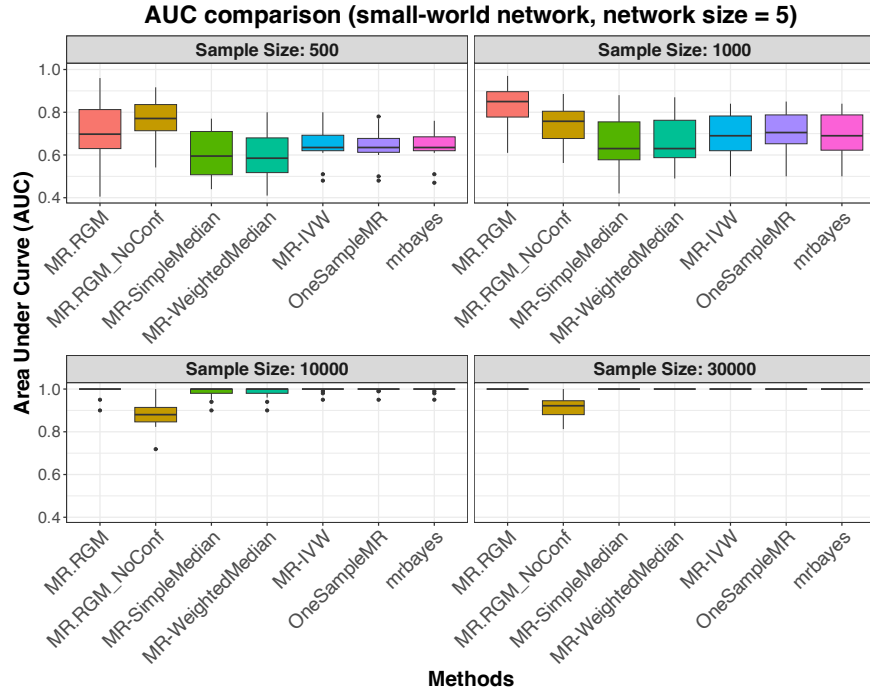


Figure 4: Graph recovery performance in a small-world network with feedback loops and unmeasured confounding, with network size $p=5$. Boxplots of AUC by method (x-axis) and sample size (facets; $n \in \{500, 1000, 10000, 30000\}$).

Table 4: Graph recovery performance in a small-world network with feedback loops and unmeasured confounding, with network size $p=5$.

Setting	Method	AUC	TPR	FDR	MCC
n = 500	MR.RGM	0.712 (0.142)	0.467 (0.183)	0.282 (0.165)	0.309 (0.219)
	MR.RGM_NoConf	0.763 (0.100)	0.569 (0.086)	0.352 (0.143)	0.358 (0.168)
	MR-SimpleMedian	0.607 (0.112)	0.100 (0.089)	0.179 (0.319)	0.121 (0.174)
	MR-WeightedMedian	0.606 (0.111)	0.135 (0.101)	0.192 (0.326)	0.161 (0.221)
	MR-IVW	0.652 (0.075)	0.195 (0.107)	0.221 (0.315)	0.214 (0.198)
	OneSampleMR	0.647 (0.078)	0.200 (0.120)	0.213 (0.331)	0.224 (0.217)
	mrbayes	0.646 (0.071)	0.189 (0.110)	0.213 (0.331)	0.216 (0.208)
n = 1000	MR.RGM	0.832 (0.087)	0.561 (0.146)	0.130 (0.105)	0.513 (0.167)
	MR.RGM_NoConf	0.738 (0.099)	0.594 (0.168)	0.315 (0.165)	0.411 (0.220)
	MR-SimpleMedian	0.656 (0.121)	0.160 (0.086)	0.025 (0.109)	0.260 (0.126)
	MR-WeightedMedian	0.668 (0.118)	0.160 (0.097)	0.067 (0.162)	0.238 (0.144)
	MR-IVW	0.699 (0.099)	0.295 (0.156)	0.128 (0.171)	0.314 (0.175)
	OneSampleMR	0.712 (0.097)	0.322 (0.155)	0.091 (0.142)	0.363 (0.155)
	mrbayes	0.702 (0.098)	0.317 (0.154)	0.142 (0.174)	0.323 (0.185)
n = 10000	MR.RGM	0.992 (0.025)	0.950 (0.060)	0.006 (0.025)	0.946 (0.075)
	MR.RGM_NoConf	0.887 (0.069)	0.833 (0.161)	0.331 (0.081)	0.546 (0.106)
	MR-SimpleMedian	0.984 (0.026)	0.925 (0.062)	0.041 (0.071)	0.885 (0.101)
	MR-WeightedMedian	0.985 (0.025)	0.935 (0.065)	0.041 (0.071)	0.894 (0.106)
	MR-IVW	0.996 (0.012)	0.990 (0.030)	0.075 (0.083)	0.908 (0.098)
	OneSampleMR	0.996 (0.012)	0.989 (0.031)	0.070 (0.077)	0.912 (0.092)
	mrbayes	0.996 (0.012)	0.989 (0.031)	0.065 (0.079)	0.917 (0.094)
n = 30000	MR.RGM	1.000 (0.000)	1.000 (0.000)	0.000 (0.000)	1.000 (0.000)
	MR.RGM_NoConf	0.913 (0.053)	0.882 (0.147)	0.265 (0.126)	0.645 (0.088)
	MR-SimpleMedian	1.000 (0.000)	1.000 (0.000)	0.058 (0.056)	0.939 (0.061)
	MR-WeightedMedian	1.000 (0.000)	1.000 (0.000)	0.058 (0.056)	0.939 (0.061)
	MR-IVW	1.000 (0.000)	1.000 (0.000)	0.091 (0.062)	0.902 (0.068)
	OneSampleMR	1.000 (0.000)	1.000 (0.000)	0.087 (0.062)	0.907 (0.068)
	mrbayes	1.000 (0.000)	1.000 (0.000)	0.087 (0.062)	0.907 (0.068)

Table 5: Graph recovery performance in a small-world network with feedback loops and unmeasured confounding, with network size $p=10$.

Setting	Method	AUC	TPR	FDR	MCC
n = 500	MR.RGM	0.737 (0.069)	0.500 (0.100)	0.494 (0.083)	0.360 (0.100)
	MR.RGM_NoConf	0.796 (0.069)	0.594 (0.107)	0.544 (0.091)	0.378 (0.122)
	MR-SimpleMedian	0.593 (0.081)	0.065 (0.050)	0.490 (0.360)	0.095 (0.121)
	MR-WeightedMedian	0.602 (0.083)	0.093 (0.062)	0.540 (0.297)	0.111 (0.136)
	MR-IVW	0.651 (0.066)	0.175 (0.068)	0.479 (0.200)	0.196 (0.113)
	OneSampleMR	0.654 (0.070)	0.186 (0.072)	0.478 (0.199)	0.202 (0.116)
	mrbytes	0.650 (0.069)	0.175 (0.071)	0.484 (0.195)	0.194 (0.111)
n = 1000	MR.RGM	0.813 (0.052)	0.594 (0.109)	0.379 (0.078)	0.498 (0.100)
	MR.RGM_NoConf	0.796 (0.069)	0.594 (0.107)	0.544 (0.091)	0.378 (0.122)
	MR-SimpleMedian	0.698 (0.093)	0.218 (0.088)	0.331 (0.191)	0.293 (0.125)
	MR-WeightedMedian	0.712 (0.090)	0.240 (0.083)	0.345 (0.132)	0.303 (0.096)
	MR-IVW	0.761 (0.061)	0.360 (0.116)	0.316 (0.091)	0.398 (0.088)
	OneSampleMR	0.758 (0.063)	0.375 (0.110)	0.312 (0.075)	0.411 (0.081)
	mrbytes	0.756 (0.062)	0.367 (0.120)	0.321 (0.085)	0.400 (0.090)
n = 10000	MR.RGM	0.994 (0.016)	0.972 (0.042)	0.032 (0.031)	0.961 (0.031)
	MR.RGM_NoConf	0.919 (0.029)	0.905 (0.077)	0.491 (0.059)	0.572 (0.070)
	MR-SimpleMedian	0.994 (0.007)	0.955 (0.061)	0.128 (0.064)	0.885 (0.066)
	MR-WeightedMedian	0.994 (0.007)	0.963 (0.061)	0.135 (0.062)	0.885 (0.062)
	MR-IVW	0.998 (0.003)	0.993 (0.024)	0.156 (0.075)	0.888 (0.060)
	OneSampleMR	0.998 (0.003)	0.992 (0.025)	0.156 (0.082)	0.887 (0.065)
	mrbytes	0.998 (0.003)	0.992 (0.025)	0.156 (0.082)	0.887 (0.065)
n = 30000	MR.RGM	1.000 (0.002)	0.994 (0.016)	0.000 (0.000)	1.000 (0.010)
	MR.RGM_NoConf	0.941 (0.032)	0.921 (0.054)	0.455 (0.053)	0.615 (0.059)
	MR-SimpleMedian	1.000 (0.000)	1.000 (0.000)	0.146 (0.052)	0.901 (0.036)
	MR-WeightedMedian	1.000 (0.000)	1.000 (0.000)	0.148 (0.049)	0.899 (0.035)
	MR-IVW	1.000 (0.000)	1.000 (0.000)	0.183 (0.058)	0.873 (0.042)
	OneSampleMR	1.000 (0.000)	1.000 (0.000)	0.188 (0.066)	0.870 (0.048)
	mrbytes	1.000 (0.000)	1.000 (0.000)	0.190 (0.061)	0.868 (0.045)

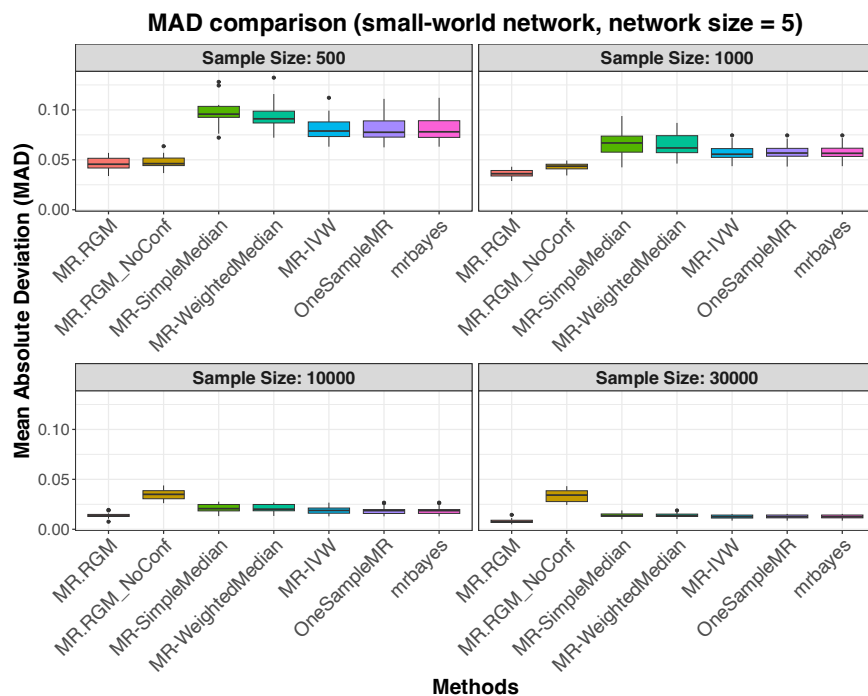


Figure 5: Causal effect estimation performance in a small-world network with feedback loops and unmeasured confounding, with network size $p=5$. Boxplots of mean absolute deviation (MAD) by method (x-axis) and sample size (facets; $n \in \{500, 1000, 10000, 30000\}$).

Table 6: Causal effect estimation performance in a small-world network with feedback loops and unmeasured confounding, with network size $p=5$.

Setting	Method	MaxAbsDev	MeanAbsDev	MeanSqDev
n = 500	MR.RGM	0.127 (0.022)	0.045 (0.007)	0.003 (0.001)
	MR.RGM_NoConf	0.140 (0.033)	0.048 (0.006)	0.004 (0.001)
	MR-SimpleMedian	0.259 (0.048)	0.097 (0.013)	0.015 (0.004)
	MR-WeightedMedian	0.253 (0.041)	0.094 (0.013)	0.014 (0.003)
	MR-IVW	0.222 (0.042)	0.081 (0.012)	0.010 (0.003)
	OneSampleMR	0.216 (0.041)	0.081 (0.012)	0.010 (0.003)
n = 1000	MR.RGM	0.106 (0.022)	0.036 (0.004)	0.002 (0.0004)
	MR.RGM_NoConf	0.134 (0.024)	0.043 (0.004)	0.003 (0.001)
	MR-SimpleMedian	0.167 (0.031)	0.067 (0.013)	0.007 (0.002)
	MR-WeightedMedian	0.160 (0.019)	0.065 (0.011)	0.006 (0.002)
	MR-IVW	0.144 (0.030)	0.057 (0.008)	0.005 (0.001)
	OneSampleMR	0.148 (0.027)	0.058 (0.008)	0.005 (0.001)
n = 10000	MR.RGM	0.045 (0.010)	0.014 (0.003)	0.0003 (0.0001)
	MR.RGM_NoConf	0.095 (0.016)	0.035 (0.005)	0.002 (0.0005)
	MR-SimpleMedian	0.057 (0.012)	0.021 (0.004)	0.001 (0.0003)
	MR-WeightedMedian	0.057 (0.012)	0.021 (0.004)	0.001 (0.0003)
	MR-IVW	0.051 (0.010)	0.019 (0.004)	0.001 (0.0002)
	OneSampleMR	0.050 (0.009)	0.019 (0.004)	0.001 (0.0002)
n = 30000	MR.RGM	0.033 (0.029)	0.008 (0.002)	0.0002 (0.0002)
	MR.RGM_NoConf	0.089 (0.018)	0.033 (0.006)	0.002 (0.0004)
	MR-SimpleMedian	0.038 (0.010)	0.014 (0.002)	0.0003 (0.0001)
	MR-WeightedMedian	0.038 (0.009)	0.014 (0.002)	0.0003 (0.0001)
	MR-IVW	0.037 (0.008)	0.013 (0.002)	0.0003 (0.0001)
	OneSampleMR	0.036 (0.008)	0.013 (0.002)	0.0003 (0.0001)
n = 30000	MR.RGM	0.033 (0.029)	0.008 (0.002)	0.0002 (0.0002)
	MR.RGM_NoConf	0.089 (0.018)	0.033 (0.006)	0.002 (0.0004)
	MR-SimpleMedian	0.038 (0.010)	0.014 (0.002)	0.0003 (0.0001)
	MR-WeightedMedian	0.038 (0.009)	0.014 (0.002)	0.0003 (0.0001)
	MR-IVW	0.037 (0.008)	0.013 (0.002)	0.0003 (0.0001)
	OneSampleMR	0.036 (0.008)	0.013 (0.002)	0.0003 (0.0001)

Table 7: Causal effect estimation performance in a small-world network with feedback loops and unmeasured confounding, with network size $p=10$.

Setting	Method	MaxAbsDev	MeanAbsDev	MeanSqDev
n = 500	MR.RGM	0.153 (0.034)	0.036 (0.004)	0.002 (0.001)
	MR.RGM_NoConf	0.175 (0.034)	0.040 (0.004)	0.003 (0.001)
	MR-SimpleMedian	0.336 (0.076)	0.094 (0.011)	0.014 (0.003)
	MR-WeightedMedian	0.325 (0.058)	0.089 (0.012)	0.013 (0.003)
	MR-IVW	0.299 (0.064)	0.081 (0.010)	0.011 (0.003)
	OneSampleMR	0.302 (0.066)	0.082 (0.009)	0.011 (0.002)
n = 1000	MR.RGM	0.031 (0.018)	0.006 (0.001)	0.0001 (0.00002)
	MR.RGM_NoConf	0.151 (0.026)	0.035 (0.002)	0.002 (0.0003)
	MR-SimpleMedian	0.229 (0.034)	0.066 (0.005)	0.007 (0.001)
	MR-WeightedMedian	0.215 (0.025)	0.063 (0.006)	0.006 (0.001)
	MR-IVW	0.194 (0.023)	0.057 (0.006)	0.005 (0.001)
	OneSampleMR	0.196 (0.022)	0.058 (0.006)	0.005 (0.001)
n = 10000	MR.RGM	0.054 (0.007)	0.012 (0.001)	0.0003 (0.0001)
	MR.RGM_NoConf	0.105 (0.018)	0.029 (0.003)	0.002 (0.0002)
	MR-SimpleMedian	0.072 (0.008)	0.022 (0.001)	0.0007 (0.0001)
	MR-WeightedMedian	0.072 (0.008)	0.021 (0.001)	0.0007 (0.0001)
	MR-IVW	0.062 (0.008)	0.019 (0.001)	0.0005 (0.0001)
	OneSampleMR	0.062 (0.008)	0.018 (0.001)	0.0005 (0.0001)
n = 30000	MR.RGM	0.030 (0.018)	0.006 (0.001)	0.0001 (0.00002)
	MR.RGM_NoConf	0.096 (0.013)	0.028 (0.003)	0.001 (0.0001)
	MR-SimpleMedian	0.046 (0.007)	0.012 (0.001)	0.0003 (0.00004)
	MR-WeightedMedian	0.045 (0.007)	0.012 (0.001)	0.0002 (0.00004)
	MR-IVW	0.039 (0.007)	0.011 (0.001)	0.0002 (0.00003)
	OneSampleMR	0.038 (0.005)	0.011 (0.001)	0.0002 (0.00003)
n = 30000	MR.RGM	0.030 (0.018)	0.006 (0.001)	0.0001 (0.00002)
	MR.RGM_NoConf	0.096 (0.013)	0.028 (0.003)	0.001 (0.0001)
	MR-SimpleMedian	0.046 (0.007)	0.012 (0.001)	0.0003 (0.00004)
	MR-WeightedMedian	0.045 (0.007)	0.012 (0.001)	0.0002 (0.00004)
	MR-IVW	0.039 (0.007)	0.011 (0.001)	0.0002 (0.00003)
	OneSampleMR	0.038 (0.005)	0.011 (0.001)	0.0002 (0.00003)

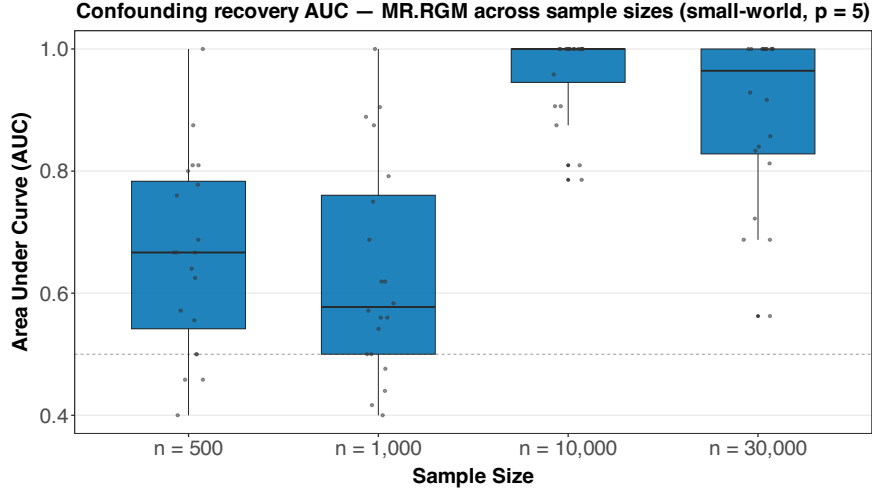


Figure 6: Confounding structure recovery performance using MR.RGM in a small-world network with feedback loops and unmeasured confounding, with network size $p=5$. Boxplots of AUC across sample sizes ($n \in \{500, 1000, 10000, 30000\}$).

Table 8: Confounding structure recovery performance using MR.RGM in a small-world network with feedback loops and unmeasured confounding, across network sizes $p \in \{5, 10\}$.

Setting	Sample Size	AUC	TPR	FDR	MCC
$p = 5$	500	0.661 (0.154)	0.312 (0.290)	0.363 (0.384)	0.179 (0.369)
	1000	0.634 (0.173)	0.480 (0.307)	0.418 (0.300)	0.216 (0.327)
	10000	0.962 (0.066)	0.905 (0.148)	0.321 (0.351)	0.584 (0.290)
	30000	0.892 (0.133)	0.990 (0.044)	0.333 (0.354)	0.651 (0.348)
$p = 10$	500	0.687 (0.067)	0.288 (0.083)	0.262 (0.226)	0.213 (0.135)
	1000	0.756 (0.067)	0.402 (0.121)	0.180 (0.191)	0.349 (0.127)
	10000	0.983 (0.017)	0.926 (0.068)	0.152 (0.270)	0.762 (0.219)
	30000	0.950 (0.102)	0.998 (0.008)	0.151 (0.289)	0.847 (0.286)

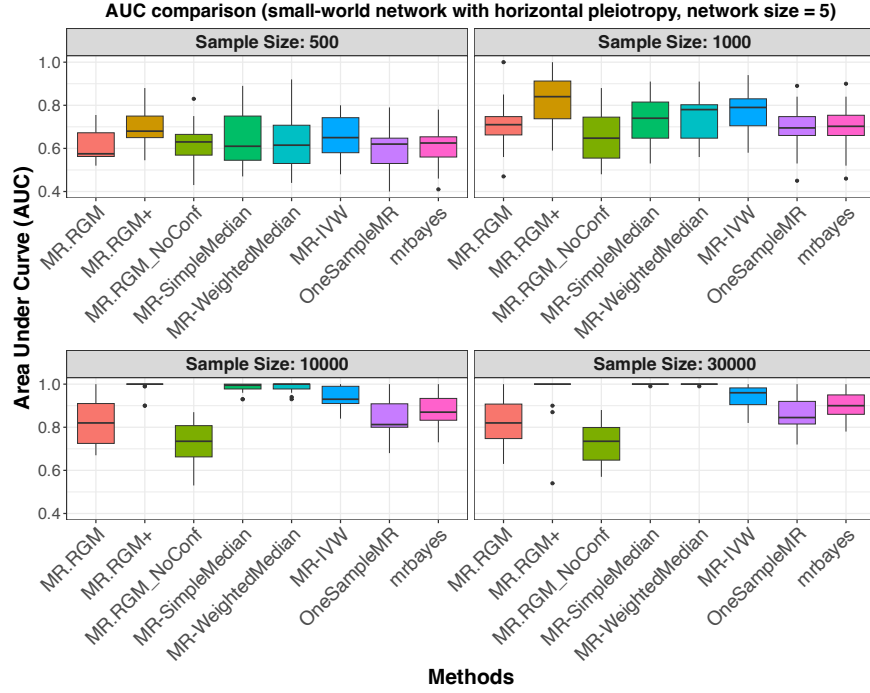


Figure 7: Graph recovery performance in a small-world network with feedback loops, unmeasured confounding, and horizontal pleiotropy, with network size $p=5$. Boxplots of AUC by method (x -axis) and sample size (facets; $n \in \{500, 1000, 10000, 30000\}$).

Table 9: Graph recovery performance in a small-world network with feedback loops, unmeasured confounding, and horizontal pleiotropy, with network size $p=5$.

Setting	Method	AUC	TPR	FDR	MCC
n = 500	MR.RGM	0.614 (0.072)	0.483 (0.126)	0.374 (0.134)	0.192 (0.212)
	MR.RGM+	0.697 (0.083)	0.483 (0.146)	0.256 (0.093)	0.344 (0.160)
	MR.RGM_NoConf	0.621 (0.095)	0.536 (0.123)	0.392 (0.103)	0.177 (0.181)
	MR-SimpleMedian	0.642 (0.120)	0.080 (0.081)	0.067 (0.226)	0.131 (0.156)
	MR-WeightedMedian	0.629 (0.123)	0.105 (0.074)	0.117 (0.211)	0.142 (0.144)
	MR-IVW	0.650 (0.094)	0.180 (0.087)	0.163 (0.239)	0.214 (0.179)
	OneSampleMR	0.595 (0.106)	0.244 (0.112)	0.410 (0.230)	0.103 (0.215)
	mrbayes	0.606 (0.094)	0.244 (0.096)	0.422 (0.165)	0.085 (0.171)
n = 1000	MR.RGM	0.714 (0.113)	0.594 (0.122)	0.286 (0.123)	0.358 (0.196)
	MR.RGM+	0.817 (0.114)	0.528 (0.182)	0.135 (0.140)	0.481 (0.200)
	MR.RGM_NoConf	0.661 (0.117)	0.663 (0.154)	0.341 (0.099)	0.319 (0.203)
	MR-SimpleMedian	0.738 (0.110)	0.200 (0.138)	0.070 (0.156)	0.267 (0.159)
	MR-WeightedMedian	0.745 (0.109)	0.235 (0.128)	0.090 (0.158)	0.293 (0.139)
	MR-IVW	0.764 (0.097)	0.275 (0.148)	0.130 (0.231)	0.312 (0.157)
	OneSampleMR	0.690 (0.102)	0.394 (0.108)	0.325 (0.099)	0.222 (0.124)
	mrbayes	0.690 (0.105)	0.411 (0.124)	0.323 (0.092)	0.232 (0.124)
n = 10000	MR.RGM	0.826 (0.099)	0.939 (0.068)	0.173 (0.078)	0.746 (0.123)
	MR.RGM+	0.988 (0.031)	0.928 (0.087)	0.006 (0.023)	0.927 (0.084)
	MR.RGM_NoConf	0.730 (0.094)	0.828 (0.115)	0.336 (0.076)	0.420 (0.189)
	MR-SimpleMedian	0.985 (0.022)	0.935 (0.073)	0.064 (0.080)	0.869 (0.129)
	MR-WeightedMedian	0.986 (0.021)	0.955 (0.067)	0.063 (0.068)	0.889 (0.103)
	MR-IVW	0.943 (0.046)	0.825 (0.099)	0.069 (0.075)	0.770 (0.127)
	OneSampleMR	0.831 (0.090)	0.983 (0.037)	0.191 (0.078)	0.764 (0.098)
	mrbayes	0.867 (0.071)	0.978 (0.042)	0.193 (0.072)	0.757 (0.093)
n = 30000	MR.RGM	0.823 (0.097)	0.983 (0.037)	0.152 (0.075)	0.814 (0.113)
	MR.RGM+	0.962 (0.109)	0.989 (0.031)	0.042 (0.080)	0.942 (0.115)
	MR.RGM_NoConf	0.729 (0.091)	0.867 (0.094)	0.332 (0.066)	0.458 (0.169)
	MR-SimpleMedian	0.999 (0.002)	1.000 (0.000)	0.062 (0.055)	0.934 (0.060)
	MR-WeightedMedian	0.999 (0.002)	1.000 (0.000)	0.066 (0.060)	0.930 (0.065)
	MR-IVW	0.943 (0.052)	0.840 (0.102)	0.097 (0.087)	0.752 (0.148)
	OneSampleMR	0.856 (0.081)	1.000 (0.000)	0.245 (0.079)	0.705 (0.114)
	mrbayes	0.906 (0.054)	1.000 (0.000)	0.247 (0.081)	0.701 (0.117)

Table 10: Graph recovery performance in a small-world network with feedback loops, unmeasured confounding, and horizontal pleiotropy, with network size $p=10$.

Setting	Method	AUC	TPR	FDR	MCC
n = 500	MR.RGM	0.720 (0.067)	0.511 (0.101)	0.553 (0.065)	0.315 (0.090)
	MR.RGM+	0.744 (0.067)	0.514 (0.085)	0.525 (0.047)	0.342 (0.066)
	MR.RGM_NoConf	0.722 (0.075)	0.563 (0.104)	0.604 (0.061)	0.283 (0.095)
	MR-SimpleMedian	0.606 (0.067)	0.095 (0.059)	0.408 (0.293)	0.144 (0.105)
	MR-WeightedMedian	0.613 (0.072)	0.115 (0.059)	0.480 (0.256)	0.157 (0.110)
	MR-IVW	0.626 (0.087)	0.150 (0.082)	0.516 (0.240)	0.174 (0.148)
	OneSampleMR	0.627 (0.077)	0.211 (0.081)	0.575 (0.116)	0.171 (0.100)
	mrbayes	0.627 (0.078)	0.211 (0.070)	0.583 (0.116)	0.164 (0.093)
n = 1000	MR.RGM	0.797 (0.052)	0.603 (0.127)	0.449 (0.122)	0.444 (0.140)
	MR.RGM+	0.811 (0.062)	0.567 (0.122)	0.411 (0.099)	0.458 (0.112)
	MR.RGM_NoConf	0.762 (0.043)	0.686 (0.095)	0.556 (0.029)	0.387 (0.060)
	MR-SimpleMedian	0.706 (0.071)	0.200 (0.094)	0.368 (0.228)	0.264 (0.140)
	MR-WeightedMedian	0.694 (0.094)	0.220 (0.094)	0.327 (0.200)	0.294 (0.120)
	MR-IVW	0.734 (0.062)	0.275 (0.097)	0.352 (0.161)	0.326 (0.122)
	OneSampleMR	0.736 (0.061)	0.375 (0.124)	0.448 (0.150)	0.333 (0.151)
	mrbayes	0.736 (0.062)	0.383 (0.113)	0.453 (0.137)	0.333 (0.139)
n = 10000	MR.RGM	0.951 (0.029)	0.969 (0.041)	0.161 (0.067)	0.871 (0.060)
	MR.RGM+	0.985 (0.027)	0.958 (0.034)	0.061 (0.088)	0.932 (0.067)
	MR.RGM_NoConf	0.855 (0.027)	0.850 (0.061)	0.506 (0.054)	0.512 (0.070)
	MR-SimpleMedian	0.992 (0.013)	0.970 (0.058)	0.145 (0.053)	0.883 (0.056)
	MR-WeightedMedian	0.993 (0.010)	0.975 (0.056)	0.147 (0.054)	0.884 (0.055)
	MR-IVW	0.958 (0.032)	0.875 (0.086)	0.167 (0.072)	0.810 (0.084)
	OneSampleMR	0.956 (0.020)	0.994 (0.016)	0.283 (0.065)	0.793 (0.051)
	mrbayes	0.968 (0.014)	0.994 (0.016)	0.276 (0.062)	0.798 (0.049)
n = 30000	MR.RGM	0.950 (0.026)	0.992 (0.019)	0.139 (0.068)	0.900 (0.050)
	MR.RGM+	0.987 (0.023)	0.989 (0.021)	0.029 (0.075)	0.973 (0.061)
	MR.RGM_NoConf	0.869 (0.025)	0.895 (0.042)	0.530 (0.029)	0.510 (0.039)
	MR-SimpleMedian	0.999 (0.0003)	1.000 (0.000)	0.170 (0.065)	0.883 (0.048)
	MR-WeightedMedian	0.999 (0.0003)	1.000 (0.000)	0.172 (0.066)	0.882 (0.049)
	MR-IVW	0.960 (0.032)	0.893 (0.071)	0.196 (0.058)	0.800 (0.057)
	OneSampleMR	0.966 (0.016)	1.000 (0.000)	0.336 (0.066)	0.752 (0.055)
	mrbayes	0.977 (0.010)	1.000 (0.000)	0.335 (0.065)	0.753 (0.054)

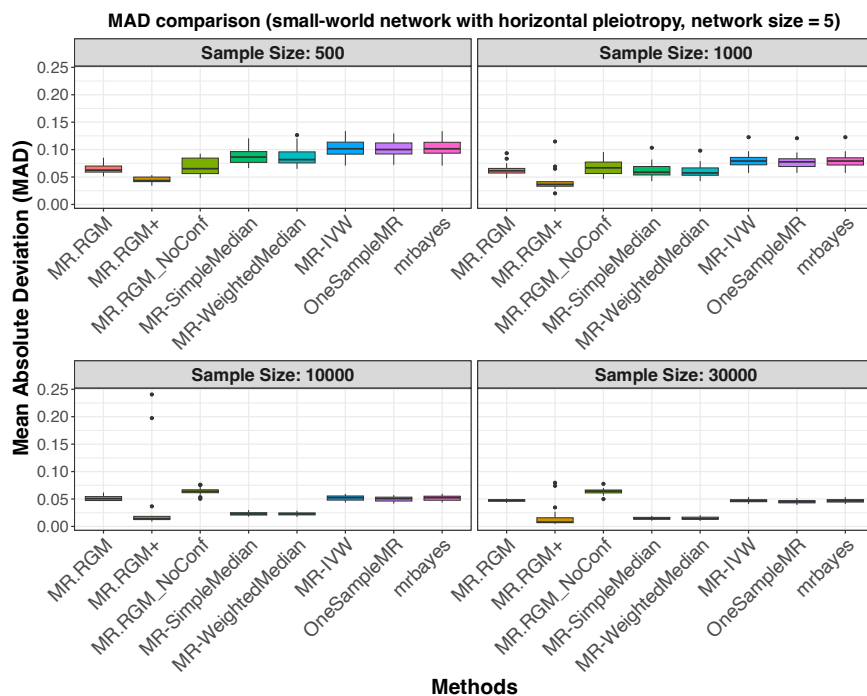


Figure 8: Causal effect estimation performance in a small-world network with feedback loops, unmeasured confounding, and horizontal pleiotropy, with network size $p=5$. Boxplots of mean absolute deviation (MAD) by method (x-axis) and sample size (facets; $n \in \{500, 1000, 10000, 30000\}$).

Table 11: Causal effect estimation performance in a small-world network with feedback loops, unmeasured confounding, and horizontal pleiotropy, with network size $p=5$.

Setting	Method	MaxAbsDev	MeanAbsDev	MeanSqDev
n = 500	MR.RGM	0.232 (0.076)	0.065 (0.008)	0.008 (0.003)
	MR.RGM+	0.129 (0.044)	0.045 (0.005)	0.003 (0.001)
	MR.RGM.NoConf	0.231 (0.082)	0.070 (0.015)	0.009 (0.004)
	MR-SimpleMedian	0.247 (0.051)	0.089 (0.016)	0.013 (0.004)
	MR-WeightedMedian	0.228 (0.057)	0.087 (0.017)	0.012 (0.005)
	MR-IVW	0.310 (0.065)	0.101 (0.017)	0.017 (0.005)
	OneSampleMR	0.298 (0.053)	0.100 (0.016)	0.016 (0.005)
	mrbytes	0.316 (0.062)	0.102 (0.017)	0.017 (0.005)
n = 1000	MR.RGM	0.276 (0.057)	0.063 (0.011)	0.009 (0.003)
	MR.RGM+	0.179 (0.207)	0.043 (0.021)	0.007 (0.016)
	MR.RGM.NoConf	0.214 (0.051)	0.068 (0.014)	0.009 (0.004)
	MR-SimpleMedian	0.183 (0.067)	0.062 (0.014)	0.007 (0.003)
	MR-WeightedMedian	0.188 (0.069)	0.061 (0.013)	0.006 (0.003)
	MR-IVW	0.292 (0.069)	0.081 (0.014)	0.013 (0.005)
	OneSampleMR	0.279 (0.058)	0.079 (0.014)	0.012 (0.004)
	mrbytes	0.292 (0.063)	0.081 (0.014)	0.013 (0.005)
n = 10000	MR.RGM	0.305 (0.039)	0.051 (0.004)	0.010 (0.001)
	MR.RGM+	0.306 (0.665)	0.038 (0.065)	0.040 (0.111)
	MR.RGM.NoConf	0.209 (0.027)	0.064 (0.007)	0.008 (0.001)
	MR-SimpleMedian	0.065 (0.015)	0.023 (0.003)	0.001 (0.0003)
	MR-WeightedMedian	0.065 (0.013)	0.023 (0.003)	0.001 (0.0002)
	MR-IVW	0.268 (0.019)	0.052 (0.005)	0.009 (0.001)
	OneSampleMR	0.256 (0.018)	0.050 (0.005)	0.008 (0.001)
	mrbytes	0.269 (0.019)	0.052 (0.005)	0.009 (0.001)
n = 30000	MR.RGM	0.300 (0.023)	0.047 (0.002)	0.010 (0.001)
	MR.RGM+	0.164 (0.253)	0.018 (0.022)	0.006 (0.014)
	MR.RGM.NoConf	0.206 (0.028)	0.064 (0.006)	0.008 (0.001)
	MR-SimpleMedian	0.044 (0.009)	0.015 (0.003)	0.0004 (0.0001)
	MR-WeightedMedian	0.044 (0.009)	0.015 (0.003)	0.0004 (0.0001)
	MR-IVW	0.264 (0.018)	0.047 (0.003)	0.008 (0.0008)
	OneSampleMR	0.251 (0.017)	0.045 (0.003)	0.008 (0.001)
	mrbytes	0.263 (0.018)	0.047 (0.003)	0.008 (0.001)

Table 12: Causal effect estimation performance in a small-world network with feedback loops, unmeasured confounding, and horizontal pleiotropy, with network size $p=10$.

Setting	Method	MaxAbsDev	MeanAbsDev	MeanSqDev
n = 500	MR.RGM	0.317 (0.063)	0.045 (0.005)	0.005 (0.001)
	MR.RGM+	0.201 (0.197)	0.037 (0.005)	0.003 (0.004)
	MR.RGM.NoConf	0.273 (0.062)	0.049 (0.005)	0.005 (0.001)
	MR-SimpleMedian	0.293 (0.037)	0.088 (0.006)	0.012 (0.002)
	MR-WeightedMedian	0.293 (0.034)	0.088 (0.006)	0.012 (0.002)
	MR-IVW	0.388 (0.057)	0.087 (0.007)	0.013 (0.002)
	OneSampleMR	0.367 (0.044)	0.087 (0.006)	0.013 (0.002)
	mrbytes	0.383 (0.051)	0.088 (0.007)	0.013 (0.002)
n = 1000	MR.RGM	0.315 (0.047)	0.042 (0.003)	0.005 (0.001)
	MR.RGM+	0.285 (0.367)	0.035 (0.013)	0.007 (0.013)
	MR.RGM.NoConf	0.219 (0.030)	0.045 (0.003)	0.004 (0.001)
	MR-SimpleMedian	0.222 (0.034)	0.064 (0.006)	0.007 (0.001)
	MR-WeightedMedian	0.209 (0.032)	0.063 (0.006)	0.006 (0.001)
	MR-IVW	0.332 (0.040)	0.066 (0.005)	0.008 (0.001)
	OneSampleMR	0.316 (0.042)	0.066 (0.005)	0.008 (0.001)
	mrbytes	0.334 (0.041)	0.067 (0.005)	0.008 (0.001)
n = 10000	MR.RGM	0.321 (0.019)	0.028 (0.002)	0.005 (0.0004)
	MR.RGM+	0.531 (0.806)	0.023 (0.021)	0.017 (0.033)
	MR.RGM.NoConf	0.218 (0.018)	0.042 (0.003)	0.004 (0.0004)
	MR-SimpleMedian	0.074 (0.015)	0.021 (0.002)	0.001 (0.0001)
	MR-WeightedMedian	0.074 (0.014)	0.021 (0.002)	0.001 (0.0001)
	MR-IVW	0.296 (0.014)	0.032 (0.002)	0.004 (0.0003)
	OneSampleMR	0.282 (0.015)	0.031 (0.002)	0.004 (0.0003)
	mrbytes	0.296 (0.015)	0.032 (0.002)	0.004 (0.0003)
n = 30000	MR.RGM	0.324 (0.015)	0.024 (0.002)	0.005 (0.0005)
	MR.RGM+	0.351 (0.812)	0.013 (0.020)	0.012 (0.033)
	MR.RGM.NoConf	0.214 (0.018)	0.042 (0.003)	0.004 (0.0002)
	MR-SimpleMedian	0.044 (0.006)	0.013 (0.002)	0.0003 (0.0001)
	MR-WeightedMedian	0.044 (0.006)	0.013 (0.002)	0.0003 (0.0001)
	MR-IVW	0.283 (0.014)	0.026 (0.001)	0.004 (0.0002)
	OneSampleMR	0.268 (0.013)	0.025 (0.001)	0.004 (0.0002)
	mrbytes	0.282 (0.014)	0.026 (0.001)	0.004 (0.0002)

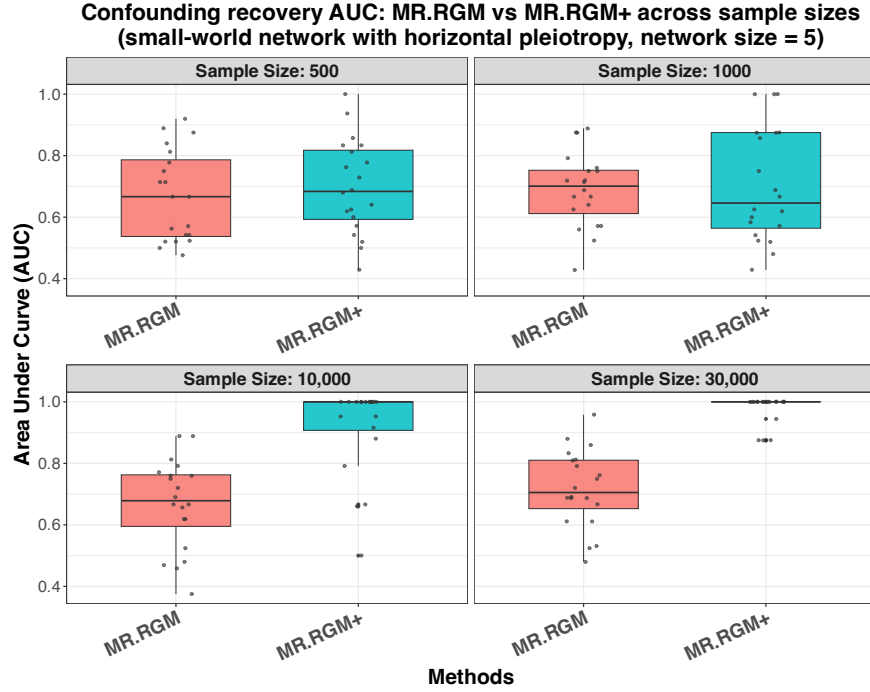


Figure 9: Confounding structure recovery performance using MR.RGM and MR.RGM+ in a small-world network with feedback loops, unmeasured confounding, and horizontal pleiotropy, with network size $p=5$. Boxplots of AUC by method (x-axis) and sample size (facets; $n \in \{500, 1000, 10000, 30000\}$).

Table 13: Confounding structure recovery performance using MR.RGM in a small-world network with feedback loops, unmeasured confounding, and horizontal pleiotropy, across network sizes $p \in \{5, 10\}$.

Setting	Sample Size	AUC	TPR	FDR	MCC
$p = 5$	500	0.669 (0.143)	0.415 (0.307)	0.537 (0.296)	0.082 (0.336)
	1000	0.689 (0.119)	0.505 (0.292)	0.526 (0.253)	0.105 (0.357)
	10000	0.668 (0.142)	0.888 (0.166)	0.470 (0.278)	0.351 (0.278)
	30000	0.718 (0.123)	0.919 (0.143)	0.473 (0.283)	0.371 (0.297)
$p = 10$	500	0.618 (0.095)	0.306 (0.121)	0.365 (0.213)	0.136 (0.129)
	1000	0.677 (0.053)	0.432 (0.074)	0.320 (0.187)	0.222 (0.086)
	10000	0.841 (0.055)	0.890 (0.086)	0.255 (0.225)	0.564 (0.173)
	30000	0.860 (0.065)	0.952 (0.055)	0.289 (0.233)	0.577 (0.194)

Table 14: Confounding structure recovery performance using MR.RGM+ in a small-world network with feedback loops, unmeasured confounding, and horizontal pleiotropy, across network sizes $p \in \{5, 10\}$.

Setting	Sample Size	AUC	TPR	FDR	MCC
$p = 5$	500	0.698 (0.149)	0.327 (0.288)	0.403 (0.402)	0.203 (0.347)
	1000	0.704 (0.181)	0.506 (0.290)	0.360 (0.305)	0.292 (0.283)
	10000	0.916 (0.142)	0.881 (0.178)	0.321 (0.327)	0.574 (0.270)
	30000	0.978 (0.045)	1.000 (0.000)	0.311 (0.358)	0.694 (0.351)
$p = 10$	500	0.685 (0.096)	0.233 (0.116)	0.236 (0.208)	0.205 (0.138)
	1000	0.733 (0.066)	0.352 (0.102)	0.183 (0.177)	0.315 (0.107)
	10000	0.938 (0.085)	0.866 (0.086)	0.174 (0.259)	0.660 (0.243)
	30000	0.950 (0.097)	0.994 (0.020)	0.162 (0.290)	0.824 (0.297)

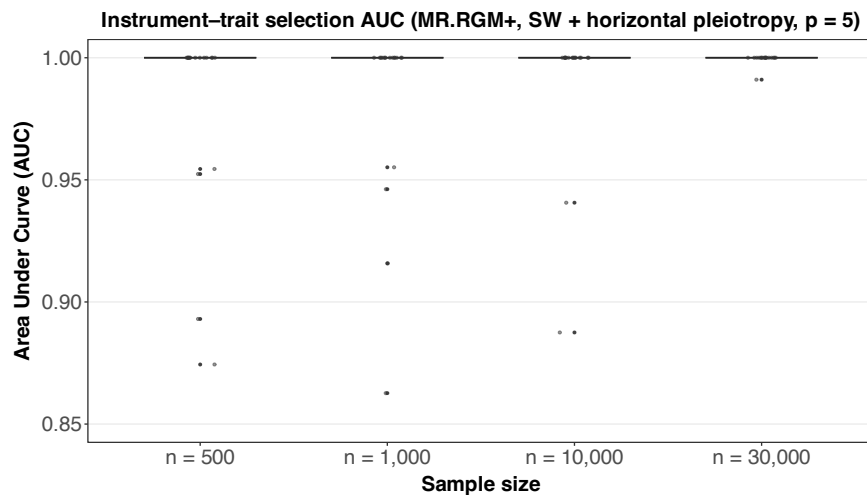


Figure 10: Instrument-trait selection performance using MR.RGM+ in a small-world network with feedback loops, unmeasured confounding, and horizontal pleiotropy, with network size $p=5$. Box-plots of AUC across sample sizes ($n \in \{500, 1000, 10000, 30000\}$).

References

- [1] Jack Bowden, George Davey Smith, and Stephen Burgess. Mendelian randomization with invalid instruments: effect estimation and bias detection through Egger regression. *International Journal of Epidemiology*, 44(2):512–525, 2015.
- [2] Enes Makalic and Daniel F. Schmidt. A Simple Sampler for the Horseshoe Estimator. *IEEE Signal Processing Letters*, 23(1):179–182, 2016.
- [3] Hao Wang. Scaling It Up: Stochastic Search Structure Learning in Graphical Models. *Bayesian Analysis*, 10(2):351–377, June 2015.
- [4] Zhongshang Yuan, Huanhuan Zhu, Ping Zeng, Sheng Yang, Shiquan Sun, Can Yang, Jin Liu, and Xiang Zhou. Testing and controlling for horizontal pleiotropy with probabilistic Mendelian randomization in transcriptome-wide association studies. *Nature Communications*, 11(1):3861, 2020.